PROTECTION OF BIOMEDICAL ALLOYS BY THIN FILMS OF ALUMINA AND HAFNIA PREPARED BY ATOMIC LAYER DEPOSITION

Ivan Spajić

Doctoral Dissertation
Jožef Stefan International Postgraduate School
Ljubljana, Slovenia

Supervisor: Prof. Dr. Ingrid Milošev, Jožef Stefan Institute, Ljubljana, Slovenia

Evaluation Board:
Prof. Dr. Dragan Mihailović, Chair, IPS and Jožef Stefan Institute, Ljubljana, Slovenia
Asst. Prof. Matjaž Spreitzer, Member, IPS and Jožef Stefan Institute, Ljubljana, Slovenia
Prof. Dr. Mustafa Ürgen, Member, Technical University Istanbul, Istanbul, Turkey

MEDNARODNA PODIPLOMSKA ŠOLA JOŽEFA STEFANA
JOŽEF STEFAN INTERNATIONAL POSTGRADUATE SCHOOL

Ivan Spajić

PROTECTION OF BIOMEDICAL ALLOYS BY THIN FILMS OF ALUMINA AND HAFNIA PREPARED BY ATOMIC LAYER DEPOSITION

Doctoral Dissertation

ZAŠČITA BIOMEDICINSKIH ZLITIN Z NANOSOM TANKIH ATOMSKIH PLASTI ALUMINIJEVEGA IN HAFNIJEVEGA OKSIDA

Doktorska disertacija

Supervisor: Prof. Dr. Ingrid Milošev

Ljubljana, Slovenia, May 2022

Acknowledgments

First of all, I thank my mentor, prof. Ingrid Milošev, for valuable discussions and help in planning and writing my doctoral thesis. Also, thank you for giving me the great opportunity to get a scientific career at the Jožef Stefan Institute.

Also, I am grateful to all in the K3 department, Department of Physical and Organic Chemistry. Special thanks to dr. Peter Rodič for introducing me to the work on the atomic layer deposition technique and Barbara Kapun for SEM-EDXS and FIB analyses. To all other colleagues, thank you for all your help during my experimental work, especially for stimulating discussions - this often gave me great motivation.

I am also grateful to the Center for Excellence in Nanoscience and Nanotechnology (CENN Nanocenter) at the Jožef Stefan Institute for its generosity and accessibility in using the necessary scientific equipment.

Many thanks to dr. Maria Lekka, who was the leader of the mCBEEs project under the Marie Skłodowska Curie grant agreement no. 764977 of the European Union's Horizon H2020 research and innovation program, from which my PhD project was funded. Special thanks for all the help during my stay in Udine and valuable discussions about my work. Also, thanks to all colleagues and mentors involved in the mCBEEs project for valuable discussions and teaching.

Also, Slovenian Research Agency is acknowledged for funding (grant no. P2-0393).

Last but not least, I thank my family and friends for their tremendous support throughout the whole study.

Abstract

One of the most commonly used metal materials for the manufacture of biomedical implants are stainless steel and titanium-based alloys. Due to the specific conditions and complex environment in the human body, different strategies have been employed to protect them and improve their functionality in vivo. In this thesis, a novel method of atomic layer deposition (ALD) was used for the deposition of ultrathin protective barrier oxide films on commercially pure titanium (cp-Ti) and stainless steel 316L (SS316L). The aim was to study the composition, thickness, structure, morphology, corrosion properties, biocompatibility and antibacterials properties of ALD oxide films.

Alumina (Al2O3) and hafnia (HfO2) ALD thin films of different thicknesses were applied on differently prepared surfaces of cp-Ti and SS316L. In addition to single layers, the combination of alumina and hafnia in a multilayer configuration was studied. Electrochemical techniques, potentiodynamic polarization and electrochemical impedance spectroscopy were used as the main methods of testing the corrosion properties of bare and ALD-coated substrates. All measurements were carried out in simulated physiological solution at 37 °C. The composition, structure and morphology of deposited films were studied using SEM/EDS, ToF-SIMS, XPS, AFM-SKPFM, TEM, XRD and ellipsometry.

The method of metal surface preparation significantly affects the protective properties of ALD alumina and hafnia thin films, even when deposited as relatively thick layers of ca. 150 nm. There is a critical deposition thickness that provides barrier corrosion protection of ALD films on cp-Ti and SS316L. Very thin ALD alumina film of 20 nm proved to be unprotective, while 60 nm thin film showed good protection during 30 days of immersion in simulated physiological solution. Multilayer ALD thin film, consisting of hafnia interlayer between alumina layers, showed no significant improvement compared to single-layer alumina thin film of the same thickness.

Both ALD thin films, alumina and hafnia, did not show significantly altered biocompatible nor antibacterial properties compared to bare cp-Ti and SS316L substrates. However, the surface roughness of ALD thin films, primarily the presence of agglomerates, can significantly affect the attachment and development of cells on the surface. On the other hand, the development of bacteria on the surface of ALD thin films is not related to the presence of agglomerate but rather to surface chemical properties.

We concluded that ALD thin films of alumina and hafnia, prepared under optimized conditions of substrate preparation and process parameters, assure excellent corrosion protection of cp-titanium and stainless steel in simulated biomedical applications and are biocompatible.

Povzetek

Eden od najpogostejše uporabljenih kovinskih materialov za izdelavo biomedicinskih vsadkov so nerjavno jeklo in zlitine na osnovi titana. Zaradi specifičnih pogojev in kompleksnega okolja v človeškem telesu so bile uporabljene različne strategije za njihovo zaščito in izboljšanje njihove funkcionalnosti in vivo. V doktorskem delu je bila uporabljena nova metoda za nanašanje ultratankih zaščitnih oksidnih filmov na komercialno čisti titan (cp-Ti) in nerjavno jeklo 316L (SS316L), atomsko nanašanje plasti (ALD). Cilj je bil preučiti sestavo, debelino, strukturo, morfologijo, korozijske lastnosti, biokompatibilnost in antibakterijske lastnosti ALD oksidnih filmov.

Tanke plasti iz aluminijevega (Al_2O_3) in hafnijevega oksida (HfO_2) različnih debelin so bile nanešene na različno pripravljene površine cp-Ti in SS316L. Poleg enoslojnih je bila tudi raziskana kombinacija alumine in hafnije v večplastni konfiguraciji. Kot glavne metode raziskovanja korozijskih lastnosti nezaščitenih in ALD prevlečenih podlag so bile uporabljene elektrokemijske tehnike, potenciodinamska polarizacija in elektrokemijska impedančna spektroskopija. Vse meritve so bile izvedene v simulirani fiziološki raztopini pri 37 °C. Sestavo, strukturo in morfologijo deponiranih filmov smo proučevali s pomočjo SEM/EDS, ToF-SIMS, XPS, AFM-SKPFM, TEM, XRD in elipsometrije.

Način priprave kovinske površine pomembno vpliva na zaščitne lastnosti ALD tankih filmov iz Al_2O_3 in HfO_2, tudi če gre za relativno debele plasti ca. 150 nm. Obstaja kritična debelina nanosa, ki zagotavlja stabilno korozijsko zaščito ALD filmov na cp-Ti in SS316L. Zelo tanek ALD film alumine, debeline 20 nm, se je izkazal kot nestabilen, medtem je film debeline 60 nm pokazal dobro zaščito v 30 dneh potopitve v simulirani fiziološki raztopini. Večplastni ALD film, ki vsebuje vmesni sloj HfO_2 med plastmi Al_2O_3, ni pokazal bistvenega izboljšanja v primerjavi z enoslojnim tankim filmom iz Al_2O_3 enake debeline.

Analize so pokazale, da Al_2O_3 and HfO_2 ne izkazujeta bistveno spremenjenih biokompatibilnih ali antibakterijskih lastnosti v primerjavi z nezaščitenima cp-Ti in SS316L podlagama. Vendar pa lahko površinska hrapavost filmov, predvsem prisotnost aglomeratov, pomembno vpliva na pritrditev in razvoj celic na površini. Po drugi strani, pa razvoj bakterij na površini tankih ALD filmov ni povezan s prisotnostjo aglomeratov, temveč s kemijskimi lastnostmi površine.

Ugotovili smo, da ALD tanki filmi iz Al_2O_3 and HfO_2, pripravljeni pri optimiziranih pogojih priprave podlage in procesnih parametrov, zagotavljajo odlično korozijsko zaščito cp-titana in nerjavnega jekla v simuliranih biomedicinskih aplikacijah in so biokompatibilni.

Contents

List of Figures

List of Tables

Chapter 1

Introduction

1.1 Aim of the work

This doctoral dissertation deals with the application of the atomic layer deposition (ALD) method with the purpose of protecting metallic biomaterials, commercially pure titanium (cp-Ti) and stainless steel (SS316L) in the simulated biological environment. Two types of ALD thin films were used, aluminum(III) oxide (Al_2O_3) and hafnium(IV) oxide (HfO_2), also called alumina and hafnia. Physicochemical and protective barrier properties of alumina and hafnia ALD thin films deposited on cp-Ti and SS316L have been investigated in simulated body fluid (SBF) as the electrolyte. Their material properties were studied using various surface analysis methods. One part of the study is related to the ALD thin films in contact with living cells and bacteria to study their biocompatible and antibacterial properties, respectively.

This thesis is divided into four separate studies or topics: the first focusing on the effect of substrate surface preparation on the protective properties of deposited ALD films; the second and third are focused on the effect of thickness and multilayer structure on the protective properties of ALD films; and the fourth is focused exclusively on biologically-related properties of ALD thin films, i.e. biocompatibility and antibacterial properties.
The ultimate goal of this study is to consider the possible application of alumina and hafnia ALD films on implant devices made of cp-Ti and SS316L to be used in the human body.

1.2 Biomaterials

The implantation of artificial materials into the human body dates back to the ancient past. There are findings that ancient civilizations used prostheses to repair fractured and diseased tissues and organs, even a few 1000 years B.C. [1]. For example, it is known that the Greeks and Egyptians implanted wood and animal bones in humans. Since then, and especially in the last century, biomaterials have progressed astonishingly. As medical technology has evolved, efforts have been made to systematize and standardize the materials and methods used in the field. The European Society for Biomaterials, founded in 1976, organized the Consensus Conference on Definitions in Biomaterials Science, in 1987 [2], which then read: “Biomaterials are nonviable materials intended to interface with biological systems to evaluate, treat, augment or replace any tissue, organ or function of the body” [2], [3]. Nowadays, we use different implantable materials and devices for versatile purposes. Accordingly, in the last few years the definition of biomaterials has been modified and expanded [4], [5]. Namely, in medical technology today, implantation includes devices and processes such as drug and gene delivery systems, nanotechnology-based

imaging and diagnostic systems, microelectronic devices, tissue engineering and cell therapies, organ printing and cell patterning. Therefore, as stated in this leading opinion paper [4]: "These technologies encompass the use of not only metals, ceramics and synthetic polymers, but also natural polymers, nanoparticles, carbon nanotubes, quantum dots, etc. Some new materials or substances which hitherto we may not have thought of as biomaterials should now be considered as such".

Generally, when it comes to metallic biomaterials used today for implantation purposes, they are mainly alloys composed of Ti, Fe and Co as the main elements, while Cr, Mo, Ni, V, Al and Ta are used as minor elements. Each material has specific chemical and mechanical properties and exhibits particular behavior in contact with living tissue based on which it is selected for a particular application. The three most common groups of materials used are stainless steel, Co-Cr-based alloys, and Ti based alloys [6]. In addition to these three large groups of metallic biomaterials, there is also a group of so-called "miscellaneous implant materials" used much less frequently, such as NiTi alloys, Mg, Ta and Au [7].

1.2.1 Stainless steel

The first steel developed in the early 1900s specifically for implantation in medicine was vanadium steel and aluminum [3]. However, many shortcomings in the implantation of this steel soon became apparent, as evidenced by mechanical failure, corrosion, and poor biocompatibility. These issues have spurred research and development of new steel alloys that would be more suitable for implantation. For example, by adding Mo, it was found that it is possible to improve the corrosion resistance in an acidic medium [8], and later in the 1950s, by reducing the C content to the max. 0.03% contributed to minimizing the occurrence of intergranular corrosion [9]. This alloy has been denoted 316L by the American Iron and Steel Institute (AISI) and is often named surgical or orthopedic stainless steel.

Stainless steel 316L (SS316L) has an austenitic (γ) structure with a face-centered cubic (FCC) cell, which is responsible for good strength and ductility, as well as easy for machining [10]. In addition to Fe, the main alloying elements are present in varying percentages as stated: Cr (17-19 wt%), Ni (13-15 wt%), Mo (2-3 wt%), Mn (0-2 wt%), and with small quantities (<1 wt%) of Si, Cu, P, C, S and N [6], [11]. The most critical element for the corrosion resistance of the SS316L is Cr because it enables the formation of chromium(III) oxide (Cr_2O_3) passive layer, which in combination mainly with iron(II) and iron(III) oxides (FeO and Fe_2O_3) provides a high level of protection under different conditions [12], [13]. Ni is credited for stabilizing the austenitic phase down to room temperature; otherwise, the structure of the Fe austenitic phase is stable only above 910 °C [14]. Therefore, Ni is directly responsible for the structure that gives steel excellent ductility and toughness at high strength [10]. Mo, as already mentioned, improves the corrosion resistance of steel in an acidic medium, especially when it comes to pitting corrosion [15]. Further, Mn in smaller quantities favors the austenitic structure and in the molten state of steel, increases the solubility of N and prevents its oxidation [16]. Of the elements present in a smaller percentage, C is significant as it modifies the mechanical properties of steel by increasing its tensile strength and hardness but lowering ductility [17]. Also, as already mentioned, C can weaken the corrosion resistance of steel because it enhances susceptibility to intergranular corrosion [9]. Besides C, also N, which is present in small quantities, considerably modifies steel's mechanical properties, as it stabilizes the austenitic phase [18].

1.2.2 Titanium

Unlike steel, industrial production of Ti began relatively late, in 1946. At the outset, Ti was reserved mainly for use in the aerospace industry due to its low density and high corrosion resistance. The advantages of using Ti in medicine were soon discovered, leading to the need to study and develop new Ti alloys that are more suitable for specific purposes in medicine.

Unalloyed Ti, also known as commercially pure Ti (cp-Ti), is characterized by excellent corrosion resistance due to its passive film. There are four grades (ASTM F 67) of cp-Ti according to the content of its trace elements. They vary in tensile strength as a function of those elements, primarily O [19]. Cp-Ti grade 2 is the "workhorse" of the commercially pure Ti industry. It is characterized by good enough formability and ductility, and its strength is comparable to annealed austenitic stainless steel [20]. Its composition is expressed in the maximum quantity of trace elements as follows: C (max 0.10 wt%), Fe (max 0.20 wt%), H (max 0.015 wt%), N (max 0.03 wt%), O (max 0.25 wt%), and Ti in balance [19]. Pure Ti is an allotropic element, i.e. depending on the physical conditions, it can exist in more than one crystallographic form. At room temperature, Ti exists in the hexagonal close-packed (HCP) crystal structure or alpha (α) phase, while at temperatures above 883 C, it is transformed into the body-centered cubic (BCC) crystal structure or beta (β) phase [19]. However, by alloying Ti with other elements, each crystalline phase can be selectively stabilized at room temperature [20]. Accordingly, Ti alloys are categorized depending on the share of these two phases in the structure; hence, there are alpha, alpha-beta and beta Ti alloys. Generally, alpha Ti alloys are characterized by increased strength and lower ductility than cp-Ti and have good weldability. Beta Ti alloys are extremely easy for forming as their main characteristic is ductility, but they are not weldable. Alpha-beta Ti alloys have a good combination of strength and ductility [20], [21]. The most commonly used Ti alloy, in general, is the alpha-beta alloy Ti 6Al-4V, which is also known as Ti grade 5 and, together with cp-Ti, it is widely used for biomedical purposes [22].

1.2.3 Cobalt-Chromium

As the third major group of alloys used for biomedical purposes, Co-Cr alloys began to develop extensively in the 1930s with the development of the Co-30Cr-7W-0.5C alloy, named Vitallium [3]. At first, it was used in dentistry as an alternative to the expensive gold alloys, but later it began to be used for artificial joints where its strength is expressed. Over time, many different Co-Cr alloys, which usually contain Mo, have been developed, commonly referred to as Co-Cr-Mo alloys [3]. These alloys are known for their strength, so they are often used for load-bearing purposes and are common in hip and knee arthroplasty. They are highly resistant to corrosion, comparable to SS316L [3], and show relatively good wear resistance in usage [23], [24]. As Co-Cr-Mo alloys are not the subject of the research in this thesis, a more detailed description is beyond the scope of the present thesis.

1.2.4 Basic features of SS316L and cp-Ti and their applications

Although almost all metallic biomaterials have good mechanical properties in terms of strength and toughness, they often show biomechanical incompatibility when loaded and attached to adjacent bone. This issue relates to their high modulus of elasticity (in units of GPa) or Young's modulus, which is a quantity that measures the resistance of the material to being deformed elastically when stress or load is applied to it. The inhomogeneous transfer of stress between the implant and bone may result in bone

resorption, death of bone cells, and, eventually, even implant rejection. This biomechanical incompatibility is named the "stress shielding effect" [25]. The elastic modulus of a bone varies between 4 and 30 GPa, depending on the type of bone and the direction of the measurement, i.e. vertically or along the long axis of the bone [25], [26]. Co-Cr alloys are characterized by the highest values of Young's modulus (> 200 GPa), then SS316L (190 GPa), and the lowest value has cp-Ti (110 GPa) [6]; thus, the concern over stress shielding is reduced for cp-Ti.

Due to the different properties of SS316L and cp Ti, they are commonly applied for different purposes. SS316L is characterized by good mechanical properties and has better strength and wear resistance than cp-Ti [27]. Due to its high Young's modulus, it is mainly used for temporary implant components (like screws, plates, nails, etc.) and for permanent implants in less active patients [3]. Despite its relatively good corrosion resistance, local corrosion can cause serious consequences due to the release of toxic metal ions, which may act as allergens and carcinogens [28]–[30].

On the other hand, cp-Ti is characterized by better corrosion resistance [31] thanks to its high affinity for oxygen and the spontaneous formation of highly stable amorphous passive film on the surface [32]. Further, its strength to weight ratio is around 50% greater than SS316 [28], making it a better-suited material for specific applications with high loading rates. However, cp-Ti is susceptible to cyclic loading and has poor wear resistance, i.e. fretting corrosion resistance, so it is avoided for applications where these may occur [22], [25]. Therefore, cp-Ti is most commonly used for housing devices for pacemakers, artificial heart valves, dental implants and maxillofacial surgery [3].

1.3 Corrosion

In the broadest sense, corrosion of metals is defined as the destructive attack of a metal by its reaction with the environment [33]. However, in practice, it is mainly an electrochemical process in the aqueous environment in the presence of oxygen and chloride ions. Therefore, when considering the implantation of any metallic material in the human body, which is a complex electrolytic environment, the degradation of implanted material must be of great concern. Therefore, understanding the fundamental electrochemistry behind the corrosion is essential. Hence, when a self-passivating metal is immersed in an aqueous electrolyte, an electrically conductive solution, a metal oxide film is formed on the surface. This oxide film can effectively prevent the corrosion of the metal resulting in the passivation of the metal surface. If the solution is acidic, the oxide film may be dissolved completely,

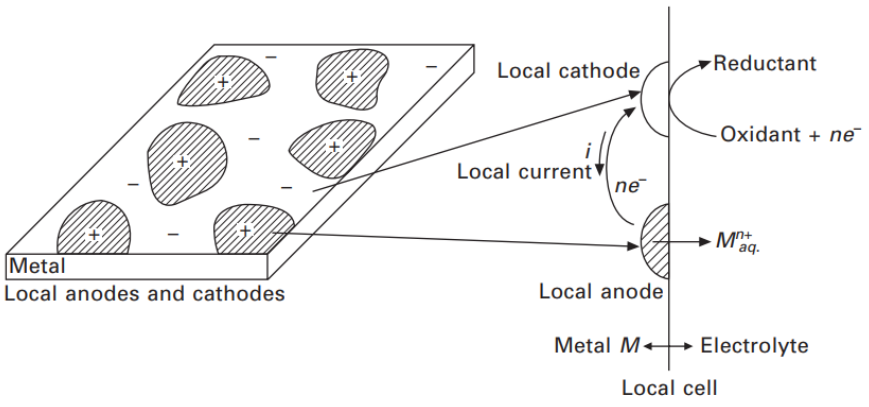

Figure 1.1: Schematic illustration of the local galvanic cells on the metal surface [34].

leaving a bare metal surface, which is then in its active state. If that is the case, an infinite number of anodic and cathodic sites are formed on the metal surface at the atomic level. Consequently, the short-circuit current flows between the local anodes and cathodes. Such a system is called a galvanic cell (**Fig. 1.1**) [34].

Anodic sites are places where oxidation takes place (**Eq. 1.1**), i.e. the release of electrons from metal atoms and its dissolution in the electrolyte, and cathodic sites are places where the opposite process, i.e. reduction, takes place (**Eqs. 1.2-1.5**), with the reception of electrons by species from electrolyte (dissolved oxygen, hydrogen and water). In most cases, the reduction process involves hydrogen evolution reaction (HER) and oxygen reduction reaction (ORR). If the electrolyte is acidic, HER proceeds according to **Eq. 1.2,** and ORR according to **Eq. 1.3**. However, if it is about alkaline or neutral electrolyte, HER corresponds to **Eq. 1.4**, and ORR to **Eq. 1.5** [33], [34]**.**

$$\mathrm{M} \rightarrow \mathrm{M^{n+}} + \mathrm{ne^-} \tag{1.1}$$

$$2\mathrm{H^+} + 2\mathrm{e^-} \rightarrow \mathrm{H_2} \tag{1.2}$$

$$\mathrm{O_2} + 4\mathrm{H^+} + 4\mathrm{e^-} \rightarrow 2\mathrm{H_2O} \tag{1.3}$$

$$2\mathrm{H_2O} + 2\mathrm{e^-} \rightarrow \mathrm{H_2} + 2\mathrm{OH^-} \tag{1.4}$$

$$\mathrm{O_2} + 2\mathrm{H_2O} + 4\mathrm{e^-} \rightarrow 4\mathrm{OH^-} \tag{1.5}$$

Each of these reactions is called the half-cell reaction, but in practice, the anodic and cathodic reactions occur in a coupled manner making the galvanic cell, as shown in **Fig. 1.1**. Therefore, the whole corrosion process is controlled by both anodic and cathodic reactions, as they are interdependent. For a deeper understanding of the metal corrosion in an electrolyte, i.e. metal dissolution, we must focus on the anodic reaction (**Eq. 1.1**). When the metal atoms release electrons, positively charged metal ions pass from the bulk metal into the electrolyte, leaving electrons behind in the metal. The accumulation of negative charge on the metal due to the residual electrons increases the potential difference between the metal and the electrolyte. This potential difference is named the *electrode potential* (or *electrochemical potential*) of the metal, thus becoming more negative. The change in the potential over time tends to retard the dissolution of metal and encourage the deposition of dissolved metal ions from the electrolyte onto the metal, i.e. the reverse reaction is established (**Eq. 1.6**). Continuation of the dissolution and deposition of metal ions would result in the metal reaching a stable potential so that the rate of dissolution becomes equal to the rate of deposition. This potential is named the *reversible electrode potential* (E_{rev}), and is defined by the Nernst equation (**Eq. 1.7)** [33]. However, in reality the corrosion reactions are irreversible and it is not possible to obtain E_{rev} as described, but another value, *corrosion potential* (E_{corr}) is determined by mixed potential kinetics [33].

$$\mathrm{M} \leftrightarrows \mathrm{M^{n+}} + \mathrm{ne^-} \tag{1.6}$$

$$E_{\mathrm{rev}} = E^0 + \frac{RT}{nF} \ln \frac{[\mathrm{M}^{n+}]}{[\mathrm{M}]} \tag{1.7}$$

where R is the gas constant, T is the absolute temperature, F is the Faraday constant, n is the number of electrons transferred per ion, $[M^{n+}]$ and $[M]$ are activities of metal ion and metal, and E^0 is standard electrode potential, respectively.

The *standard electrode potential* is also known as the *electromotive force* (EMF) of a particular metal, and it is equal to the potential of the corresponding half-cell reaction at standard conditions ($[M^{n+}] = 1$ M; p = 1 atm; T = 25 °C). In other words, it indicates the tendency of metal toward a particular electrochemical half-cell reaction. The list of all metals and corresponding half-cell reactions is named EMF series and is expressed as reduction potentials, from positive values (noble metals) to negative values (active metals). The EMF series is relative to the standard hydrogen electrode (SHE) with the potential of 0 V. The EMF series of the metals relevant to biomedical applications is summarized in **Table 1.1** [33], [34]. It is noteworthy that the order of the EMF values of metals does not directly correspond to their corrosion rate because the solubility of their passive films, i.e. metal oxides or hydroxides, is different, and in some cases, it may provide strong protection on the metal surface. For this reason, there is also the list of practical nobility of metals which provides a somewhat more realistic insight into the corrosion resistance of metals. Ti and Cr are at the bottom of this list, indicating that they are very susceptible to corrosion; however, due to their very protective passive films, in practice, they are very resistant to corrosion [3].

Table 1.1: The standard EMF series of metals relevant to biomedical applications with respect to SHE as the reference of 0 V.

Half-cell reaction	$\boldsymbol{E^0}$ **(V vs. SHE)**
$Au^{3+} + 3e^- \leftrightarrows Au$	+1.498
$Pd^{2+} + 2e^- \leftrightarrows Pd$	+0.987
$Ag^{+} + e^- \leftrightarrows Ag$	+0.799
$2H^{+} + 2e^- \leftrightarrows H_2$	0.000
$Co^{2+} + 2e^- \leftrightarrows Co$	−0.277
$Fe^{2+} + 2e^- \leftrightarrows Fe$	−0.440
$Cr^{3+} + 3e^- \leftrightarrows Cr$	−0.744
$Ti^{2+} + 2e^- \leftrightarrows Ti$	−1.630

The list of practical nobility, which is not shown here, is formed based on Pourbaix (E vs. pH) diagrams for different metals. The *Pourbaix diagram* represents the stability of all possible phases or compounds when considering certain metals in an aqueous electrolyte. It is constructed based on Nernst equations for all possible reactions under certain conditions. The results are displayed in the potential-pH plane [33]. The Pourbaix diagrams for Fe, as the main component in SS316L, and for Ti are shown in **Fig. 1.2.** The water is stable only between the dashed lines; below that region, the HER occurs, while above that region, an oxygen evolution reaction (OER) occurs [33].

According to the diagram in **Fig. 1.2 a**, Fe can undergo corrosion at potentials more positive than *ca.* −0.6 V and pH values below *ca.* 9, as a ferrous ion (Fe^{2+}) is the stable species. Under more acidic conditions, iron oxidation proceeds through the formation of ferric ion (Fe^{3+}) and propagates corrosion. In alkaline solutions, corrosion might occur

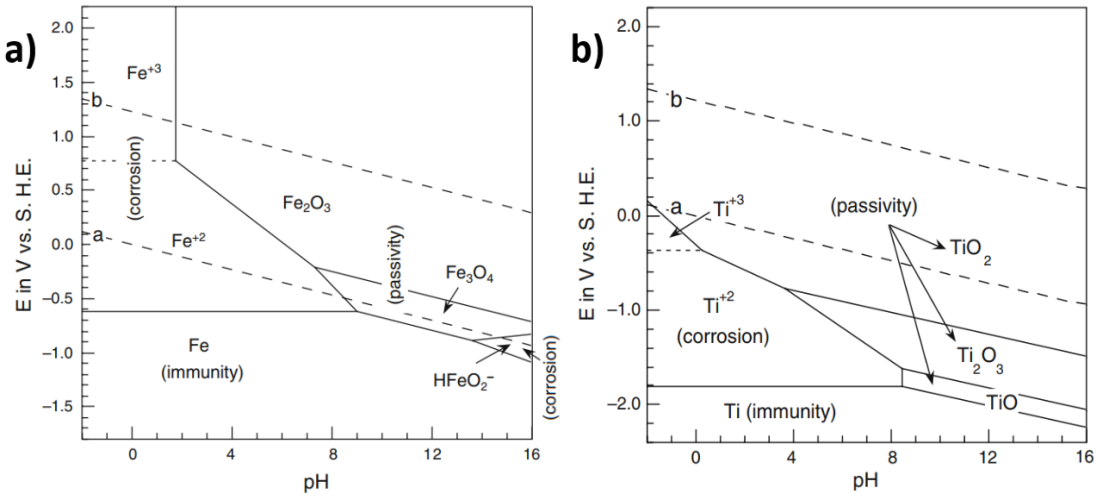

Figure 1.2: Pourbaix diagrams at 25 °C for **a)** iron-water system and **b)** titanium-water system [33].

under the conditions where the complex hypoferrite ion $[HFeO_2]^-$ is the stable species [3], [33]. These regions constitute *regions of corrosion*, where Fe can corrode from a thermodynamic point of view.

There is the *region of immunity* at lower potentials, where Fe is thermodynamically stable in its elementary state and does not corrode. In the pH range from *ca.* 9 to 13, Fe could pass directly to the *region of passivity*, as Fe_3O_4 and Fe_2O_3 may be formed as stable compounds [33].

In the case of Ti (**Fig. 1.2 b**), although it is a thermodynamically active metal (**Table 1.1**), it shows a large region of passivity based on the rapid formation of Ti suboxides (TiO and Ti_2O_3) and Ti dioxide (TiO_2). This tightly adherent passive film is at specific potentials stable at all pH values [3]. The corrosion region, where Ti ions (Ti^{2+} and Ti^{3+}) are stable species, occurs only at low pH in solutions without oxidizers. However, due to its high oxygen affinity, Ti is spontaneously passivated in almost all environments that contain oxygen, even in strongly oxidizing acids [3], [33].

It is crucial to emphasize that these diagrams are helpful only for informational purposes since they are based on thermodynamic data and do not reflect the kinetics of processes. Consequently, it is not possible to deduce which reaction will happen at a measurable rate. Further, whether metal oxide formed will be protective depends on its nature and the environment in contact with it. The effect of the environment is not included in the diagrams since it is calculated for an aqueous system [3], [33].

1.3.1 Types of corrosion processes

Depending on the type of metal and corrosive medium, there are different types of corrosion. Corrosion observed by the naked eye is called general or uniform corrosion. Another form of corrosion is localized corrosion which comprises pitting, crevice, intergranular and galvanic corrosion [34]. The former two types may cause significant problems for certain metals in biomedical applications. In addition, there are forms of corrosion that occur under mechanical load and are also typical for metallic biomaterials. These are stress corrosion cracking, fatigue and fretting corrosion [34]. All the forms of corrosion are shown in **Fig. 1.3** [34].

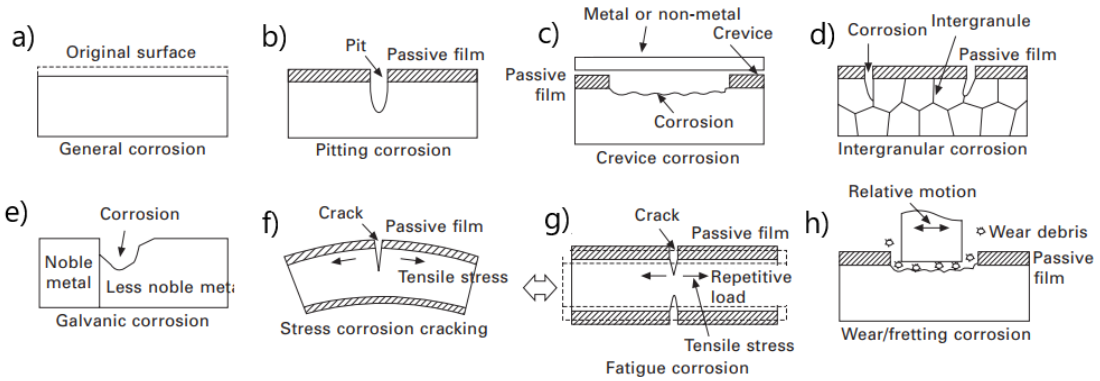

Figure 1.3: Schematic illustration of different types of corrosion [34].

General corrosion (**Fig. 1.3 a**), i.e. when the whole surface of the metal is uniformly corroded, is not an issue for modern biomedical alloys since they are protected by a passive film. However, pitting corrosion (**Fig. 1.3 b**), which refers to the formation of small cavities or pits at the metal surface when interacting with certain aggressive species, is a common corrosion problem under physiological conditions. The aggressive species are usually halogenous ions, such as chloride ions or reduced sulfur compounds [34], [35]. Crevice corrosion is another type of localized corrosion (**Fig. 1.3 c**). It occurs inside the crevice in the implant device where the mass diffusion is restricted so that there is usually a decrease in oxygen concentration and pH value and an increase in the concentration of aggressive chloride ions [34]. This process causes differential aeration. Further, adsorption of various organic or inorganic substances on the metal surface may lead to non-uniform coverage of the surface leading to critical sites exposed to aggressive bioenvironment [3]. Intergranular corrosion is a type of corrosion that is inherent to steel alloys (**Fig. 1.3 d**) and occurs selectively at grain

boundaries, which can progress very deep into the material [34]. Galvanic corrosion (**Fig. 1.3 e**) occurs when two metals of different electrode potentials are in direct contact with the electrolyte. In such a system, an anodic reaction, i.e. oxidation or corrosion, occurs on a less noble metal and a cathodic reduction reaction on a nobler metal [34]. Forms of corrosion that occur in combination with mechanical loads are associated with weakening of the passive film due to the applied specific loads, as illustrated (**Fig. 1.3 f-h**) [34].

1.3.2 Corrosion in the biological environment

The human body is a harsh environment for metals because its total mass consists of 40% to 60% of the water at a temperature around 37 °C with commonly good oxygenation, with dissolved 0.9 wt.% NaCl, and pH value around 7.4 [3]. In addition, it also contains many different inorganic salts such as bicarbonates, phosphates, sulphates with different cations such as potassium, calcium and magnesium cations, and a large variety of organic species. Although all of these species may contribute to corrosion of metallic implants to some extent, the most important species from the corrosion point of view are chloride ions due to their ability to disrupt passive films [3], [36]. On the other hand, calcium phosphate, which is spontaneously deposited, especially on Ti-based implants when implanted in the human body [25], [37], can insulate the metal surface from the environment and decelerate corrosion [34].

In addition to inorganic species, there are many different organic substances in body fluids, the concentration of which can exceed 80 g/L, that can play an important role in the corrosion of metallic biomaterials [6]. These include, for example, plasma that includes various proteins, e.g. albumin and fibrinogen, lymph and synovial or joint fluids with different proteins and lipids, etc. [38]. There are many reports on the effect of proteins on the corrosion behavior of different biomaterials [39]–[41]. Due to their chemical complexity, they may have both desirable and undesirable effects on the functionality of the implanted biomaterial [3].

In addition, when it is taken into account that not all conditions are the same in all parts of the body or that conditions may be changed significantly due to trauma or injury, the situation in practice is even more complex. Namely, different pH values and oxygen concentrations prevail in different parts of the body [3], [6]. Further, when the biomaterial is implanted, the imbalance in the human body is often accompanied by inflammation and infection, which can significantly change the pH value. Thus, the pH value of the human fluid can drop from 7.4 to 5.5, and it can take 10 to 15 days to recover its standard value [3]. Bacterial infection not only can lower the pH, but it may significantly raise it to the alkaline range (up to 9.0) [3].

Another problem is the reaction of the immune system to the implantation of a foreign body, which uses macrophages (cells responsible for destroying bacteria) to generate active oxygen species such as hydrogen peroxide (H_2O_2) to prevent infection [6], [34]. These reactive species can significantly weaken metallic biomaterials' passive film [34], [42], and Ti-based biomaterials are prone to dissolution under such conditions [34], [43].

Therefore, metallic biomaterials that are very corrosion-resistant and behave well under normal human body conditions might be subject to corrosion during implantation due to changing conditions. However, corrosion essentially occurs in any case when these materials are implanted in the human body, albeit very slowly at some finite rate. Thus, the acceptable corrosion rate in the literature is usually stated to be up to 1 µm/year [3], [35]. This way of expressing the corrosion rate is called the *corrosion penetration rate* (CPR) because it represents a loss-in-dimension vertical to the corroding surface per unit time [3]. Regarding the artificial human body fluids, four classes of exposure environments are distinguished: physiological, biophysiological, biological, and pericellular [6]. From the viewpoint of corrosion properties of metallic biomaterials, the physiological exposure environment is usually relevant, where inorganic chemical composition and thermal conditions are controlled to normative mammalian values. Thus, simulated body fluid (SBF) is sometimes simply a so-called physiological solution, i.e. an aqueous solution of 0.9 wt% NaCl. However, some more complex solutions include several different salts, e.g., Ringers solution, Hanks' solution, artificial saliva, etc. [6]. Hanks' solution, for instance, includes commonly eight different salts with possible variations in concentrations: NaCl, KCl, $NaHCO_3$, $CaCl_2$, $MgCl_2$, $MgSO_4$, Na_2HPO_4, KH_2PO_4, and glucose as an organic component [31]. It is assumed that it closely simulates the corrosion conditions of the human body.

1.3.2.1 Corrosion of SS316L

This is a section. Some more text. Some more text. Some more text. Some more text. Some SS316L is susceptible to localized corrosion, primarily pitting and crevice corrosion [31], [44]. One early study showed that more than 90% of the implanted SS316L showed damage due to pitting and crevice corrosion [45]. In another study, however, it was reported that in addition to local corrosion attacks, the main reason for the failure of SS316L implants

was fatigue corrosion [46]. Regarding the corrosion mechanism of SS316L, the reactions of Fe corrosion should be considered as the main component in this alloy. Assuming neutral electrolyte and the presence of dissolved oxygen, as is common in the human body, iron(III) oxide (Fe_2O_3) or hematite is formed by the electrochemical reaction that begins with the transfer of electrons from Fe to O in the environment. Therefore, the cathodic reaction is the ORR (**Eq. 1.5**). This half-cell reaction consumes electrons released by the anodic half-cell reaction of Fe oxidation to the oxidation state (+2) (**Eq. 1.8**). The coupled electrochemical reaction occurring at different sites on the same metal surface is given by **Eq. 1.9** [33], [47].

$$Fe \rightarrow Fe^{2+} + 2e^{-} \tag{1.8}$$

$$2Fe + O_2 + 2H_2O \rightarrow 2Fe^{2+} + 4OH^{-} \tag{1.9}$$

In the aqueous environment containing oxygen, the oxidation reaction of Fe continues up to the oxidation state (+3) (**Eq. 1.10**), which is necessary for the formation of the Fe_2O_3. Then, soluble Fe ions in the aqueous environment form Fe hydroxides (**Eq. 1.11 and 1.12**) [47].

$$4Fe^{2+} + O_2 \rightarrow 4Fe^{3+} + 2O^{2-} \tag{1.10}$$

$$Fe^{2+} + 2H_2O \leftrightarrows Fe(OH)_2 + 2H^{+} \tag{1.11}$$

$$Fe^{3+} + 3H_2O \leftrightarrows Fe(OH)_3 + 3H^{+} \tag{1.12}$$

Finally, in the last step, different oxides, iron(II) oxide (FeO), iron(III) oxide-hydroxide (FeOOH) and iron(III) oxide (Fe_2O_3), are formed through dehydration reactions (**Eq. 1.13 – 1.15**) [47]. Therefore, water and dissolved oxygen availability determine which corrosion product will form. Various anions, cations, and organic molecules present in the human body can also be incorporated into a mixture of Fe oxides.

$$Fe(OH)_2 \leftrightarrows FeO + H_2O \tag{1.13}$$

$$Fe(OH)_3 \leftrightarrows FeO(OH) + H_2O \tag{1.14}$$

$$2FeO(OH) \leftrightarrows Fe_2O_3 + H_2O \tag{1.15}$$

The presence of the other alloying elements in SS316L that can also be released into the body should also be considered. Ni is known for its allergenicity and can cause dermatitis and skin rashes [28], [29]. The other element that is also problematic is Cr; it is also an allergen and causes ulcers and nervous system disorders [35]. However, Cr is essential for the passivity of stainless steel. The inner layer of the passive film is rich in a mixture of Cr(III) and Fe(II,III) species, while the outer layer is mainly enriched in Fe (II,III) species [13], [48]. In addition, oxides of other elements (Ni, Mo, Mn) may also be present in the passive film [13].

1.3.2.2 Corrosion of cp-Ti

Although cp-Ti is very resistant to corrosion due to the natural formation of a passive film, it is susceptible to fatigue and fretting corrosion [35]. Both *in vitro* and *in vivo* experiments showed that H_2O_2 may cause the release of Ti ions from cp-Ti due to hyper oxidation of its surface [32], [42], [43]. In addition, Ti passivity can be destroyed by the action of F ions, which in interaction with Ti form aqueous complexes [49]. This problem mainly relates to using Ti and its alloys in orthodontics due to the addition of F ions in toothpastes [49], [50].

Generally, Ti passive film consists of an inner layer that is compact near-stochiometric titanium (IV) oxide (TiO_2), while the outer layer is a mixture of some Ti oxide-hydroxides and hydrates, which is defective, porous and rich in water [51]. Dissolution of TiO_2, which has a protective role, has been proposed to occur via chemical or electrochemical dissolution. Chemically, when Ti is present in a strong and reducing acid, its passive film is reduced to Ti oxidation state (+3) (**Eq. 1.16**) [52]. On the other hand, electrochemically, it has been proposed that Ti in the passive film is reduced to (+3) in the form of Ti oxide-hydroxide (TiOOH) (**Eq. 1.17**), followed by its dissolution (**Eq. 1.18**) [53], [54].

$$TiO_2 + H_2O + H^+ \rightarrow Ti(OH)_3^+ \tag{1.16}$$

$$Ti + 3TiO_2 + 6H_2O \rightarrow 4TiOOH \cdot H_2O \tag{1.17}$$

$$TiOOH \cdot H_2O + 3H^+ \rightarrow Ti^{3+} + 6H_2O \tag{1.18}$$

In oxidizing conditions, the pure Ti is gradually oxidized to oxidation state (+3) (**Eq. 1.19**), and then with presence of more dissolved oxygen, it goes up to (+4) (**Eq. 1.20**) [55]. The Ti^{4+} ion is subsequently hydrolyzed to form hydrated Ti oxide (**Eqs. 1.21 and 1.22**) [56], followed by the formation of less hydrated Ti oxide and finally insoluble TiO_2 (**Eq. 1.23**) [57], [58], i.e. re-passivation occurs. Therefore, Ti may be corroded in strongly reducing acids by reducing its passive layer, but it tends to re-passivate in the presence of oxygen [49].

$$Ti \rightarrow Ti^{3+} + 3e^- \tag{1.19}$$

$$Ti \rightarrow Ti^{4+} + 4e^- \tag{1.20}$$

$$Ti^{4+} + 2H_2O \rightarrow [Ti(OH)_2]^{2+} + 2H^+ \tag{1.21}$$

$$Ti^{4+} + 4H_2O \rightarrow Ti(OH)_4 + 2H^+ \tag{1.22}$$

$$Ti(OH)_4 \rightarrow TiO_{2-x}(OH)_{2x} + (2-x)2H_2O \tag{1.23}$$

In addition to good insulating properties, Ti passive film stimulates the precipitation of Ca phosphates [25]. This is a very important process as it results in hydroxyapatite formation [59], one of the principal components of bone, and it allows good biocompatibility of Ti-based materials [25]. However, regardless of the good biocompatibility and corrosion resistance of cp-Ti, possible cases of its corrosion should also be considered. Typical

consequences of cp-Ti corrosion are bone loss due to inflammatory reactions, hypersensitivity and allergies to released Ti ions, and yellow nail syndrome [60].

1.4 Biocompatibility and Antibacterial Properties of Biomaterials

In addition to corrosion resistance closely related to biocompatibility [61], antibacterial properties of the biomaterial are also often desired. When a biomaterial is implanted, there is a competitive process where host and pathogenic cells, i.e. bacteria, attempt to colonise its surface, also called "race for the surface" [62].

1.4.1 Biocompatibility of biomaterials

The main requirement for using a biomaterial has long been the need for it to be safe and completely inert in the biological environment and that it should not affect the environment itself. This concept of biocompatibility has resulted in selecting a group of metallic, ceramic and polymeric biomaterials that are widely used today [63]. However, in practice, biocompatibility is far more complex. One of the recent definitions of biocompatibility is "the ability of a biomaterial to perform its desired function for a medical therapy, without eliciting any undesirable local or systemic effects in the recipient or beneficiary of that therapy, but generating the most appropriate beneficial cellular or tissue response in that specific situation, and optimizing the clinically relevant performance of that therapy" [64]. According to this definition follows that a certain degree of biological activity is needed for biomaterials. Bioactivity is necessary for tissue engineering, drug and gene delivery systems, and generally where interactions between biomaterials and tissue components are essential.

When a biomaterial is implanted *in vivo*, it induces a cascade of reactions in the biological micro-environment through the interaction with body fluids, proteins and various cells [25]. The sequence of local events often leads to the classic foreign body response, which develops a fibrous collagen sheath, which encapsulates the implant and separates it from the normal tissue. The two crucial factors that manage a host response to implantation of a biomaterial are the chemical composition and surface topography. Therefore, they regulate processes such as adsorption of ions and biomolecules such as proteins, formation of calcium phosphate layers, and interaction with different types of cells (e.g. macrophages, osteoblasts and fibroblasts) [25], [63], [65]. The nature of the initial interface between a biomaterial and tissue or bone determines an implant's ultimate success or failure.

The most conducted biocompatibility tests for materials for implantation are cytotoxicity tests. These are often done *in vitro* exploring fibroblast cells, which are the cells of connective tissue and play a critical role in wound healing, and osteoblast cells, which are responsible for bone synthesis. Mesenchymal stem cells (MSCs) might also be used for biocompatibility tests. These are adult stem cells and are isolated from different tissue of mammals, e.g. bone marrow and adipose tissue. Since they are multipotent cells, they can give rise to developing adipogenic (fat), chondrogenic (cartilage), osteoblastic (bone), myoblastic (muscle) and fibroblastic (connective tissues) cells [65]. Although human cells are also used, these cells are commonly derived from animal models [65]. The behavior of these cells in contact with the test biomaterial can be assessed using liquid extracts of the biomaterial or directly on the metal surface. The evaluation is usually performed by fluorescence spectroscopy and fluorescence microscopy using fluorescent substances for staining and detecting cell nuclei and their cytoskeleton.

1.4.2 Antibacterial properties of biomaterials

Antibacterial surface implies the ability to resist the initial attachment of bacteria by either exhibiting an antiadhesive or bactericidal effect. Antiadhesive surfaces may resist bacterial attachment due to specific surface physical properties, such as topography or surface energy, which are unfavorable for bacteria attachment. Antiadhesive surfaces can be hydrophilic but also superhydrophobic. The adsorption of surface protein and bacterial adhesion can be managed by controlling the electrostatic properties. On the other hand, bactericidal surfaces may disrupt the physiological functions of bacteria, causing their death due to their chemical composition or the presence of chemical agents [66].

Upon implantation, materials may be contaminated by skin colonizing bacteria or bacteria present in the blood or body fluid coming from an infection in another part of the body. These bacteria adhere to the material's surface to derive nutrients and as a self-preservation strategy to evade an immune response. The main factor in bacteria attachment and biofilm formation is a thin layer of proteins that rapidly forms on the implant's surface after implantation. Therefore, the ideal implant surface should inhibit nonspecific protein adsorption and bacterial adhesion while promoting or even selectively promoting cellular adhesion, depending on the application [67]. Namely, as most bacteria have a net negative charge on the outer membrane, adhesion of bacteria is discouraged on negatively charged surfaces and promoted on positively charged surfaces [68], [69]. However, it also depends on the biological characteristics of the bacteria, i.e. Gram-positive or Gram-negative bacteria and their size, shape and adhesins present on the bacterial surface [70].

The formation and development of bacteria and biofilm on implanted biomaterial consists of four steps. In the first step, bacteria are brought into contact with the surface by gravitational forces, Brownian motion or hydrodynamic forces. The biofilm, which consists of adhered bacteria and extracellular polymeric substances, is formed in the second step. Then, in the third step, the further development of the biofilm consists of the proliferation of adherent bacteria and, in most cases, the synthesis of the biofilm matrix. The fourth step relates to the maturity of the biofilm and is associated with a specific bacterial metabolism and physiology [70]. Essentially, the biofilm formation is influenced by the topographical and chemical features of the implant surface. Regarding the surface topography and roughness, it is worth noting that the roughness on the macroscopic, micro-meter and nano-meter scale can have different effects. In this regard, it has been reported that many bacteria favored micro-meter-sized concave features such as surface valleys, depressions, pits, and edges [67], [71].

The suppression of implant infection relies either on the bactericidal properties of the surface or its surface energy and roughness [66]. In the literature there are studies, which are still not in the clinical phase, for incorporation of various bactericidal agents (e.g. antibiotics, silver, titanium and fluoride ions) into a particular coating [66], [67], [72]. For example, it has been reported in many studies that silver is a very effective bactericide with activity against a wide variety of bacteria, such as *Pseudomonas aeruginosa*, *Staphylococcus aureus*, *Staphylococcus epidermidis* and *Escherichia coli* [66]. These strains are relevant for surgical infections. On the other hand, modification of surface topography is carried out by various physical techniques for production of anti-bacterial surfaces that do not necessarily change the chemical composition of the surface [70].

To summarize, it is challenging to develop a biomaterial with excellent antibacterial properties without compromising biocompatibility. Furthermore, considering the previously described requirements related to corrosion and mechanical properties of materials, the challenge is even more significant.

1.5 Surface Treatment Processes

Many different techniques have been developed to modify biomaterials' surfaces and increase their functionality and lifespan. These techniques can be divided to improve biocompatibility, corrosion, and wear properties of specific biomaterials [7].

A technique known to improve the wear resistance of biomaterials is ion implantation which takes place without modifying the surface finish or the bulk properties of the material [73]. For biomedical purposes, the implantation of N ions was usually applied to both SS316L and cp-Ti [73], [74]. Surface texturing techniques that modify the material surface, most often by changing roughness, include plasma treatment, electropolishing, anodic oxidation, sandblasting and acid etching [7]. These techniques mainly focus on improving biocompatibility and antibacterial properties [7], [70].

Another way to improve the surfaces of metallic biomaterials can also be performed by simply depositing a thin coating or film over the material's surface. In this way, the release of harmful metal ions into the surrounding tissue can be effectively prevented, i.e. the occurrence of corrosion can be minimized. Some of the thin film deposition techniques are: physical vapor deposition (PVD) such as sputtering [75] and ion beam deposition [76], chemical vapor deposition (CVD) [77], pulsed laser deposition (PLD) [78], sol-gel dip deposition [79], electrodeposition [80], etc. [3], [7]. They are mainly used for the deposition of synthetic Ca hydroxyapatite, with a complex formula $Ca_{10}(PO_4)_6(OH)_2$, which is characterized by the ability to form direct bonding with surrounding bone or tissue [81]. Hydroxyapatite and similar phosphate materials simulate the naturally formed hydroxyapatite in the human body and have excellent biocompatibility [73].

Further, another interesting materials for modifying the biomaterial's surface are various ceramic materials. For example, alumina (Al_2O_3) has been used for a long time in biomedicine in bulk form. In addition, it has also been used in the form of a coating after deposition on Ti-based implants in metallic form and anodically oxidized [82], [83]. Some of the other ceramic materials that have found application as biomaterials are titania (TiO_2), zirconia (ZrO_2), titanium nitride (TiN), zirconium nitride (ZrN), silicon nitride (Si_3N_4), titanium-niobium nitride (TiNbN) and diamond-like carbon (DLC) [83]. The main reason for using ceramic materials for implantation is their tendency to be a suitable substrate for forming natural hydroxyapatite after implantation [84], [85]. In addition, various ceramic materials in the form of a coating can provide corrosion protection of metallic biomaterials due to their insulative properties [83]. One technique that is still under development and offers the possibility of deposition of various ceramic materials is atomic layer deposition (ALD) [86].

1.5.1 Atomic layer deposition

The atomic layer deposition (ALD) technique that was developed in the 1960s and 1970s is a member of the widely used chemical vapor deposition (CVD) techniques and was initially commercialized for the production of thin films in microelectronics [87], [88]. Interest in this technique came from the possibility of forming thin, nanometric films with high thickness uniformity and conformity on very complex nano-shaped surfaces or even inside nano-porous materials [89], [90]. This feature can be crucial for some applications in biomedical engineering and biotechnology [91]. Another feature of ALD is the possibility of forming defect- and impurity-free films based on a pure gas-to-solid chemical reaction, which is crucial in corrosion protection [92].

A schematic illustration of the ALD process is shown in **Fig. 1.4** on the example of alumina. The process consists of four steps:

- In the first step, a first gaseous precursor is introduced into the reaction chamber and produces a monolayer of the first precursor on a substrate surface. Herein, aluminum(III) chloride ($AlCl_3$) is taken as an example. Consequently, hydrogen chloride (HCl) is released as a by-product.
- Then, the chamber is purged with neutral gas (e.g. nitrogen or argon) to remove the excess unreacted and unbound precursors and by-products.
- In the third step, a second gaseous precursor, usually an oxidizing precursor such as water (H_2O) in this case, is introduced in the chamber and reacts with the first deposited precursor through a surface chemical reaction.
- Finally, the chamber is purged again to remove the unreacted second precursor and by-product of the chemical reaction, i.e. HCl, as in the first step. It results in a monolayer of pure alumina (Al_2O_3) deposited in the solid state on the substrate.

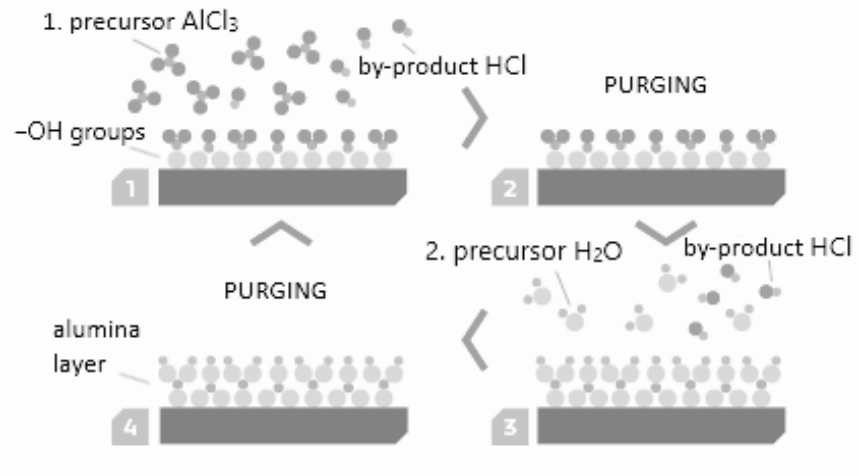

Figure 1.4: Schematic illustration of the ALD process on the example of alumina formation.

By repeating this cycle, the thin film is formed layer by layer, so it is usually said that ALD thin film grows in a self-limiting manner. Due to this, it is possible to obtain a nanometrically accurate thickness of the desired deposit on a suitable substrate by controlling the number of cycles. Essentially, the whole process is based on the surface gas-to-solid chemical reaction, which in the case of alumina deposition, can be expressed by **Eq. 1.24**.

$$2AlCl_{3(g)} + 3H_2O_{(g)} \rightarrow Al_2O_{3(s)} + 6HCl_{(g)} \tag{1.24}$$

The first precursor should be efficiently adsorbed by physical or chemical bonds on the substrate surface [88]. In the case of chemical bonds, i.e. chemisorption, which is desirable due to their strong bonding, this first step usually occurs on the hydroxyl groups (–OH) present on the surface of the desired substrate. Therefore, each cycle of the ALD reaction is a two-step process because, firstly, the first precursor is bound to the surface, then the second oxidizes it and so forth.

Depending on the precursors used, the ALD reaction can occur under certain pressure and temperature conditions. Thus, typical values of pressure and temperature during the ALD process are between 1 and 10 mbar, and from 100 °C to 500 °C, respectively [88]. Temperature is of particular importance because it crucially affects the feasibility of a particular ALD process. **Fig. 1.5** presents the so-called *temperature window* diagram,

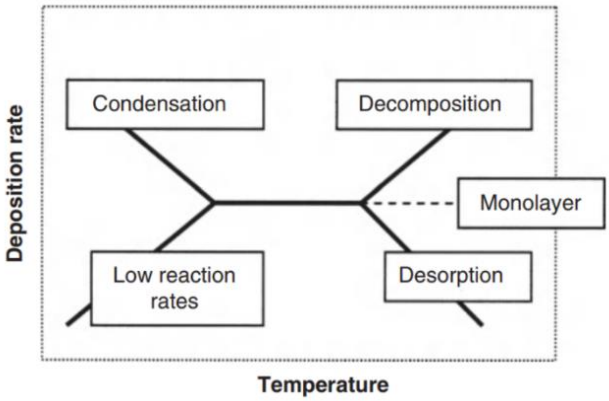

Figure 1.5: Temperature window for ALD process [88].

where the deposition or growth rate is shown as a function of temperature. If the temperature is very high, then the first precursor may be decomposed on the surface before having time to react with the second precursor. Alternatively, if the first precursor is stable, it may still be desorbed from the surface before having the chance to react with the second precursor.

On the other hand, if the temperature is too low, the precursor could be adsorbed into more than one monolayer per cycle (or even condensed into liquid or solid on the surface). Finally, at low temperatures, the reaction rate may be so slow that the reaction time may be too long (e.g. hours) compared to the reasonable ALD cycle time (e.g. seconds), i.e. there is no time to form a monolayer [88]. Therefore, precursors can form monolayers in a specific temperature range by gas-to-solid chemical reaction and produce an ALD thin film. For this reason, the suitability and properties of the ALD precursors are another aspect of the ALD technique that should be considered.

Because of the sequential nature of ALD, precursors can be divided into metal-containing precursors (or precursors that contain an element of interest) and non-metal precursors used for oxidation or reduction of the first precursor. The metal-containing precursors are mostly inorganic coordination complexes with a metal center surrounded by ligands and organometallic compounds. Some of the commonly used complexes in ALD processes are halides, alkoxides, carbonyls and N-coordinated compounds (e.g. amides, amidinates), while organometallic precursors are mostly metal alkyls and cyclopentadienyl-type compounds [93]. The most widely used and most researched ALD process is between aluminum alkyl, trimethylaluminum ($Al(CH_3)_3$ or TMA) and water [94]. Regarding the non-metal precursors, the most used oxidizing precursors for metal oxides deposition are H_2O, H_2O_2, N_2O_4, N_2O, O_2 and O_3, the choice of which depends on the selected metal precursor. In the simplest case, H_2O is used as an oxygen source, and indeed it often readily reacts with many metal halides, alkyls, and alkoxides. In a non-oxidizing regime, hydrogen gas (H_2) is perhaps the most widely used reducing agent, but it is quite inert to typical metal precursors and relatively high deposition temperatures are needed to maintain ALD reactions [88]. In addition, it is good to note that modifications of ALD allow the reaction to be carried out at room temperature by so-called *energy-enhanced* ALD. The most common modifications are plasma or UV light, which provide reactive species in ALD processes [93].

1.5.1.1 Atomic layer deposition for biomedical applications

The first proposal on using ALD thin films for biomedical implants appeared in the patent from 2006 [95], while the first article that considered the application of ALD thin films in corrosion protection was published in 1999 [92]. Today, due to the many advantages, it is researched more and more as a technique for various applications in medicine and biotechnology [91], [96]. It has been proposed that ALD thin films of various materials could impart biologically relevant surface properties such as biocompatibility, bioactivity, electrical properties, and optical properties [91]. For example, due to the excellent control of thin-film thickness and the possibility of low-temperature deposition of high-quality thin films, ALD films have been proposed for use in biosensors, bioassays and different bioelectronic applications [91]. Further, as different ceramic materials have been shown to have biocompatible behavior when implanted, many studies have focused on modifying implant materials by ALD ceramic thin films to improve their biocompatibility [96]. Since biocompatibility and corrosion properties are closely related, ALD functional thin films have also been studied as corrosion protection for various orthopedic, dental and cardiovascular implants [96].

1.6 Literature Review

In general, ALD alumina thin films have been investigated on different substrates for protection against corrosion under different conditions [92], [97]–[102], including biomedical applications. As presented above, once implanted, biomaterials such as cp-Ti and SS316L, during their implant lifetime, are susceptible to dissolution and associated with the release of potentially harmful metal ions into the body. Hitherto published studies on ALD films, aiming for the protection of different biomaterials, have been focused mainly on thin films from alumina (Al_2O_3) [103]–[106] and zirconia (ZrO_2) [107]–[109], and from bioactive titania (TiO_2) [108], [110], [111] and hydroxyapatite (HA) [112]. Alumina used as a bulk implantable material has a corundum-like structure, i.e. crystalline α-Al_2O_3, which allows its excellent stability and usability as an implant material for many years [113], [114]. Besides, it is known as a ceramic material with excellent biomechanical and biocompatible properties [82], [115]–[117]. However, alumina obtained in the form of a thin film by the ALD method, especially at temperatures below 600 °C, is always amorphous and can have significantly different properties than in the bulk form [118], [119]. In one study, ALD alumina was reported to be a suitable substrate for growing human coronary artery smooth muscle cells [104]. Additionally, the possibility of functionalizing its surface with hydrophilic or hydrophobic molecules, which can be used to control cell development, was emphasized.

Unlike alumina, which has been extensively researched and applied in biomedicine, another ALD metallic oxide, hafnium(IV) oxide (hafnia HfO_2), has not been studied frequently for similar purposes. It has been widely investigated for electronic applications as a dielectric or high-κ material [120] obtained by the ALD [121], [122], and by other methods [123], [124]. Only one short conference paper about ALD hafnia for biomedical purposes has been published, but it dealt only with antibacterial properties on different bacterial strains [125]. It has been shown that hafnia and zirconia (zirconium(IV) oxide, ZrO_2) have better antibacterial properties compared to alumina and titania [125]. Essentially, there is only one published paper on the potential use of hafnia coating for biomedical purposes, but it has been obtained by anodic oxidation [126]. It has been reported that hafnia possesses good cytocompatibility and affinity for proteins, and with an enhanced antibacterial effect [126]. There are several studies on pure metal Hf as an alternative metal in biomedical applications; it is much heavier but chemically very similar

to Ti, and analogously passivated with a protective layer of the hafnia. *In vivo* experiments showed that Hf when implanted in a mammal's tissue, have the same response as Ti [127]. Another study showed that Hf has good biocompatible and osteoconductive behavior [128], which refers to bone growth in contact with the implant. The protective properties of hafnia ALD thin films have been scarcely researched but have good insulating and barrier properties due to its high dielectric properties [99]. Also, an interesting feature of the ALD hafnia thin film is that crystallinity of the amorphous hafnia increases with increasing deposition temperature in the range of 100 to 350 °C [129], [130]. This property can be used in this convenient range of temperatures to easily control the crystallinity and, consequently, other properties related to surface protection.

One of the ideas that often appeared in the research of ALD films as a means of corrosion protection is the combination of different metal oxides in one film, i.e. multilayer structure of a thin film, aiming to exploit good properties of both types of oxides. Studies have been performed on a combination of amorphous alumina and polycrystalline titania ALD multilayers deposited on stainless steel [92], [97], [103] and copper [98]. The authors reported improved barrier properties in different corrosive environments compared to their single-layer variants in all these cases. As an explanation for the efficiency of ALD multilayer films, it is proposed that the combination of the amorphous layer, e.g. alumina, and polycrystalline layer, e.g. titania, provides good protective properties due to the combination of good barrier properties of uniform amorphous layer and good chemical stability of polycrystalline layer [92], [97].

1.7 Structure of the Thesis

This thesis is divided into four studies. The first three have already been published in the form of original scientific papers, given as references:

1. Study 3.1 – The effect of cp-Ti surface preparation on the protective properties of ALD Al_2O_3 and HfO_2 films [131].
2. Study 3.2 – The effect of thickness of ALD Al_2O_3 films deposited on cp-Ti and SS316L on their protective properties [132].
3. Study 3.3 – The effect of ALD multilayer structure Al_2O_3-HfO_2-Al_2O_3 deposited on cp-Ti and SS316L on their protective properties [132].
4. Study 3.4 – Biocompatibility and antibacterial properties of ALD Al_2O_3 and HfO_2 thin films deposited on cp-Ti and SS316L.

The following hypotheses were postulated in the thesis:

1. The smooth surface of metal substrates, SS316L and cp-Ti, allows the formation of higher quality alumina and hafnia ALD thin films, in terms of surface protection and barrier properties, than the rough surface.
2. The thickness of ALD thin films is critical for providing barrier corrosion protection.
3. The protective properties of multilayer ALD thin films, obtained by combining alumina and hafnia, are improved compared to a single layer of pure alumina ALD thin film of the same thickness on both substrates SS316L and cp-Ti.
4. Alumina and hafnia ALD thin films have better biocompatibility and antibacterial properties than metal substrates, SS316L and cp-Ti.

Chapter 2

Materials and Methods

2.1 Specimen Surface Preparation

SS316L and cp-Ti specimens in the shape of the disc of 2.0 mm in thickness and 15 mm in diameter, supplied by GoodFellow Cambridge Ltd., were used as substrate materials. The cp-Ti was grade 2, with a high purity of 99.6%, and SS316L with the composition of the main alloying elements as follows: 18 wt.% Cr, 10 wt.% Ni and 3 wt.% Mo, rest Fe, as reported by the supplier.

Both materials were polished until a mirror-like surface appearance. The polishing procedure consisted of two steps: 1st – grinding with 500-grit SiC emery papers, and 2nd – polishing with silica (SiO_2) suspension (OP-S) with a particle size of 0.25 μm, with the addition of the chemical reagents, 30% H_2O_2 and 25% NH_4OH (Merck KGaA). Following the polishing step, specimens were cleaned in 99.6% ethanol (Merck KGaA) using an ultrasonication bath Elmasonic P series (Elma Schmidbauer GmbH) for 15 min and then dried with high-pressure nitrogen gas. This polishing procedure was used for all studies. Exclusively, in study 3.1. cp-Ti specimens were also used as roughly ground. The grinding was performed using 500-grit SiC papers until a uniform surface was achieved.

All specimens, ground or polished, were, before the ALD deposition processes, stored overnight (ca. 16 h) in a vacuum desiccator filled with commercial hygroscopic silica gel to ensure uniform surface conditions. As an additional substrate for ALD depositions, Si-wafers coated with a 450 nm thick SiO_2 thermal oxide were used as control specimens due to their perfect smoothness.

2.2 ALD Deposition Processes

A TFS 200 system by Beneq Oy, was used to deposit alumina (Al_2O_3) and hafnia (HfO_2) thin films of different thicknesses in single and multilayer combinations. Alumina was deposited using trimethylaluminum ($Al(CH_3)_3$ or TMA (**Fig. 2.1 a**), 99.99% PURATREM, STREM Chemicals Inc.) as the first precursor. Hafnia was deposited using tetrakis(ethylmethylamido)hafnium(IV) ($Hf[N(CH_3)(C_2H_5)]_4$ or TEMAH (**Fig. 2.1 b**), 99.99% PURATREM, STREM Chemicals Inc.) as the first precursor. Milli-Q water (resistivity 18 MΩ cm^2 at 25 (C, Billerica, MA) was used as the second precursor for both types of thin films.

For alumina thin films, the ALD cycle consisted of a 0.35 s TMA dose, a 1 s N_2 purge, a 0.3 s water dose and a 1 s N_2 purge, and with an expected growth rate per cycle (GPC) of 1 Å/cycle on a smooth surface. For hafnia, the ALD cycle consisted of a 0.5 s TEMAH

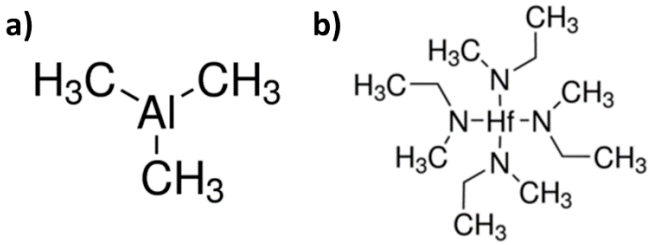

Figure 2.1: Structure formulas of ALD precursors **a)** TMA and **b)** TEMAH.

dose, a 1 s N_2 purge, a 0.2 s water dose and a 1 s N_2 purge, and with an expected GPC of 0.96 Å/cycle on a smooth surface.

Depending on the experimental goals in each study, depositions were performed at different numbers of cycles, i.e. different thicknesses of alumina and hafnia were deposited, respectively, and at different temperatures. **Table 2.1** shows how many ALD cycles were used, what film thicknesses were expected for each study, respectively, and at what temperatures the depositions were performed. The table highlights in yellow the parameters related to the deposition of multilayer films as a combination of alumina and hafnia layers. Multilayer structure consists of 20 nm hafnia layer in a sandwich of two alumina layers of 20 nm. Expected thicknesses for all ALD films were calculated according to previous depositions on Si-wafers (not published) and GPC values for alumina and hafnia, respectively. In study 3.4, deposition was performed at two different temperatures as stated, and therefore the thicknesses of ALD films may vary significantly from expectations.

As substrates, cp-Ti specimens were used in study 3.1, while in all other studies both cp-Ti and SS316L specimens were used. Additionally, Si-wafers were used as control

Table 2.1: ALD parameters for alumina, hafnia and multilayer thin films in each study. Parameters related to multilayer thin films are marked yellow.

	Alumina depositions			Hafnia depositions		
	No. of cycles	Expected thickness (nm)	Temp. (°C)	No. of cycles	Expected thickness (nm)	Temp. (°C)
Study 3.1	1000	100 nm	160	1050	100	180
Study 3.2	200	20	180	–	–	–
	600	60				
Study 3.3	600	60	180	*210	*20	*180
	*200 + 200	*20 + 20	*180			
Study 3.4	600	60	180	630	60	180
			260			260

specimens, as will be described below. Exceptionally in studies 3.2. and 3.3 one group of the specimens was prepared for cross-section study and surface thickness evaluation. The latter specimens were partially masked with adhesive, heat-resistant tape to disable ALD deposition on one part of the surface, thus creating a sharp ALD step after adhesive tape removal. In **Table 2.2**, the abbreviated names of all specimens in all four studies are given to simplify the interpretation of the results.

Table 2.2: Abbreviated specimen names for all four studies.

<table>
<tr><td rowspan="2">Study 3.1</td><td>Ti-500</td><td>Ground cp-Ti specimens</td><td colspan="2" rowspan="2">1h-40d refers to immersion time for long-term measurements</td></tr>
<tr><td>Ti-OPS</td><td>Polished cp-Ti specimens</td></tr>
<tr><td rowspan="3">Studies 3.2 and 3.3</td><td>Ti-20AL and SS-20AL</td><td colspan="2">cp-Ti and SS316L coated with ca. 20 nm of Al_2O_3 thin film</td><td rowspan="3">1h-30d refers to immersion time for long-term measurements</td></tr>
<tr><td>Ti-60AL and SS-60AL</td><td colspan="2">cp-Ti and SS316L coated with ca. 60 nm of Al_2O_3 thin film</td></tr>
<tr><td>Ti-60ML and SS-60ML</td><td colspan="2">cp-Ti and SS316L coated with ca. 60 nm of multilayer thin film</td></tr>
<tr><td rowspan="2">Study 3.4</td><td>Ti-AL180 and SS-AL180
Ti-HF180 and SS-HF180</td><td colspan="3">cp-Ti and SS316L coated with alumina (AL) or hafnia (HF) at 180 °C</td></tr>
<tr><td>Ti-AL260 and SS-AL260
Ti-HF260 and SS-HF260</td><td colspan="3">cp-Ti and SS316L coated with alumina (AL) or hafnia (HF) at 260 °C</td></tr>
</table>

2.3 Electrochemical Measurements

All electrochemical measurements were performed using potentiostats/galvanostats with electrochemical impedance modulus, Autolab PG STAT 302N, PG STAT M204 and PG STAT 12, controlled by Nova 2.1.4 software and supplied by Metrohm AG. The standard three-electrode system was used with an Ag/AgCl (3 M KCl) electrode ($E = 0.192$ V vs. SHE) as the reference electrode and a carbon rod as the counter electrode. The specimen, serving as a working electrode, was tightened in a suitable Teflon holder with a 1 cm^2 area exposed to the electrolyte solution. All the potentials in the text are given with respect to the Ag/AgCl electrode. To simulate human body conditions, the electrochemical tests were performed in an Autolab 400 mL corrosion cell thermostated at 37 ± 0.1 °C (**Fig. 2.2**), with Hanks' solution as the electrolyte with a pH of 7.4. All chemicals used to prepare the Hanks' solution were of p.a. purity and were supplied by Merck and Sigma-Aldrich, and its composition is shown in **Table 2.3**.

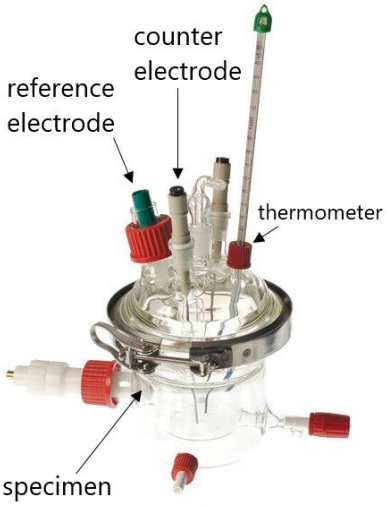

Figure 2.2: Thermostated 400 mL corrosion cell with a three-electrode system.

Table 2.3: Chemical composition of the Hanks' solution.

Components	γ (g dm^{-3})
NaCl	8.0
KCl	0.40
$NaHCO_3$	0.35
$CaCl_2$	0.14
$MgCl_2 \cdot 6H_2O$	0.10
$MgSO_4 \cdot 7H_2O$	0.06
$Na_2HPO_4 \cdot 2H_2O$	0.06
KH_2HPO_4	0.06
Glucose	1.0

2.3.1 Potentiodynamic polarization

PDP tests were performed slightly differently depending on the objectives of each study. In study 3.1, after stabilization of OCP values for 1 hour, PDP measurements were performed from −0.1 V vs OCP (i.e. from the cathodic region) to 4.0 V vs OCP in the anodic direction by a scan rate of 1 mV/s.

In studies 3.2 and 3.3, cyclic PDP tests were performed whose procedures differed for SS316L and cp-Ti. First, as in the previous case, all specimens were allowed to rest and stabilize for 1 h at the OCP, and the polarization scan rate was the same, 1 mV/s. For SS316L, polarization started at −0.1 V vs OCP up to a threshold current density, i.e. when the current density has increased by one order of magnitude following the breakdown (E_b) of the native passive film. After reaching the threshold, the reverse potential scan (E_v) was applied. For ALD-coated SS316L specimens, E_v was set at the point at which current

density increased for two orders of magnitude above E_b. For cp-Ti specimens, cyclic PDP procedures were the same for bare, and ALD-coated specimens: from −0.1 V vs OCP up to 4.0 V followed by applying a reverse potential scan.

2.3.2 Electrochemical impedance spectroscopy

Unlike PDP tests, EIS procedures were essentially the same in all studies. First, specimens were allowed to rest and stabilize for 1 h at the OCP. Then, EIS tests were performed from 100 kHz to 1 mHz with an AC excitation voltage of 10 mV around OCP, resulting in 7 points per frequency decade. In study 3.1, the measurements were carried out after specific immersion times: 1 hour, 1 day, 5 days, 15 days and 40 days. In studies 3.2 and 3.3, measurements were performed after immersion times: 1 hour, 1 day, 5 days, 15 days and 30 days, except if the film showed significant changes in barrier properties at another immersion time, as stated in the text.

Because EIS measurements were considered non-destructive, PDP measurements were performed after 40 days (study 3.1) and 30 days (studies 3.2 and 3.3) of immersion. These results have been compared to those PDP tests recorded after 1 h of immersion (the stabilization at OCP). The same procedures were used for these PDP tests as described in Section 2.3.1. The theoretical backgrounds of both techniques, PDP and EIS, are given in Appendix A.

2.4 Characterization Techniques

2.4.1 Stylus profilometry

The profilometry method determined 3D surface imaging and the roughness of the prepared specimens (Bruker DektakXT). The stylus radius was 2 µm, and the applied force was 1 mg. 3D map resolution was 2 µm/trace and scanned on a surface area of 1 × 1 mm. The Bruker Vision 64 and TalyMap Gold 6.2 software were used to create 3D surface topography and calculate the mean surface roughness. According to **Eq. 2.1**, the parameter arithmetic average height (Sa) is used to evaluate the surface roughness of the 3D profiles [133].

$$S_a = \frac{1}{l_x}\frac{1}{l_y}\int_0^{l_x}\int_0^{l_y} |z|\, dx\, dy \tag{2.1}$$

where l_x and l_y are relative lengths of the profiles in x and y directions, respectively.

2.4.2 Ellipsometry

The thicknesses of the ALD films were determined using the ellipsometry method (Accurion Nanofilm_ep3se). The specimens were illuminated with a laser beam at a wavelength of 610 nm. The measurements were performed using a range of incidence angles from 45° to 66°. The experimental data were fitted according to the Cauchy model to determine the thickness, using the EP4 modelling software by Accurion. Ellipsometry measurements were performed in studies 3.1 – 3.3 on Si-wafers, considered as perfectly smooth surfaces, and on ALD-coated cp-Ti specimens in air.

2.4.3 Scanning electron microscopy and energy-dispersive X-ray spectrometry

Morphological features and chemical composition were investigated using a scanning electron microscope (SEM) and equipped with an energy-dispersive X-ray spectrometer (EDXS):

- Field-emission SEM (Fe-SEM) JEOL JSM-7600F and EDXS Oxford Instruments INCA.
- SEM Carl Zeiss EVO-40 and EDXS Oxford Instruments INCA.
- FE-SEM JEOL SM-7610F Plus equipped with EDXS Oxford Instruments INCA.
- Quanta 400 FEG ESEM equipped with EDXS EDAX Genesis X4M.

In studies 3.1 – 3.3., SEM imaging and EDXS analyses were performed at beam acceleration voltages from 1 kV to 5 kV to gather information on the topmost surface of the ALD films. Different types of detectors inside SEM were used; for secondary electrons (SE) to obtain insights into the morphology of the specimen surfaces and for back-scattered electrons (BSE) to get information on the composition. The EDXS analysis should be considered a semi-quantitative technique since the interaction volume is higher than the film thickness. The depth at which analysis took place was simulated using CASINO software v2.48 (monte CArlo SImulation of electroN trajectory in sOlids).

2.4.4 Focused ion beam

Cross-section surfaces were obtained using a focused ion beam (FIB) instrument (FEI Helios 650 Nanolab and EDXS Aztek) with Ga^+ ions as etching beam (study 3.1). Before analysis, a 1 μm thick Pt protective layer was deposited over the cross-section site as an additional protective layer. The cross-section was then made by rough etching of ALD thin films followed by fine polishing using a lower current. Then, the cross-section images were taken by SEM to check the homogeneity and thickness of the films.

2.4.5 Time-of-flight secondary ion mass spectrometry

In study 3.1, time-of-flight secondary ion mass spectrometry (ToF-SIMS) (IonToF ToF-SIMS 5) was employed to reveal the chemical composition of thin films. The analyses providing the depth profiles of the thin films were obtained using a beam of Bi^+ ions of 30 keV and 1 pA delivered over a 50 × 50 μm area of the specimen surface. The sputtering of the thin films was performed by using an O^{2+} sputtering ion beam of 2 keV and 545 nA over a 400 × 400 μm area and by Ar^+ sputtering ion beam of 2 keV and 380 nA over the same surface area. Considering the nanometric thickness of the films, only Si-wafers were used as substrates aiming to provide a very sharp interface substrate/ALD film and, consequently, more accurate and precise characterization.

2.4.6 X-ray photoelectron spectroscopy

X-ray photoelectron spectroscopy (XPS) (Physical Electronics PHI-TFA XPS) surface analysis was used in studies 3.2 and 3.3. The analyzed area was 0.1 $mm^{2,}$ and the depth analysis was 3–5 nm. As the source of X-rays, a monochromatic Al emitting photon at an energy of 1486.6 eV was used. Depth profile analysis was obtained using a 1 keV Ar^+ ion beam rastering over an area of 3 × 3 mm, with a sputtering rate of 1.0 nm min^{-1}. XPS spectra were analyzed by Multipack V8.1 C software (Physical Electronics Inc.) and normalized relative to the C 1 s peak at 284.8 eV.

2.4.7 Atomic force microscopy and scanning Kelvin probe force microscopy

Atomic force microscopy (AFM) (Digital Instruments Nanoscope IIIa Multimode) coupled with scanning Kelvin probe microscopy (SKPFM) were performed in the air at 25 ± 1 °C with an approximate relative humidity of 28%, with a pixel resolution of 512 × 512, zero-bias voltage, and a scan frequency rate of 0.2 Hz (study 3.2). Surface morphology and Volta potential difference (VPD) of prepared specimens were analyzed, specifically on specimens prepared with an ALD step, as described above. In the first scan, AFM topography data were obtained using the tapping mode, and then, in the second scan, the VPD (employing the SKPFM) on a surface was measured by lifting the tip up to 100 nm and passing once more over the surface in the non-contact mode. The scanned surface area was 100 x 100 μm. The WSxM software was used to process and edit the obtained results [134].

2.4.8 Vickers hardness test

The hardness test has been used exclusively in study 3.3 to test the resistance to delamination in an improvised way, i.e. the detachment resistance of the ALD films from cp-Ti and SS316L substrates [97]. The method is based on measuring the area of the ALD film that has cracked and detached from the substrate when applying different loads of the pyramidal Vickers indenter. The ALD-coated specimens were used and subject to load conditions marked as $HV_{2.0}$, where applied force is around 20 N.

2.4.9 X-ray diffractometry

X-ray diffractometry (XRD) (Empyrean, Malvern PANalytical) was used to estimate the crystallinity of the ALD films deposited only on cp-Ti specimens in study 3.4 using grazing incidence (GI-XRD) mode, with Cu Kα1 radiation (λ = 1.5406 Å) at 45 kV and 40 mA. A hybrid monochromator with a 1/16° slit was used on the incident beam side, and a parallel plate collimator with a 0.27° opening was used on the diffracted beam side. The GI angle (ω) was fixed at 1°, and the X-ray patterns were collected in the 2θ range from 20° to 80° with a step size of 0.02°.

2.4.10 Transmission electron microscopy

Transmission electron microscopy (TEM) (JEM-2010F, Jeol Ltd.), equipped with Gatan PEELS system, Oxford Instruments EDS ISIS 300 system, STEM detector (BD, ADF, HAADF) and Gatan Orius camera, was used for detailed structural investigations of cp-Ti specimens coated with hafnia thin films (study 3.4). For this purpose, the specimens were prepared as lamellas using FEI Helios Nanolab 650, focused ion beam (FIB) technique. Firstly, the specimens were protected with an electron deposited Pt layer of 300 nm and an additional ion deposited Pt layer of 2.5 μm. Then, the preparation of lamellas began with ion milling with Ga^+ ions as an etching beam. Final polishing was performed with Ga^+ ions at 1 kV/100 pA for 1 min on each side, enabling the removal of the amorphous residue and gallium artefacts. The final thickness of lamella was below 50 nm.

2.5 Biological Assays

This part of the research was carried out in collaboration with the Institute for Research & Innovation in Health (i3S) in Porto. All specimens were prepared at the Jožef Stefan Institute (JSI) (Section 2.1) and were sent for testing at i3S.

2.5.1 Biocompatibility

Biocompatibility assays were performed in two ways: incubating the specimens and using their extracts and directly seeding the cells on the specimen surfaces. Specimens were sterilized by immersion in serial dilutions of ethanol (90, 70, and 50 % (v/v)) and rinsing with autoclaved deionized water followed by phosphate-buffered solution (PBS) for 15 min. Human bone marrow-derived mesenchymal stem cells (hMSCs - Lonza) were used to perform both types of assays. Unless mentioned otherwise, all reagents were obtained from Sigma in analytical grade.

2.5.1.1 Assays with extracts

Extracts were obtained by placing each specimen in 7 ml of Dulbecco's modified eagle medium (DMEM – 21885025 Thermo Fisher Scientific) with low glucose supplemented with 1% (v/v) penicillin-streptomycin (15070063 – Thermo Fisher Scientific) and incubating overnight in an orbital incubator at 37 °C and 180 rpm. The following day, specimens were removed, and the extracts supplemented with 10% (v/v) fetal bovine serum (FBS – 10094563 Thermo Fisher Scientific) previously inactivated by heat. A 1% (v/v) solution of Triton X-100 (BP151-500 – Sigma Aldrich) prepared in a fresh culture medium was used as a positive control for cell death.

Cells were seeded at a density of $1.5x10^4$ viable cells/cm^2 (as determined by the trypan blue assay) in 96-well tissue culture plates (353072 - Falcon) with 3 replicates for each sample type, subsequently treated with the extracts and kept at 37 °C in a humidified atmosphere of 5% CO_2. At the end of each culture period (24 h, 48 h and 72 h), the cell viability and morphology were assessed using a resazurin-based assay and immunocytochemistry at the end of experiment (72 h). A schematic representation of the implementation of the assays with extracts is shown in **Fig. 2.3**.

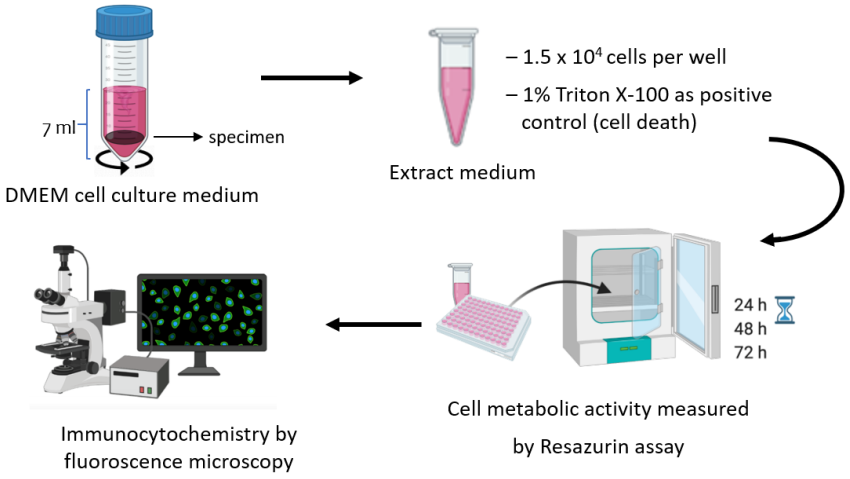

Figure 2.3: Schematic representation of the performance of the assays by using extracts.

2.5.1.2 Test by direct contact

$1.1x10^4$ viable cells/cm^2 (as determined by the trypan blue assay) were directly seeded per specimen, added medium for culturing (DMEM) and maintained at 37 °C in a humidified atmosphere of 5% CO_2. At the end of each culture period (1st and 7th day), the cell viability and morphology were assessed using a resazurin-based assay and immunocytochemistry at the end of the experiment (7th day).

2.5.1.3 Resazurin Assay

To monitor cell metabolic activity and infer about cell viability, a resazurin assay was performed in both cases, from extracts and with direct contact of cells with specimens, as described above. Resazurin is a blue, non-fluorescent molecule that several cell enzymes reduce to a pink, fluorescent product called resorufin. The amount of resorufin produced is directly proportional to the number of living cells. A resazurin solution (0.1 mg / mL in PBS) was added to each well with a cell culture medium to a final concentration of 10% (v/v). After 3 h of incubation at 37 °C, 200 µL of the medium was transferred into a black-walled plate, and fluorescence was measured at excitation and emission wavelengths of 530 and 590 nm, respectively (Synergy Mx microplate reader – Biotek Instruments).

2.5.1.4 Immunocytochemistry

To assess cell morphology, at the end of the experimental period for each case, 72 h and 7 days, respectively, the cell culture medium was removed, and cells were fixed with 4% (w/v) p-formaldehyde (30525-89-4 – TCI) in PBS for 15 min. Cytoskeletal filamentous actin (F-actin) was stained by incubating cells with Alexa Fluor 488 phalloidin (a12379 - Invitrogen), 5 U/mL, for 30 min in the dark. Cells were then washed three times with PBS, and cell nuclei were counterstained with Hoescht 33342 (H3570 - Invitrogen). Samples were imaged with an inverted epifluorescence microscope (Leica DMI6000 FFW).

2.5.2 Antibacterial properties

Antibacterial properties were assessed by incubating the specimens with the bacteria *Staphylococcus aureus* (ATCC 25923). First, all prepared specimens were sterilized twice by immersion in 70 % (v/v) ethanol for 15 min, then rinsed three times with sterile MilliQ water, dried with Ar and stored in a 24-well plate saturated with Ar.

A drop (35 µL) of bacterial inoculum at a concentration of 1×10^7 CFU/mL was placed on the surface of the specimen and covered with a polypropylene film. Specimens were then placed in a 24-well plate inside a humidified box to avoid evaporation and left to incubate at 37 °C for 2 h. After incubation, the polypropylene film was removed, then 1 mL of sterile PBS was added to each sample, i.e. the content was collected (supernatant) and diluted for colony forming units (CFU) counting. Then specimens were rinsed three times with PBS and prepared for SEM analysis to visualize adherent bacteria or processed to detach adherent bacteria by sonication.

To detach adhered bacteria, a protocol described here [135] was followed. Specimens were transferred to 50 ml Falcon tubes containing 1 mL of 0.5 % (v/v) Tween 80 in PBS and then sonicated (BactoSonic®, BANDELIN) at 160 W for 15 min, placed on ice for 5 min and vortexed, and sonicated again for 15 min. Then, serial dilutions were prepared and plated for CFU counting of bacteria directly adhered to the surface of the tested specimens.

2.5.2.1 Scanning electron microscopy

Specimens were prepared according to a procedure described here [136]. After collecting supernatants, specimens were washed three times with PBS, as described above. The adherent bacteria were then fixed with a freshly prepared solution of 1.5% glutaraldehyde in 0.14 M of sodium cacodylate buffer for 30 min at room temperature. After fixation, the specimens were rinsed twice with deionized water and dehydrated using a growing ethanol/water gradient (50%, 60%, 70%, 80%, 90% and 99% (v/v)), maintaining the specimens in each solution for 10 mins. Then, 1 mL of hexamethyldisilazane was added to each specimen, and they were left to dry overnight. The specimens were placed onto SEM pin stubs (TED PELLA, Inc., USA) using carbon tape and sputtered with an Au/Pd thin film (15 mA, 60 s) to improve their conductivity. The surface topography and chemical composition, and bacteria morphology and distribution, were characterized by SEM.

Chapter 3

Results and Discussion

3.1 The Effect of cp-Ti Surface Preparation on the Protective Properties of ALD Al_2O_3 and HfO_2 Films

3.1.1 Surface morphology

The 3D surface profiles of ground and polished specimens were obtained using the profilometry method. These specimens, designated as Ti-500 and Ti-OPS, respectively, are prepared according to the procedures described in Section 2.1.

For ground specimens, the range of S_a was 200 nm, while polished specimens, with very smooth surfaces, had S_a values in the range of 10 nm, i.e. one order of magnitude smaller (**Figs. 3.1 a-f**). The main feature of the thin films grown by ALD is that they follow,

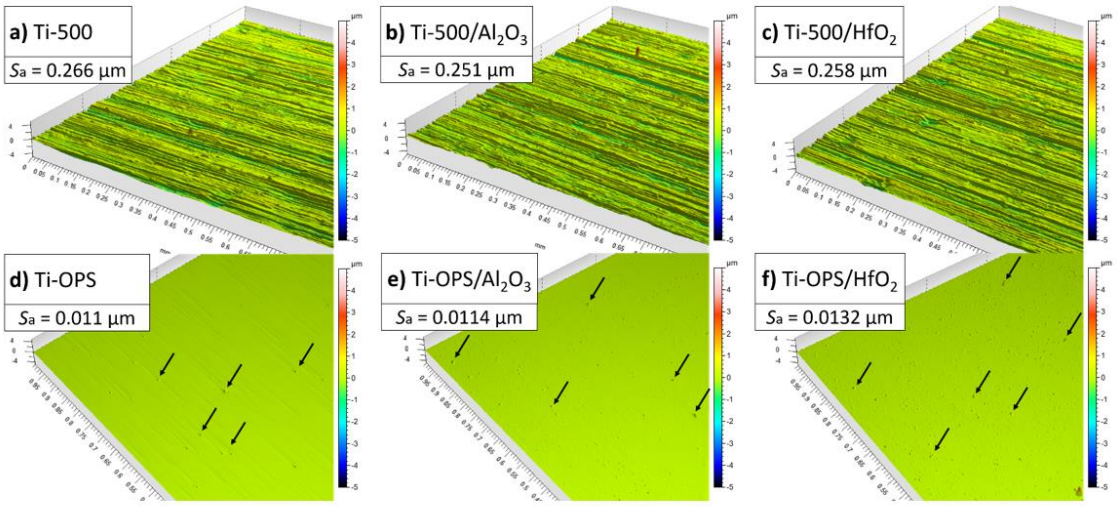

Figure 3.1: 3D surface profiles of differently prepared bare and coated specimens of cp-Ti and their roughness values (S_a) obtained by profilometry, **a)** bare, ground cp-Ti surface; **b)** ground cp-Ti surface coated with alumina; **c)** ground cp-Ti surface coated with hafnia; **d)** bare, polished cp-Ti surface; **e)** polished cp-Ti surface coated with alumina; **f)** polished cp-Ti surface coated with hafnia. Small arrows in polished specimens denote the spots from which the SiO_2 particles were removed.

almost perfectly, the topography of the substrate surface [90], [137]. This property stands out, especially for certain films such as alumina, which tend to form an amorphous structure with a smooth surface [137]. Some other films, such as hafnia, show the possibility of forming a certain amount of polycrystalline structure, which can increase the roughness due to the growth of facets on the crystallites [99], [129]. Here we observed that ground (**Fig. 3.1 a-c**) and polished (**Fig. 3.1 d-f**) surfaces retain their roughness after deposition of the two ALD thin films, alumina and hafnia, since the S_a values, before and after depositions, differed negligibly. Accordingly, hafnia grown at the relatively low temperature of 180 °C probably does not show the very high crystallinity that would cause a significant increase in the roughness. Moreover, after the deposition of both thin films on ground surfaces, the roughness was slightly decreased, confirming a smoothing effect [138], [139]. Some irregularities (tiny bumps noted by arrows in **Fig. 3.1 d-f**) were noticed on polished surfaces. It will be shown below that these features, caused by the removal of SiO_2 particles during specimen preparation, could theoretically trigger agglomerate or crystallite formation, particularly for hafnia.

A comparison of the SEM images of the ground and polished cp-Ti surfaces shows a significant difference in the surface morphology (**Fig. 3.2**). Ground specimens exhibit a rough surface with random longitudinal scratches (**Figs. 3.2 a,b**). In contrast, the polishing procedure revealed the Ti grains (**Figs. 3.2 c,d**). The microstructure is typical of coarse-grained titanium, with relatively large grains of several tens of micrometers. H_2O_2 and NH_4OH added to the OP-S polishing suspension improve the removal rate of the cp-Ti surface, thus producing a reproducible, mirror-like surface appearance [140]–[142]. However, different removal (etching) rates and/or grain orientations may produce a

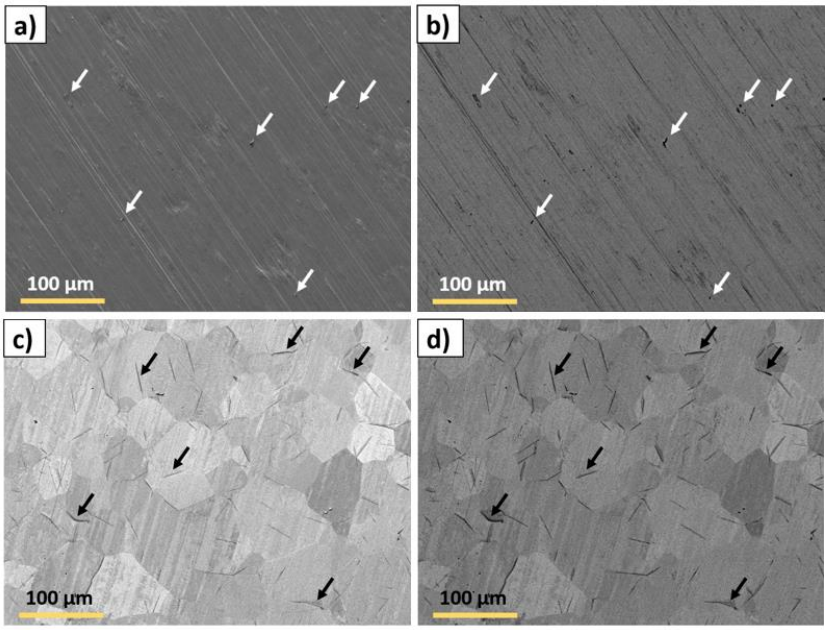

Figure 3.2: SEM images of the ground and polished cp-Ti surfaces from the **a)** secondary electrons and **b)** backscattered electrons showing the morphology and composition of the ground cp-Ti surface, **c)** secondary electrons, and **d)** backscattered electrons, each showing the morphology and composition of the polished cp-Ti surface. White arrows denote SiC particles embedded in the ground cp-Ti surface; black arrows denote oxygen-rich areas on the polished cp-Ti surface. Magnification was 250× and beam acceleration voltage 5 kV.

non-perfectly smooth surface at grain boundaries. The polishing with added H_2O_2 and NH_4OH may exhibit increased hydrophilicity of the surface [143], which helps the uniform growth of ALD films [144].

The interaction between cp-Ti and the mixture of H_2O_2 and NH_4OH during the polishing allows subsequent chemical dissolution and oxidation of the cp-Ti surface. An enlarged SEM image of grains on cp-Ti surface is presented in **Fig. 3.3 a,** and the corresponding EDXS analysis on the surface is given in **Table 3.1.** The surface is covered by a titanium oxide layer with the main constituent titanium and oxygen. Some longitudinal sites are slightly richer in oxygen (spectra 1, 2 and 3). Note that at smaller magnification, these spots are observed as black lines (**Figs. 3.2 c,d**). The formation of oxygen-rich areas can be related to the action of H_2O_2 and NH_4OH reagents during polishing and the formation of Ti peroxide [145], [146] and, even, superoxide [143]. The formation of Ti peroxide over the entire surface of cp-Ti could provide surface protection and improve the biocompatibility of the cp-Ti surface [145], [146]. However, from the aspect of researching the barrier properties of ALD thin films, it is not of great importance since the entire cp-Ti surface is covered with ALD film anyway.

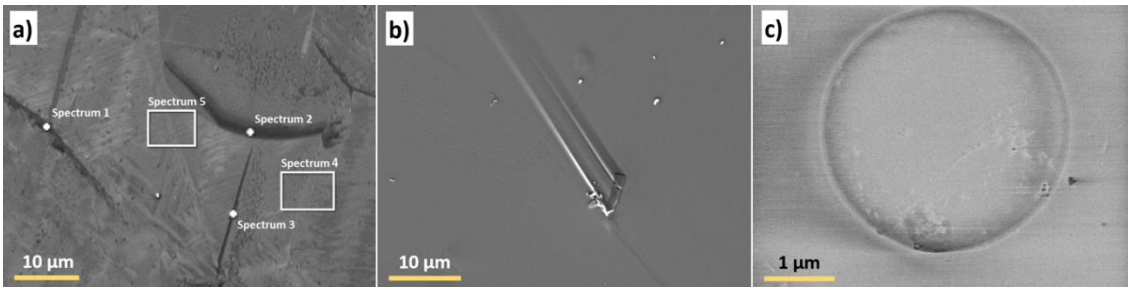

Figure 3.3: SEM images of **a)** polished cp-Ti surface, recorded using the back-scattered electrons, magnification was 2,000×, **b)** the embedded SiC particles in the Ti-OPS surface coated with alumina, recorded using the secondary electrons; magnification was 2,300×, and **d)** the site of the removed SiO_2 particle, recorded using the secondary electrons; magnification was 22,000×. The beam acceleration voltage was 5 kV.

Table 3.1: Results of EDXS analysis on polished cp-Ti surface shown in **Fig. 3.3 a**.

Spectrum	**Ti (at %)**	**O (at %)**
1	92.5	7.5
2	93.3	6.7
3	92.8	7.2
4	94.3	5.7
5	94.4	5.6

At some spots on ground specimens, residues of SiC particles embedded in the surface were observed (white arrows in **Figs. 3.2 a,b**). Several other features are evident in polished specimens (**Figs. 3.2 c,d**). cp-Ti is a soft and ductile metal whose surface is susceptible to deformation by the action of hard particles from grinding and polishing

treatments. These particles can also be embedded in the surface [147]. The polishing processes predominantly remove the embedded SiC particles originating from the emery papers or SiO_2 particles originating from the polishing suspension. Only some isolated particles were detected on the specimen surface (**Fig. 3.3 b**). Several unrelated particles, ascribed to contamination, were also detected on the surface, although very rarely. The much smaller SiO_2 particles could be very tightly embedded in the surface, remaining there after rinsing with distilled water and ultrasonication in ethanol. However, thanks to the polishing procedure and extensive ultrasonic cleaning, SiO_2 particles were removed effectively from the surface, but dents and holes of regular circular shape remained at such spots (**Fig. 3.3 c**). Arrows note these features on 3D surface profiles in **Figs. 3.1 d-f.**

On coated specimens, the dents and holes represent the sites, i.e. defects and edges, where agglomerates and crystallites are formed during the ALD process and could affect the growth of the ALD films. However, these formations can also form spontaneously, i.e. regardless of surface morphology, which has been proven for perfectly smooth surfaces of Si-wafer as a substrate and is shown in Appendix B. SEM analysis showed that agglomerates of nanometer size (denoted by white arrows) were formed over the entire surface (**Fig. 3.4**). For hafnia thin film (**Fig. 3.4 b**), the amount of very small agglomerates was substantial compared with alumina (insets in **Fig. 3.4 a**). Contaminant particles formed due to transport and specimen handling are denoted with black arrows (**Fig. 3.4**). Distinctive features, several micrometers of length, were observed throughout the surface (black circles). They are formed on alumina and hafnia thin films but were more visible on the former due to the fewer ALD agglomerates. These irregular features are likely related to the growth of ALD films on oxygen-rich sites and/or grain boundaries (**Figs. 3.2 c,d**).

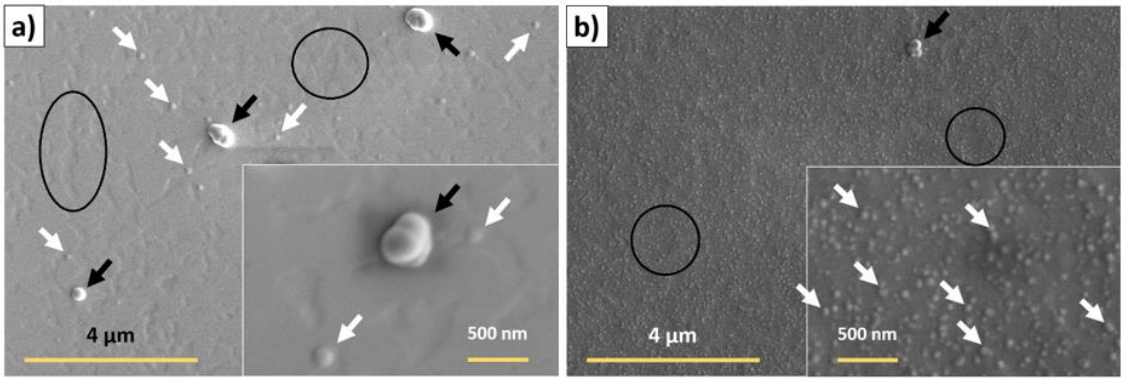

Figure 3.4: SEM images recorded using secondary electrons of **a)** alumina and **b)** hafnia thin films deposited on the Ti-OPS surface. Magnification was 10,000× and 50,000× (insets) and beam acceleration voltage 2 kV. White arrows denote ALD agglomerates or crystallites, black arrows denote larger agglomerates, and black circles denote distinctive irregular features grown on oxygen-rich sites of the substrate.

3.1.2 Chemical composition and thickness

The interfaces between ALD thin films and polished Si substrates can be observed on the compositional depth profiles obtained by the ToF-SIMS technique. Due to the high smoothness of the polished Si-wafers, this border is sharp enough to estimate the thicknesses of ALD thin films. Signals for Al^+ and AlO^+ for alumina (**Fig. 3.5 a**) and Hf^+ and HfO^+ for hafnia thin film (**Fig. 3.5 b**) are shown. Si^+ and SiO^+ were used as the

signals of the substrate. The ToF-SIMS depth profiling is a valuable method for analyzing thin films, but the ratio of different ion intensities does not provide quantitative information on thin films [148]. Thus, due to the significant variation in ionization probabilities between different chemical elements and compounds, ToF-SIMS can only be considered a qualitative method. In the compositional profiles, the difference is noticeable. Al, as a relatively light element, can be very easily ionized from the Al_2O_3 compound, where it gives an abundance of positive ions, while Hf, which is known as a hard metal, shows much poorer ionization, by more than one order of magnitude, from the HfO_2 compound (**Fig. 3.5**).

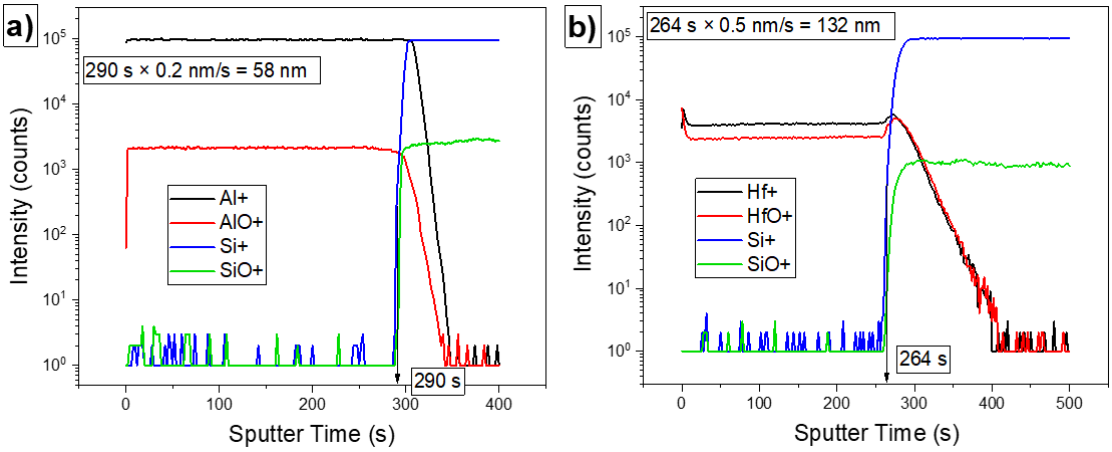

Figure 3.5: Compositional depth profiles with the calculation of the thickness of **a)** the alumina ALD thin film with the characteristic signals of Al^+ and AlO^+ and **b)** the hafnia ALD thin film with the characteristic signals Hf^+ and HfO^+. Characteristic signals of Si substrates are Si^+ and SiO^+ ions.

When considering the thickness of ALD thin films, we cannot rely solely on the GPC and number of cycles because of substrates of different chemistry and roughness. The ALD films can have different growth rates and densities. A thickness of 100 nm was expected according to the recipe developed previously on perfectly polished Si wafer specimens. However, this study has proven that on the polished cp-Ti, the thickness can vary significantly and deviate from the expected one. Also, shortcomings of different methods when determining the thickness were detected. Reliable data on thickness were only obtained by direct measurement using SEM analysis at the cross-section site.

To estimate the thicknesses of ALD thin films, the time at which an intensive increase in Si^+ signal occurred was taken to indicate that the interface has been reached (**Fig. 3.5**). Etching rates were *ca.* 0.2 nm/s for alumina and *ca.* 0.5 nm/s for hafnia thin films because different etching conditions were used. Both were determined by using a thin film of SiO_2 of known thickness as standard. Based on the obtained parameters, the thickness of the ALD thin film can be calculated as a product of the time the interface with the silica substrate is reached and the etching rate (**Fig. 3.5**). Accordingly, the thickness of the ALD alumina would be *ca.* 58 nm and that of the ALD hafnia film *ca.* 132 nm. These results in both cases show a significant deviation from the expected thickness of 100 nm. The reason is the difference in chemical composition and density between the ALD films and the standard used. Therefore, a more suitable standard should be taken for both thin films. A similar problem with ALD thin films was observed in another study, where the glow discharge optical emission spectroscopy technique was used for estimating thickness [97].

Ellipsometry was taken as the second method for thickness evaluation. The thicknesses of the film deposited on Si-wafers were around 100 nm, as it has also been confirmed by FIB-SEM observation (see Appendix B), but this was not the case for cp-Ti substrates. The obtained values were 108 nm (±1 nm) for alumina and 109 nm (±1 nm) for hafnia thin films on Ti-OPS, which is very close to the expected value of 100 nm. The thickness has been only reliably determined at the FIB cross-section of the thin films using direct SEM observation (**Fig. 3.6**). This method measured the thickness of ca. 160 nm for alumina (**Fig. 3.6 a**) and *ca.* 150 nm for hafnia (**Fig. 3.6 b**) thin films. Note that the measured thickness may vary from site to site by a couple of nanometers due to agglomerates on the surface of the ALD films, especially in the case of hafnia. Cross-section SEM is representative of the thickness of the ALD films (**Figs. 3.6**) but does not show clearly the presence of agglomerates. Accordingly, the presented results emphasize that great care must be taken when determining the thickness of ALD thin films. Evaluation based on comparing a particular property of the analyzed and standard materials or a theoretical model can result in an incorrect result.

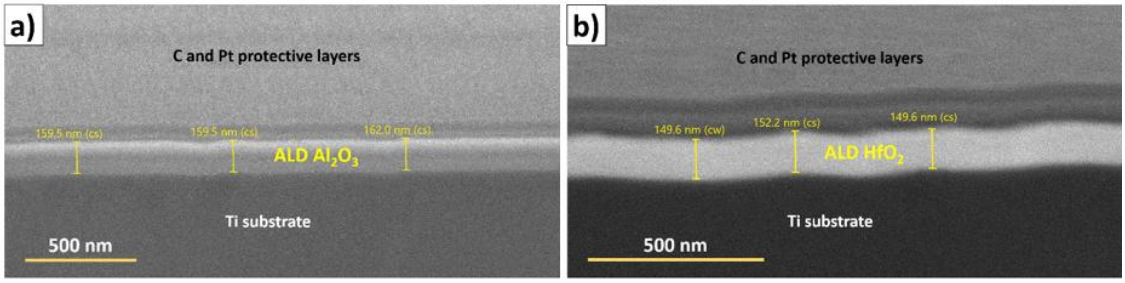

Figure 3.6: SEM image, obtained by secondary electrons, of the ALD thin films on the FIB cross-section sites of **a)** alumina and **b)** hafnia deposited on the polished cp-Ti surface. Magnification was a) 50,000× and b) 80,000× and beam acceleration voltage 2 kV.

The ALD films deposited on rough Ti specimens were not subjected to the FIB/SEM. However, it can be estimated from the thicknesses obtained by ellipsometry. They were 115 nm (± 1 nm) for alumina and 116 nm (± 1 nm) for hafnia, but since they are unreliable, it is expected that both thickness values are slightly higher compared to smooth surfaces. As proved here, the ALD method tends to form thicker deposits on rough surfaces [99]. Therefore, in the absence of an appropriate theoretical model, ellipsometry as a fast and non-destructive method may only be used as an assistant method for estimating the thicknesses of these films.

The composition of the ALD films was determined using EDXS at the top surface (**Fig. 3.7**) and the FIB cross-section (**Figs. 3.8**). The expected chemical composition of both thin films was confirmed (**Fig. 3.7**). Besides the pronounced peaks for O, and Al and Hf, respectively, the strong peaks for C are also visible originating from the carbon thin films deposited to prevent the charging effect of the specimens. Although this technique should thus be considered semi-quantitative, it can be stated that the experimental Al:O ratio is 2:3, in accordance with the stoichiometric ratio in alumina, and Hf:O is 1:2, as is expected for the stoichiometric ratio in hafnia (**Fig. 3.7**).

The FIB/EDXS analysis at the cross-section provided crucial information concerning the structure of ALD films. Both ALD films were compact and uniform, with no deformation sites or cracks (**Figs. 3.8**). EDXS analyses confirmed this visual information since only Al, Hf and O atoms were detected. Signals of particular elements overlap, especially for the hafnia thin film, due to contamination of particular layers with elements

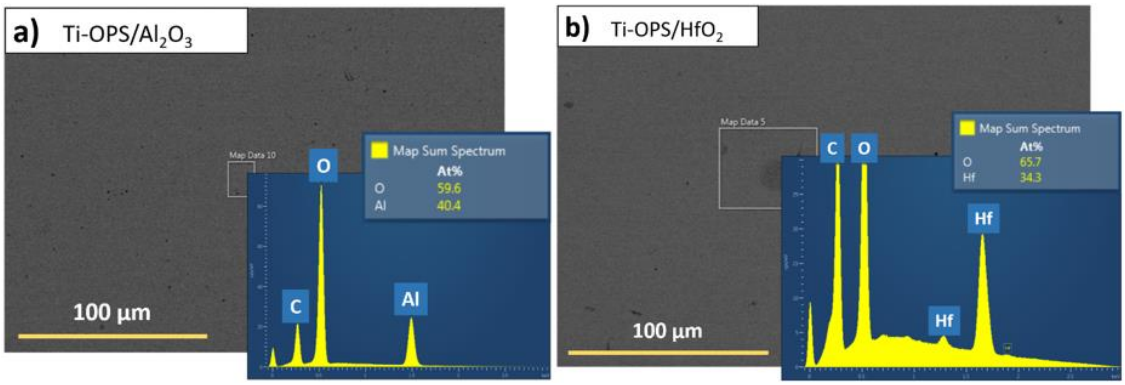

Figure 3.7: SEM images obtained from backscattered electrons and EDXS spectra recorded on the surface of **a)** alumina and of **b)** hafnia ALD thin film on the polished cp-Ti surface. White rectangles at the SEM images are spots where EDXS analyses were made.

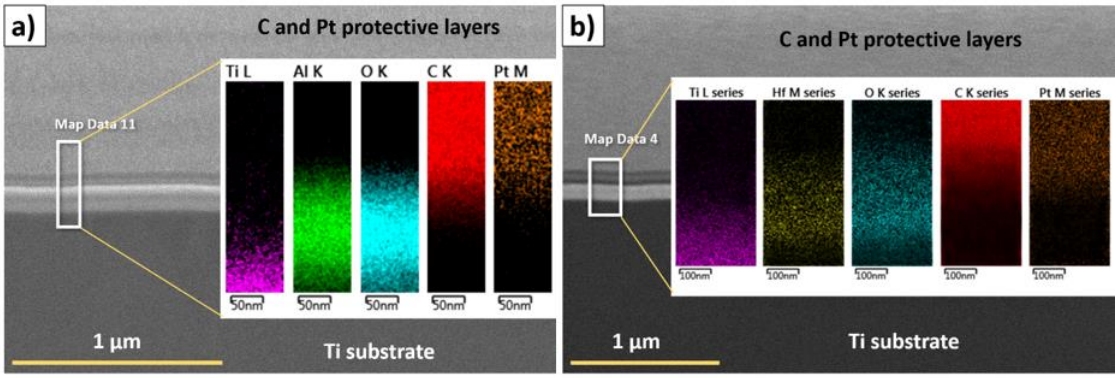

Figure 3.8: SEM images of the cross-section site made by FIB of **a)** alumina and **b)** hafnia with EDXS mapping recorded at the white rectangle. SEM images were recorded using the secondary electrons under magnification of 40,000×; beam acceleration voltage was 2 kV.

from adjacent layers during the etching process by FIB. ALD films follow the substrate surface, so there is no indication of delamination.

EDXS revealed specific characteristics of the polished cp-Ti surface related to the effect of the combined action of H_2O_2 and NH_4OH (**Figs. 3.2 c,d**). The SEM investigation of the polished cp-Ti surface covered with alumina ALD thin film revealed larger and smaller dark flecks or spots (**Fig. 3.9**). According to EDXS mapping analysis, these spots were enriched in Ti and O atoms, indicating the enhanced formation of passive TiO_2 film. As the second explanation, the possibility of thermally induced spreading of Ti peroxide during heating in the ALD chamber must be considered. Namely, since random sites enriched in oxygen on the uncoated polished surface (**Fig. 3.3 a, Table 3.1**) are ascribed to the formation of Ti peroxide, its growth and spreading could occur at increased temperatures before the ALD deposition. Although the formation of the Ti peroxide and its thermal treatment correlates with the improved protective properties of the cp-Ti surface [145], its role under ALD thin film is negligible. Even so, the formation of oxide/peroxide below the ALD film does not affect the uniformity and compactness of the ALD films, as confirmed by the SEM investigation (**Fig. 3.6**).

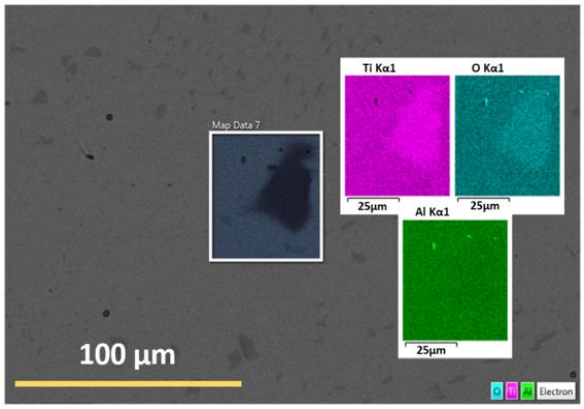

Figure 3.9: SEM images obtained from backscattered electrons and EDXS mapping analysis recorded at the surface of alumina ALD thin film on the polished cp-Ti surface. Mapping was recorded within the white rectangles.

3.1.3 Electrochemical properties

3.1.3.1 Potentiodynamic polarization

PDP curves recorded for ground (Ti-500) and polished (Ti-OPS) bare cp-Ti specimens following immersion of 1 hour and 40 days at the OCP in Hanks' solution are presented in **Fig. 3.10**. After 1 hour of immersion, the current density increased exponentially from E_{corr} to *ca.* 0 V and −0.2 V for Ti-500 and Ti-OPS, respectively, when a broad passive plateau was established. At more positive potentials, the growth of highly insulating passive film prevailed and continued up to 2.5 V and 2.8 V, when the current density increased due to oxygen evolution reaction [149], [150]. XRD and XPS studies showed that the oxide layer on Ti-20Nb-10Zr-5Ta alloy and pure Ti [151] consists of a disordered mixture of amorphous Ti oxide and suboxide, i.e. TiO_2 and Ti_2O_3, when formed at potentials up to 1 V. At more positive potentials, the layer is completely transformed into passive TiO_2. It seems that the same process occurs here, i.e. at 0 V for Ti-500 and –0.2 V for Ti-OPS, the oxide film was transformed into amorphous TiO_2, which provided a broad, passive plateau of the current density. The formation of the crystalline TiO_2 passive film was reported to occur at higher potentials of *ca.* 5 V [149], [152] and associated with the passive film's breakdown.

After 40 days of immersion of Ti-500 and Ti-OPS specimens, the E_{corr} values were shifted to more positive values, i.e. by 0.6 V and 0.25 V, respectively (**Fig. 3.10**). This indicates that, after prolonged immersion, the oxide film contributed to the surface passivation. The strong shift of the Ti-OPS curve to smaller current density and more positive potentials may be related to the presence of the Ti-peroxide gel, as well as to the formation and continued growth of the mixture of oxides and suboxides in the passive film during 40 days. The increase in the current density was halted entirely at potentials below 1 V. At more positive potentials, the long-immersed Ti-OPS specimen showed the same characteristics as those after 1 h of immersion, i.e. the passive film consisted of TiO_2. In the case of Ti-500, the j_{corr} increased slightly at prolonged immersion, an observation that will be interesting to compare with EIS results (*vide infra*). The shape of the PDP curves was similar as at the beginning of immersion. So, on the Ti-500 specimen, which was initially not covered by the modified passive film, i.e. Ti-peroxide gel, as with Ti-OPS, a disordered passive film was formed during 40 days. Its properties are affected by stresses

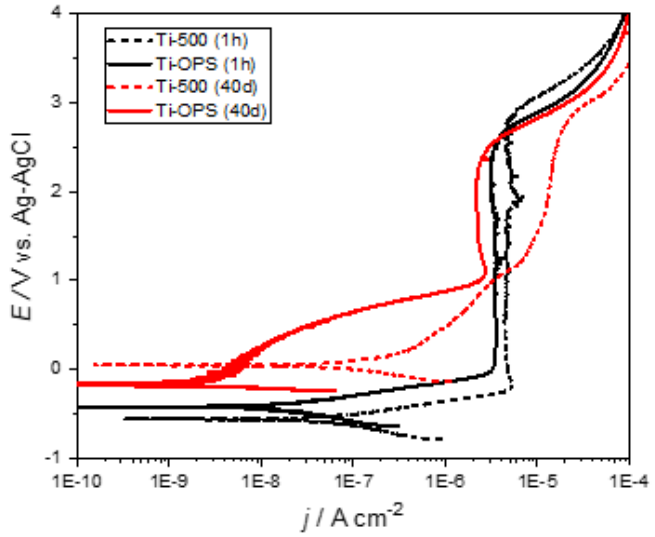

Figure 3.10: PDP curves of bare ground and polished, Ti-500 and Ti-OPS, specimens recorded in Hanks' solution after 1 hour and after 40 days of immersion at the open circuit potential. $\mathrm{d}E/\mathrm{d}t = 1$ mV/s.

present in the film on the rough surface [153], making it an inadequate insulation barrier for establishing a constant current density. In contrast, Ti-OPS exhibits better corrosion resistance under simulated conditions of the human body after prolonged immersion.

ALD-coated cp-Ti specimens significantly reduced j_{corr} values after 1 hour at the OCP (**Fig. 3.11**). Compared to uncoated specimens, alumina-coated cp-Ti specimens showed much smaller j_{corr} by *ca.* three orders of magnitude. It is worth noting that alumina thin films did not significantly alter the shape of the PDP curves of bare cp-Ti specimens, nor do the E_{corr} values, suggesting that the alumina does not show specific electrochemical activity. Therefore, the ALD technique produced insulative and electrochemically inert alumina thin film [99], [137].

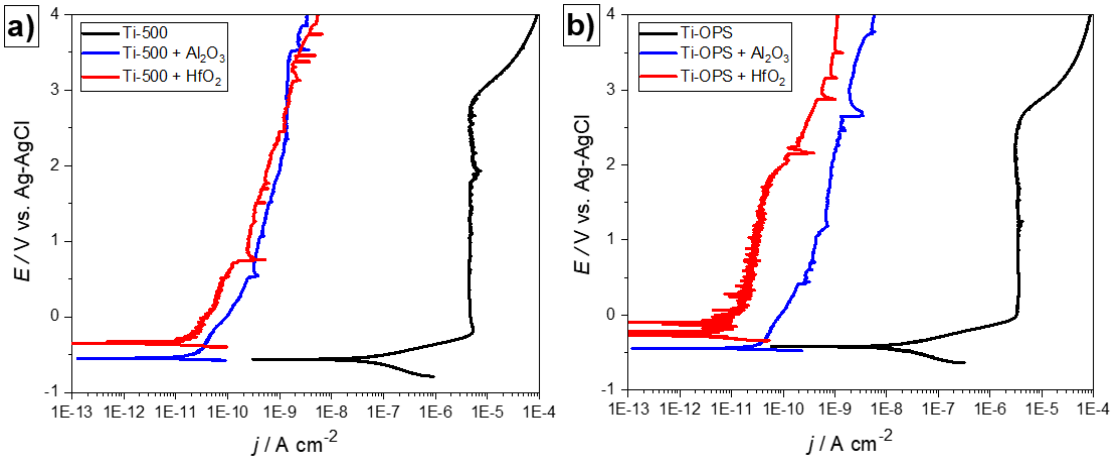

Figure 3.11: PDP curves for bare and ALD-coated cp-Ti specimens recorded in Hanks' solution after 1 h of immersion at the OCP: **a)** ground, Ti-500, specimens and **b)** polished, Ti-OPS, specimens. $\mathrm{d}E/\mathrm{d}t = 1$ mV/s.

Unlike alumina thin films, hafnia showed a positive shift in E_{corr} after deposition on Ti-500 and Ti-OPS specimens, of 0.2 V and 0.15 V, respectively (**Fig. 3.11**). As a high-κ gate dielectric material, hafnia provides additional electrical insulation of the cp-Ti surface and, thus, excellent barrier properties.

All electrochemical parameters (corrosion potential, E_{corr}, corrosion current density, j_{corr}, and calculated polarization resistance, R_p) for bare and ALD-coated specimens are shown in **Table 3.2**. These values were determined to evaluate the electrochemical porosity of ALD films on differently prepared cp-Ti surfaces. The polarization resistances were calculated using the Stern-Geary equation (**Eq. 3.1**):

$$R_p = \frac{B}{j_{corr}} = \frac{|b_a| \cdot |b_c|}{2.3 \cdot (|b_a| + |b_c|) \cdot j_{corr}} \tag{3.1}$$

where B is the Stern-Geary constant, and b_a and b_c are the slopes of the anodic and cathodic branches. For uncoated specimens, j_{corr} was determined as the intersection of tangents to cathodic and anodic branches. For coated specimens, the j_{corr} was determined as the intersection of the tangent to the anodic branch and the E_{corr} line.

There are several methods for calculating the porosity of thin films (P) [154], but in electrochemistry, the equation introduced by Tato and Landolt (**Eq. 3.2)** is mainly used [155]. This equation corresponds to the ratio of the R_p of the bare and coated specimens.

$$P = \frac{R_p}{R_{pALD}} \cdot 100 \tag{3.2}$$

where R_{pALD} is polarization resistance of ALD-coated specimens.

Later, this equation was complemented to **Eq. 3.3** [156], and used in many recent papers to describe the porosity of PVD and CVD films to be used as protection against corrosion [99], [154], [157], [158]. The total porosity of the coating (P) determined using **Eq. 3.3.** takes into account additional electrochemical parameters:

$$P = \frac{R_p}{R_{pALD}} \cdot 10^{-\left(\frac{\Delta E_{corr}}{b_a}\right)} \cdot 100 \tag{3.3}$$

where ΔE_{corr} is the difference in the corrosion potentials between the bare and coated cp-Ti specimens, ΔE is the difference between E_{corr} and $E_{corr\ ALD}$, and b_a refers to the anodic Tafel slope of the bare cp-Ti substrate. Here, P-value was calculated using both equations.

According to the calculated porosity, hafnia generally shows lower porosity than alumina thin films regardless of the equation used (**Table 3.2**). This difference in porosity between hafnia and alumina is particularly highlighted in the Ti-OPS specimen. Deposited hafnia reduced j_{corr} by more than three orders of magnitude for Ti-500 and even more for the Ti-OPS specimen (**Fig. 3.11**). The R_p increased accordingly, reaching values in the range of $G\Omega \cdot cm^2$. Since the values of R_p and ΔE (ΔE=$|E_{corr}$ - $E_{corrALD}|$) are the basis for calculating porosity, the changes of these parameters are reflected in the final values. Moreover, porosity is calculated in relation to the parameters of uncoated specimens, so it should be taken into account that polished specimens generally have larger R_p values. The ΔE for hafnia-coated specimens is broader; consequently, the porosity differs considerably depending on whether **Eq. 3.2** or **3.3** have been taken for the calculation. All these factors result in different trends in porosity for alumina- and hafnia-coated specimens. For alumina, the porosity is higher for polished specimens regardless of the equation used. This higher porosity may be related to the fact that both alumina-coated specimens exhibit similar R_p, so the relative increase compared to the uncoated substrate is smaller for the

Table 3.2: Corrosion parameters and porosity of bare cp-Ti specimens and ALD-coated specimens deduced from PDP curves recorded after 1 h immersion at the open circuit potential.

	E_{corr} / V vs. Ag-AgCl	$\lvert\Delta E_{corr}\rvert$ / V vs. Ag-AgCl	j_{corr} / A · cm^{-2}	R_p / Ω · cm^2	P / % (**Eq. 3.2**)	P / % (**Eq. 3.3**)
Ti-500	-0.561	--	4.7×10^{-8}	8.0×10^5	--	--
Ti-OPS	-0.421	--	1.4×10^{-8}	2.6×10^6	--	--
Ti-500 alumina	-0.549	0.012	2.3×10^{-11}	3.3×10^8	0.24	0.20
Ti-OPS alumina	-0.445	0.024	3.5×10^{-11}	2.2×10^8	1.18	0.80
Ti-500 hafnia	-0.352	0.209	2.0×10^{-11}	6.3×10^8	0.13	0.05
Ti-OPS hafnia	-0.273	0.148	1.1×10^{-11}	1.8×10^9	0.14	0.01

polished specimen. Also, note that alumina grows as an amorphous film and is difficult to crystallize, regardless of the surface irregularities, i.e. on both surfaces, it retains the same protective properties [137]. Hafnia tends to be denser (or less porous) on the polished cp-Ti surface if the porosity is calculated considering the ΔE (**Eq. 3.3**). In contrast, no difference in calculated porosity concerning the surface roughness was observed if ΔE was excluded (**Eq. 3.2**). Note that the absolute R_p value for hafnia deposited on Ti-OPS is higher than on Ti-500 specimen (opposite to results for alumina), which indicates good protection properties.

3.1.3.2 Electrochemical impedance spectroscopy

PDP tests showed that the ALD films on the ground and polished cp-Ti specimens have excellent barrier properties and low porosity. The following step was to perform long term EIS measurements to monitor their barrier properties for 40 days. The uncoated cp-Ti specimens significantly differed in impedance and phase angle values during 40 days (**Fig. 3.12**). For Ti-500, the phase angle slightly decreased in the mean frequency range, reflecting a decrease in the protective properties of the passive film with immersion time (**Fig. 3.12 a**). In contrast, the Ti-OPS specimen's impedance and phase angle values continuously increased during 40 days (**Fig. 3.12 b**). Thus, Ti-OCP exhibited better protective properties at the beginning of the test than Ti-500 and showed a continuous improvement. This is predominantly due to the progressive growth of the oxide layer [159], [160], which seems to be more efficient on the polished surface. It should be noted that there is a high possibility of the formation of insulative phosphate precipitates from the Hanks' solution on the surface [161], [162]. Therefore, the chemical-mechanical treatment of the cp-Ti surface can improve the passivation process significantly in Hanks' solution and/or increase the susceptibility to precipitation of phosphate species. Mechanical treatment alone, i.e. grinding, did not significantly improve the long-term passivation process. The EIS results (**Fig. 3.12**) can be correlated to PDP curves after 40 days of immersion (**Fig. 3.10**); for Ti-500, E_{corr} was shifted slightly more positive, but j_{corr} was even slightly larger, and a plateau of current density was not established at potentials above 1

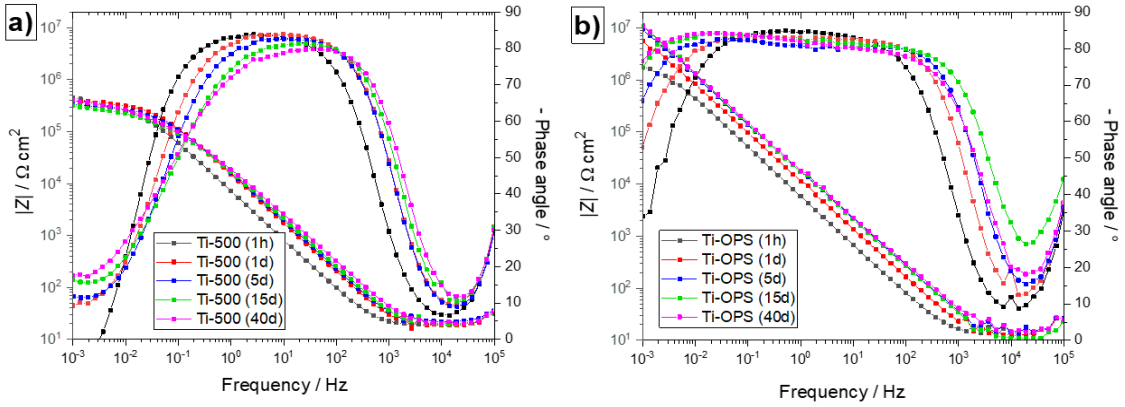

Figure 3.12: Bode plots of bare cp-Ti specimens recorded over 40 days of immersion in Hanks' solution at 37 °C for **a)** ground cp-Ti and for **b)** polished cp-Ti specimen.

V. This means that the long-term protective properties of the passive film on Ti-500 were poorer than that of Ti-OPS, thus confirming EIS results.

EIS spectra of ALD-coated alumina (**Fig. 3.13**), and hafnia (**Fig. 3.14**) indicate significantly higher impedance values than bare specimens. The impedances at the lowest frequency of 0.001 Hz ($|Z|_{0.001\ \mathrm{Hz}}$) were taken as values when evaluating these films' protective properties (**Fig. 3.15**). $|Z|_{0.001\ \mathrm{Hz}}$ of alumina-coated Ti-500 was negligibly lower after 1 hour of immersion than that of Ti-OPS. However, after immersion of 40 days, this difference was more noticeable and was 0.2 order of magnitude favoring the Ti-OPS (**Fig. 3.15**). For alumina-coated Ti-500, the$|Z|_{0.001\ \mathrm{Hz}}$ decreased to the 10th day of immersion and remained constant at longer immersion times. The phase angle dropped after 15 days (**Fig. 3.13 a**), indicating the weakening of the alumina film. In contrast, alumina-coated Ti-OPS show stable impedance and phase angle values over 40 days (**Fig. 3.13 b**). The alumina ALD thin films, therefore, retain their barrier properties better on the polished cp-Ti surface.

For hafnia-coated specimens, the difference between Ti-500 and Ti-OPS specimens was much more pronounced than alumina (**Fig. 3.14**). The $|Z|_{0.001\ \mathrm{Hz}}$ after 1 h was larger by more than one order of magnitude favoring the hafnia-coated Ti-OPS, but after immersion

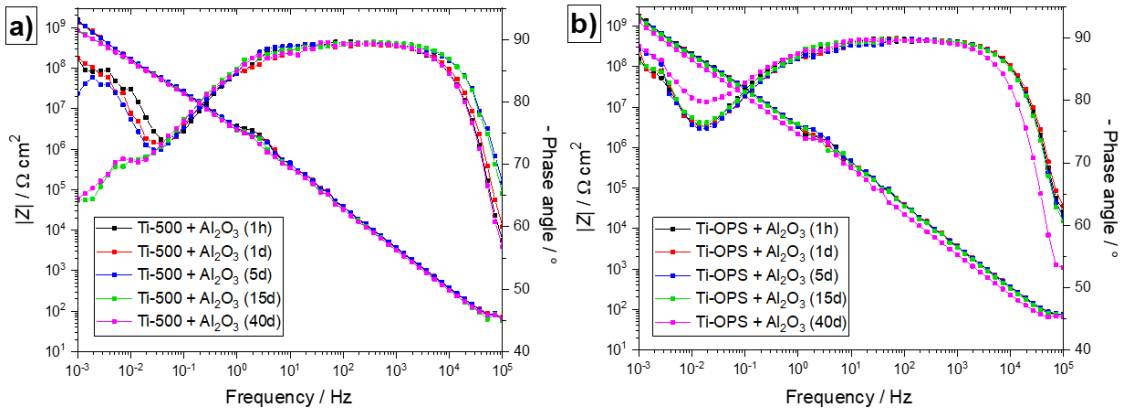

Figure 3.13: Bode plots of alumina-coated cp-Ti specimens recorded during 40 days of immersion in Hanks' solution at 37 °C for **a)** a ground cp-Ti and **b)** a polished cp-Ti specimen.

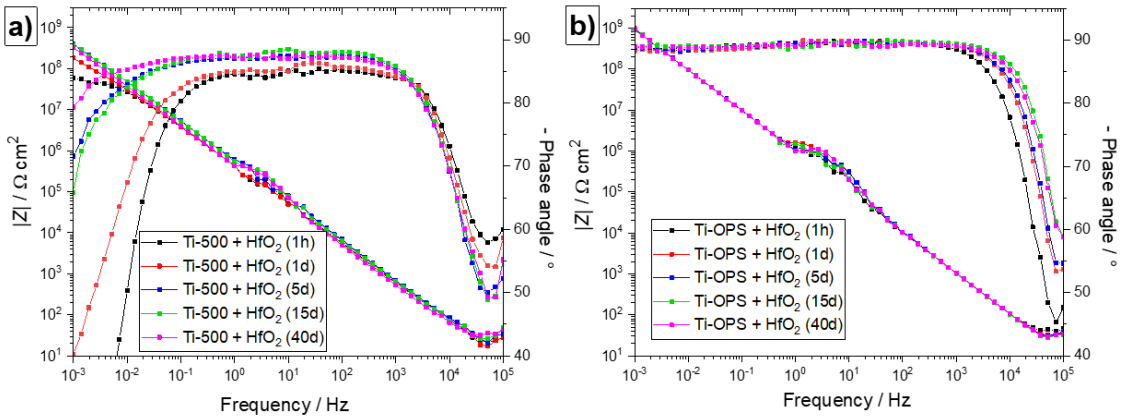

Figure 3.14: Bode plots of hafnia-coated cp-Ti specimens recorded during 40 days of immersion in Hanks' solution at 37 °C for **a)** a ground cp-Ti and **b)** a polished cp-Ti specimen.

for 40 days, this difference was reduced (**Fig 3.15**). Over 40 days, the impedance and phase angle of the hafnia on Ti-500 progressive increased (**Fig. 3.14 a**). The EIS response looks similar to that of the progressive passivation of bare Ti-OPS (**Fig. 3.12 b**). It seems that the changes in Bode plots reflect the passivation of the cp-Ti surface through the pores of the ALD film. The calculated porosity of the hafnia thin film is very low, i.e. 0.05 % (**Table 3.2**), but it still appears to allow the additional passivation reflected in the increase in phase angle during immersion (**Fig. 3.14 a**). In contrast, the hafnia on the Ti-OPS specimen showed better stability (**Fig. 3.14 b**). The almost constant and very high impedance and the phase angle over 40 days confirm its smaller porosity of only 0.01 % (**Fig. 3.14 b, Table 3.2**).

Briefly, both alumina and hafnia thin films on cp-Ti specimens exhibited high and stable $|Z|_{0.001\ \mathrm{Hz}}$ values, especially when deposited on polished surfaces, during 40 days of immersion in Hanks' solution (**Fig. 3.15**). Alumina thin film showed relatively good stability over immersion time but with a falling trend when deposited on Ti-500. Hafnia

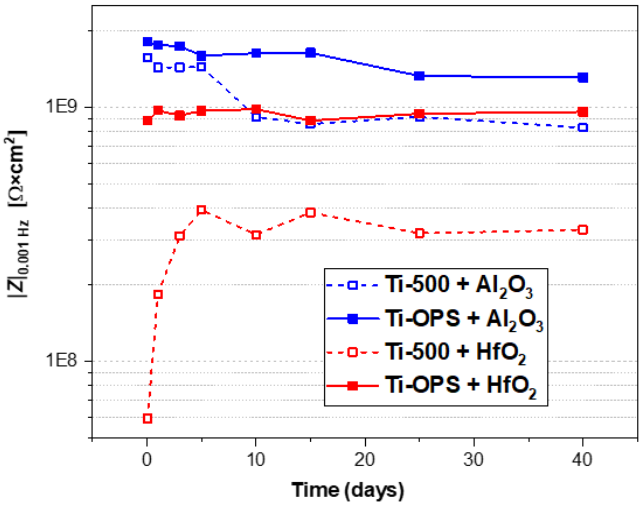

Figure 3.15: Values of $|Z|_{0.001\ \mathrm{Hz}}$ for ground and polished alumina- and hafnia-coated cp-Ti specimens as a function of immersion time in Hanks' solution at 37 °C.

thin film showed excellent stability with continuously high $|Z|_{0.001\ \mathrm{Hz}}$ values only on the Ti-OPS. Alumina and hafnia deposited on Ti-OPS showed larger $|Z|_{0.001\ \mathrm{Hz}}$, which retained constant values over time. The superior behavior of hafnia is also indicated by the high and constant values of phase angles very close to -90° during the whole immersion period.

3.1.4 Summary

Smooth and mirror-like polished surface of cp-Ti can be efficiently obtained only by using chemical reagents, H_2O_2 and NH_4OH. Both type of surfaces, ground and polished, allow uniform deposition and complete coverage of both type of ALD thin films, alumina and hafnia. This is evident from PDP tests, as in the case of both types of surfaces and for both thin films, a vastly reduced corrosion current density is observed. However, alumina and hafnia thin films differ morphologically because hafnia tends to form a lot of tiny agglomerates, while this is much less pronounced for alumina.

Both thin films show significant protective and insulating properties as already mentioned and evident from PDP measurements. However, it has been observed that while alumina provides equal protection on both types of surfaces, the protective properties of hafnia are affected by the surface roughness. Namely, hafnia on a polished surface allows a significantly greater reduction in the corrosion current density than on the ground surface.

However, EIS measurements have provided much more relevant information on protective properties over time in simulated human body conditions. Both thin films, alumina and hafnia, showed a significant increase in impedance magnitude and phase angle values. As it was found by PDP tests, EIS confirmed that alumina and hafnia thin films have different dependence of protective properties on surface roughness. Alumina showed an evident decline in protective properties only after 15 days of immersion under test conditions, while hafnia showed significantly weaker protection immediately after 1h of immersion. Both thin films showed excellent stability on polished surfaces during 40 days of immersion. However, hafnia shows exceptional insulating properties, better than alumina, continuously throughout the 40 days.

3.2 The Effect of Thickness of Al_2O_3 ALD Films Deposited on cp-Ti and SS316L on Their Protective Properties

3.2.1 Surface morphology

SEM micrographs of polished cp-Ti and SS316L surfaces are shown in **Fig. 3.16**. The polished cp-Ti surface was the same as in Section 3.1 (**Fig. 3.2 c,d**) with the coarse-grained cp-Ti microstructure with differently oriented crystal grains of 20 to 100 µm in size are observed **(Fig. 3.16 a**). The SS316L exhibits an austenitic microstructure with equiaxed grains of the same size, 20 to 100 µm (**Fig. 3.16 b**). Chemical etchants, H_2O_2 and NH_4OH, do not have the same etching effect on SS316L as on cp-Ti, though H_2O_2 is recommended for use in the etching mixture for chemical-mechanical polishing for both materials. Despite that, a mirror-like surface was achieved without visual defects and with the same roughness as cp-Ti, i.e. order of 10 nm (Section 3.1).

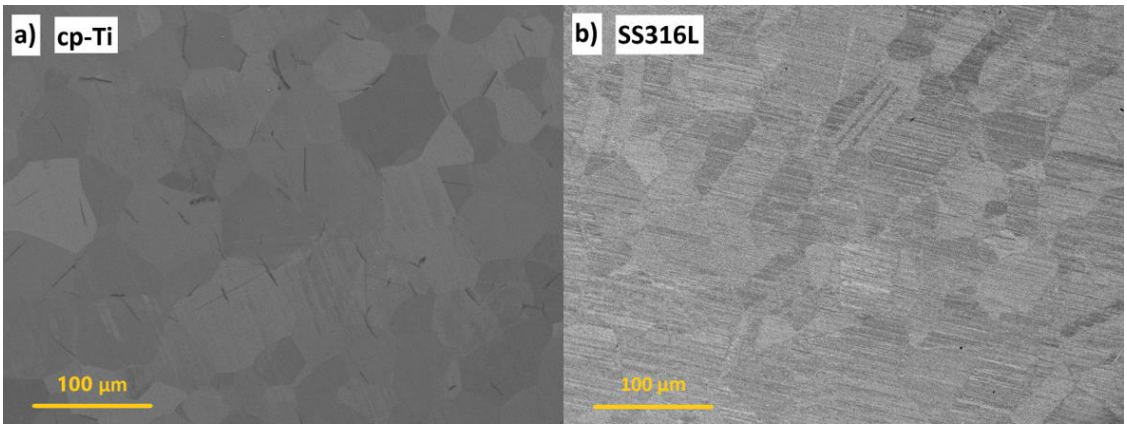

Figure 3.16: SEM images of the **a)** polished cp-Ti surface and **b)** polished SS316L surface, showing their microstructure and grain outlines.

SEM micrographs of specimens with ALD steps, prepared using adhesive tape as described in Section 2.2, are shown in **Fig. 3.17**. Due to the very small thicknesses and the charging effect in SEM, it was difficult to obtain clear morphological images and cross-sections of ALD films at the fracture site. Both thin films, 20AL and 60AL, showed a uniform structure with distributed black spots (slightly harder to see with SS316L) on both substrates. These are surface features of ALD alumina thin films, possibly related to the process of thin film growth. However, these features do not affect the protective properties of the films (*vide infra*), so they are probably not related to porosity.

Regarding morphology along the entire step, more compact and uniform alumina films were obtained for Ti-60AL and SS-60AL (**Figs. 3.17 a,c**) compared to Ti-20AL and SS-20AL thin films (**Figs. 3.17 b,d**). The thicknesses of these films were also evaluated

Table 3.3: Thicknesses and RMSE values of ALD thin films deposited on cp-Ti, measured by ellipsometry.

Expected thickness / nm	Thickness / nm	RMSE
20 nm Al_2O_3	20.1 nm ± 1 nm	0.454
60 nm Al_2O_3	64.2 nm ± 1 nm	0.561

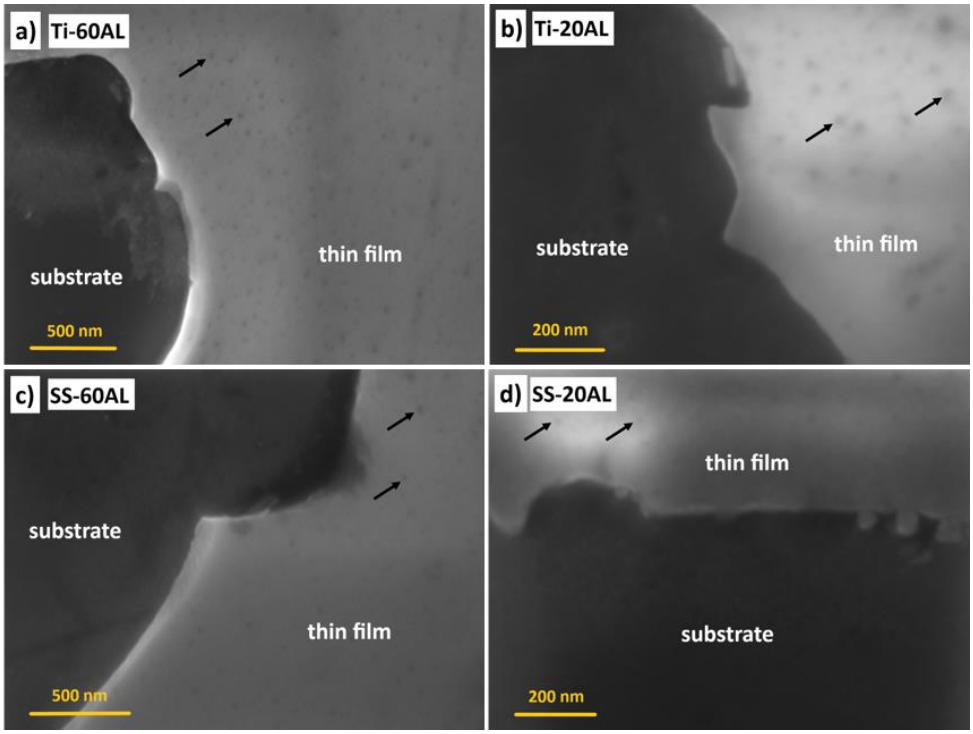

Figure 3.17: SEM images of the step site between ALD film and substrates for the **a)** 60 nm of alumina on cp-Ti, **b)** 20 nm of alumina on cp-Ti, **c)** 60 nm of alumina on SS316L, and d) 20 nm of alumina on SS316L. Arrows denote black spots..

by using ellipsometry (only cp-Ti specimens). The values obtained are following expected values and are presented in **Table 3.3**. However, if we consider the increased RMSE values and the underestimated values of the ALD film thickness shown in Section 3.1, we can expect the thicknesses for both films to be about a few nm higher.

3.2.2 Short-term electrochemical measurements

The comparison of cyclic PDP curves of bare and ALD-coated cp-Ti after 1 hour of immersion at the OCP in simulated physiological Hanks' solution at 37 °C is presented in **Fig. 3.18**. The curve for bare cp-Ti reflects the formation of a completely insulating passive titania film (Section 3.1).

Corrosion parameters, E_{corr} and j_{corr}, are almost the same for alumina thin films, Ti-20AL and Ti-60AL (**Fig. 3.18**). In the case of Ti-60AL, E_{corr} is shifted more positively by *ca.* 0.2 V, compared to cp-Ti, while for Ti-20AL, the shift is *ca.* 0.1 V. Further, for alumina thin films, the j_{corr} value is reduced by about two orders of magnitude compared to cp-Ti indicating that j_{corr} is not significantly dependent on the film thickness. However, the j_{pass} parameter is related to the thickness of the alumina thin films: it was somewhat greater for Ti-20AL than for thicker Ti-60AL film. Therefore, with increasing potential, the effect of ALD film thickness on the protective properties of cp-Ti was observed. In the reverse cycle, the current density decreased for both alumina thin films and for the bare cp-Ti. Long-term EIS measurements, however, will reveal more differences between these thin films (*vide infra*).

The cyclic PDP curves of SS316L showed a different dependence current vs potential response (**Fig. 3.19**) than cp-Ti due to its susceptibility to pitting corrosion [31]. Similar to cp-Ti, bare SS316L showed passivation in the anodic region. Following the E_{corr}, the

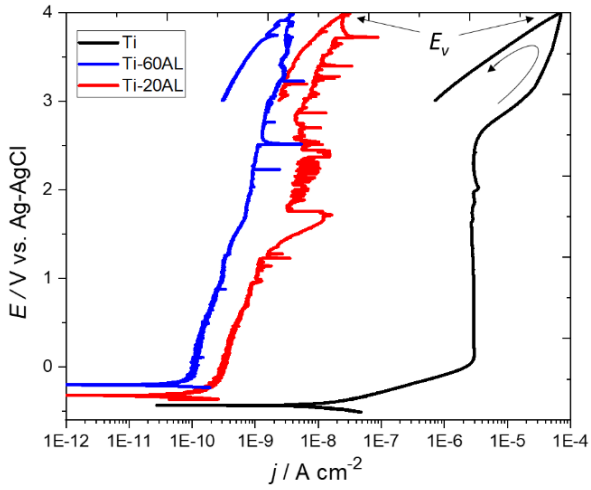

Figure 3.18: Cyclic PDP curves recorded in Hanks' solution at 37 °C for bare cp-Ti, cp-Ti coated with 20 nm and 60 nm of alumina thin films. dE/dt = 1 mV/s.

current density increased initially, and at *ca.* 0.5 V it reached the plateau with the j_{pass} value, i.e. when an insulating passive film is formed. At low potentials, the film is rich in Cr and Mo, while at higher potentials, it becomes rich in Fe as well [163]. The passive plateau is extended up to the breakdown potential (E_b at 1 V). The passive layer breaks down at more positive potentials, and the current density increases abruptly by about one order of magnitude due to localized corrosion. In contrast to cp-Ti, there was no repassivation in the reverse cycle. This may be associated with the lack of Cr on the surface, which would be required for repassivation and cease of pit growth. Since Cr was already depleted for the formation of the passive film, the initiation and pit growth have been continued.

As for cp-Ti, ALD-coated SS316L specimens show reduced j_{corr} by about two orders of magnitude compared to bare SS316L. The j_{pass} values were reduced (conditionally speaking) even more (**Fig. 3.19**). The j_{pass} was established within the first 100 mV above E_{corr} and

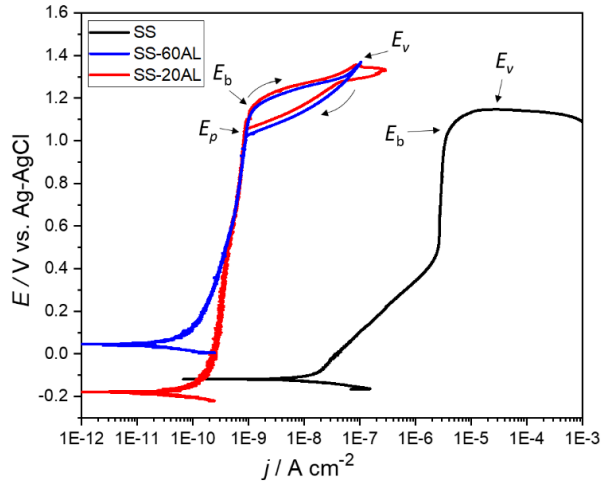

Figure 3.19: Cyclic PDP curves recorded in Hanks' solution at 37 °C for bare SS316L, SS316L coated with 20 nm and 60 nm of alumina thin films. dE/dt = 1 mV/s.

was similar for both thin films. The E_{corr} shifted positively by about 0.15 V for SS-60AL, while for SS-20AL, it shifted slightly negative compared to bare SS316L.

Both alumina thin films break down at about 1.2 V, slightly more positive than the passive film on bare SS316L. At higher potentials, the current density increased rapidly. After scan reversal, the loop was formed (**Fig. 3.19**). The intersection point of the reverse and forward curves is at 1 V. This value is called the pitting protection potential (E_p). Theoretically, below this potential, there is no risk of pitting corrosion. The loop size indicates the level of localized corrosion, which is, in this case, relatively low, i.e. E_b and E_p are not far apart. These results show that the ALD alumina films, whether thinner or thicker, can indirectly prevent the propagation of localized corrosion on the SS316L substrate. This is possible due to the protected surface of the SS316L substrate with the thin film, which when in contact with the electrolyte through the pores of the thin film has the ability to repassivate. On the other hand, the uncoated SS316L is exposed to a corrosive environment throughout the whole range of potential and it is initially passivated but repassivation is not possible once when local corrosion starts.

3.2.3 Long-term electrochemical measurements

3.2.3.1 Commercially pure titanium

Results of EIS measurements of bare and ALD-coated cp-Ti specimens during immersion for 30 days in Hanks' solution at 37 °C are shown in **Fig. 3.20.** The measurement of Ti-20AL is shown for up to 15 days only because the protective properties of the film were lost soon after immersion (**Fig. 3.20 b**). Bare cp-Ti showed the usual EIS response associated with the passive film formation during the immersion period. Thus, an increase in impedance values and widening of the phase angle curve plateau at *ca.* −85° with immersion time can be observed (**Fig. 3.20 a**). The Ti-20AL film, due to its insulating properties, showed in the first five days a significant increase in impedance values at low frequencies of about 1.5 orders of magnitude, a broader plateau and higher phase angle values than bare cp-Ti. However, after 10 days, the film was dissolved from the cp-Ti substrate, resulting in the change in EIS plots becoming of the same shape as bare cp-Ti (**Figs. 3.20 a,b**).

Thicker alumina film, Ti-60AL, showed a stable EIS response over 30 days of the immersion period, with almost constant impedance and phase angle (**Figs. 3.20 c**). Impedance values are increased at low frequencies by two orders of magnitude compared to that of bare cp-Ti, and, in the mid-frequency range, the plateau of the phase angle values was close to −90°. The phase angle decreased slightly and rose again with decreasing frequency, indicating a diffusion process in the solid phase at the ALD film/electrolyte interface, as reported for Ti-6Al-4V specimens [164]. Namely, this would indicate the possibility of slow dissolution of ALD alumina film on the surface in contact with electrolyte.

After EIS tests, i.e. after 30 days of immersion, PDP tests were performed on these specimens (**Fig. 3.20 d)**. Since, in the course of the immersion period, the natural passive film of cp-Ti thickens, a positive shift in E_{corr} is observed, compared to that after 1 hour of immersion. Also, for the same reason, the shape of the curve changed. Starting from E_{corr} and towards more positive potentials, a much slower increase in current density was observed, the passive film being thicker (or more protective) than shortly after immersion. The increase was completely halted up to *ca.* 1 V when this thick and disordered passive film was transformed entirely to an insulating TiO_2 passive film. With a further increase of potential, the same processes occurred as after short immersion.

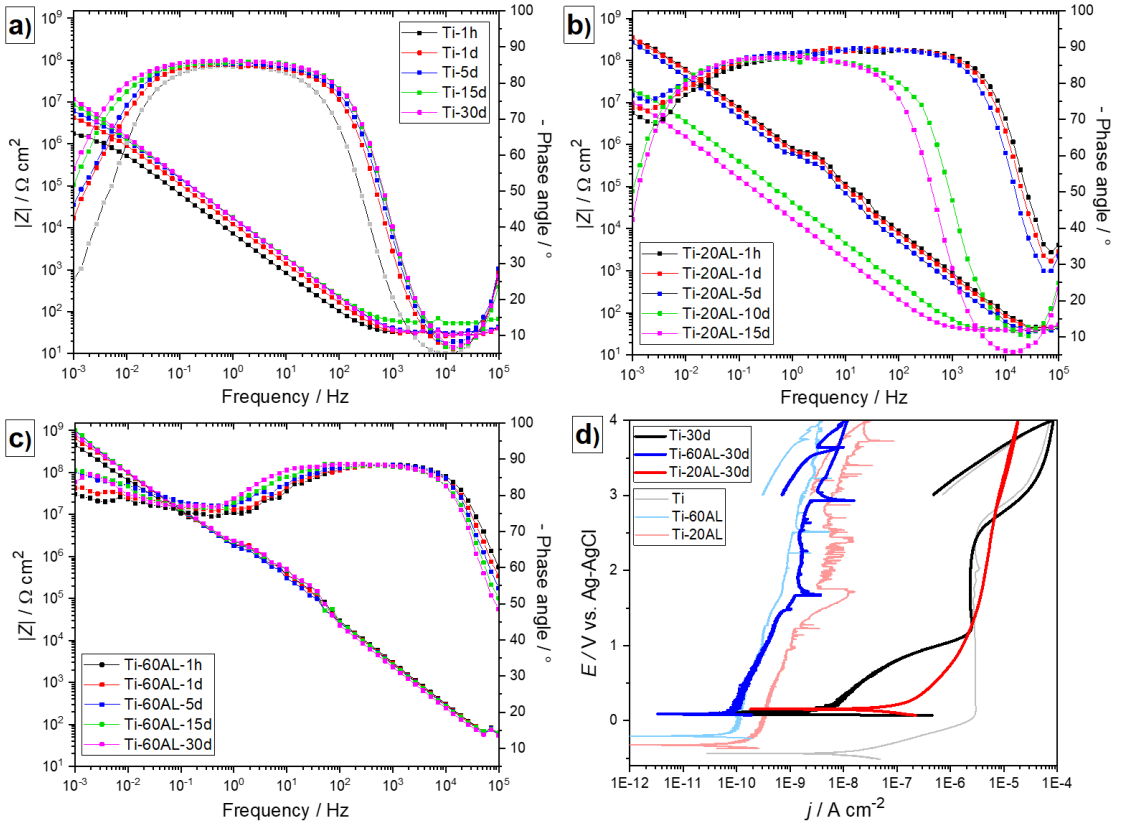

Figure 3.20: Bode plots recorded over 30 days of immersion in Hanks' solution at 37 °C for **a)** bare cp-Ti, **b)** cp-Ti coated with 20 nm of alumina and **c)** cp-Ti coated with 60 nm of alumina, and **d)** cyclic PDP curves recorded in Hanks' solution at 37 °C after the immersion period for 30 days of bare cp-Ti and of cp-Ti coated with 20 nm and 60 nm of alumina. The corresponding PDP curves obtained 1h after immersion (light-coloured) (**Fig. 3.18**) are shown for comparison $\mathrm{d}E/\mathrm{d}t = 1$ mV/s.

For the long-immersed ALD-coated cp-Ti specimens (**Fig. 3.20 d)**, the E_{corr} reached the same value as bare cp-Ti, i.e. shifted more positive for 300–400 mV than the values shortly after immersion. The passivation of the substrate surface can explain this shift by the Ti-oxide layer formed through the pores of ALD thin films. In other words, the same Ti-oxide passive layer was formed on the interface as on the uncoated cp-Ti specimens. The Ti-60AL-30d film retained the same j_{corr} as after a short immersion period (*ca.* 10^{-10} A cm^{-2}), i.e., its protective properties on cp-Ti were not diminished. But, in the case of Ti-20AL-30d, a different PDP response was noted (**Fig. 3.20 b**). A broad current density plateau was established with current densities as high as the uncoated sample. However, the shape of the curve differs from that of the bare specimen after long immersion. This change indicates the dissolution of the alumina thin film and blocking of the exposed surface by some precipitated layer from Hanks' solution, limiting the increase in the current density of the newly formed surface. To prove the formation of a new product, electrochemical data are supplemented by XPS analysis.

The XPS survey spectra of Ti-20AL, before and after immersion, are shown in **Fig. 3.21**. Before immersion, only Al and O originating from ALD coating and adventitious carbon are detected. After immersion, however, chemical elements, Ca and P, originating from Hanks' solution, are also detected. Since the behavior of cp-Ti in SBF electrolytes has already been well-studied, it is known that precipitation of different species from Hanks'

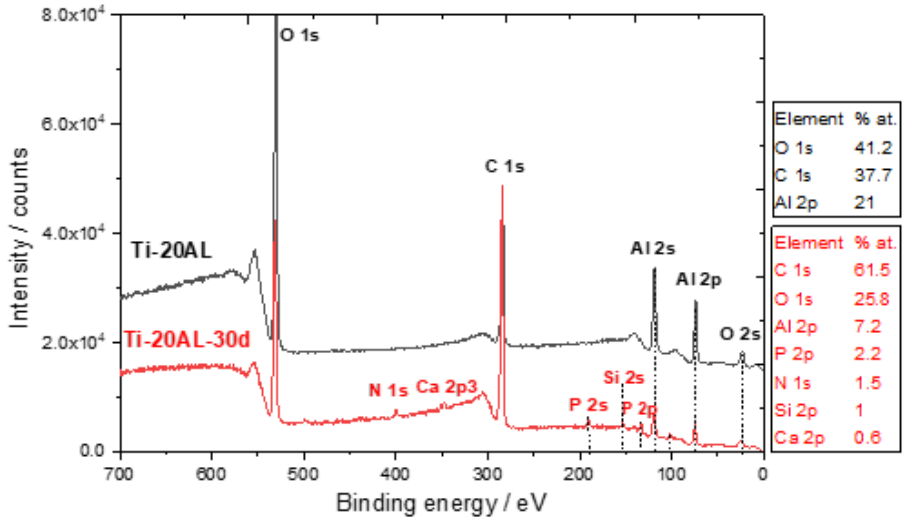

Figure 3.21: XPS survey spectra of cp-Ti with 20 nm alumina as-prepared (black curve) and after 30-day immersion period in Hanks' solution at 37 °C (red curve) with atomic concentrations of individual elements.

solution containing Ca and P ions commonly occurs [165]–[167]. This process can be further stimulated by applying a low potential excitation in the vicinity of E_{corr} [161]. It seems that this is what happens during EIS measurements, i.e., with the application of excitation AC voltage during EIS measurements, precipitation of calcium phosphates (i.e. hydroxyapatite) is encouraged. Another result that should be observed from XPS spectra is the significant reduction in the intensity of Al 2s and Al 2p peaks, indicating the removal of the alumina film (**Fig. 3.21**).

In **Fig. 3.22**, the high-resolution Al 2p and O 1s spectra are shown before and after immersion. The binding energy of the Al 2p peak center was 73.8 eV, as is characteristic of the alumina (Al-O bond). After immersion, however, the peak center shifted to 74.4 eV, which corresponds to the Al-OH bond, thus the hydrated form of alumina (**Fig. 3.22 a**). Also, the binding energy for the O 1s peak center shifted from 530.4 eV, which corresponds

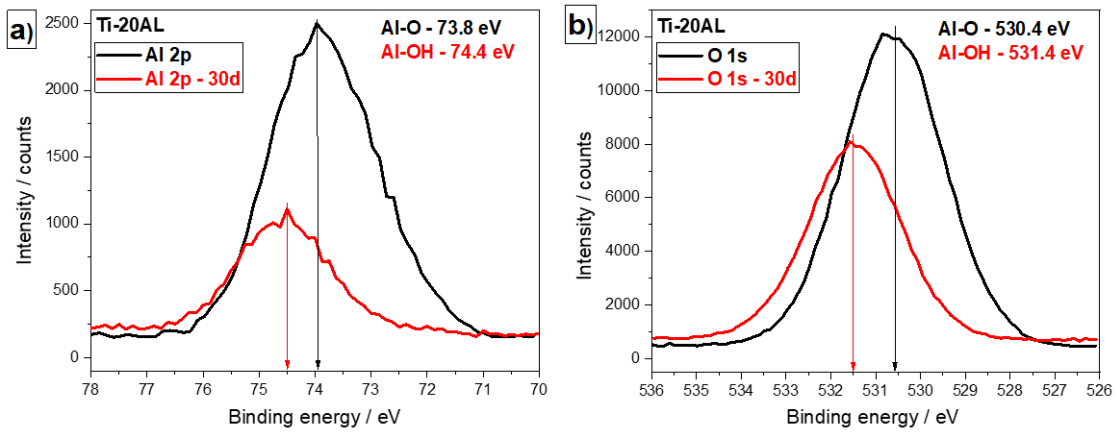

Figure 3.22: High-resolution XPS spectra of cp-Ti with 20 nm of alumina as prepared (black curves) and after a 30-day immersion period in Hanks' solution at 37 °C (red curves) for **a)** Al 2p and **b)** O 1s.

to Al-O bond, to 531.4 eV after immersion (**Fig. 3.22 b**), corresponding to the Al-OH bond [168]. Based on XPS and PDP results, we can conclude that the Ti-20AL film was dissolved to a certain extent during the immersion. The dissolution caused a significant increase in the current density during PDP tests, but precipitation of calcium phosphates from Hanks' solution limited the increase in current density at high potentials, i.e. causing a blocking effect (**Fig. 3.20 d**).

3.2.3.2 Stainless steel 316L

Bare and ALD-coated SS316L specimens were tested using long-term EIS measurements (**Fig. 2.23**). The bare SS316L showed a stable response over 30 days due to the formation of its passive film (**Fig. 3.23 a**). The growth and development of the passive film provided the increase in impedance values at the lowest frequencies, with the widening of the phase angle curve plateau with the immersion. Accordingly, there is a slight improvement in the insulating properties of the passive film on SS316L over time.

In the case of SS-20AL film, high initial protection can be observed (**Fig. 3.23 b**) since the impedance values at the lowest frequencies were increased by about two orders of magnitude relative to bare SS316L. Although the Bode impedance curves did not change

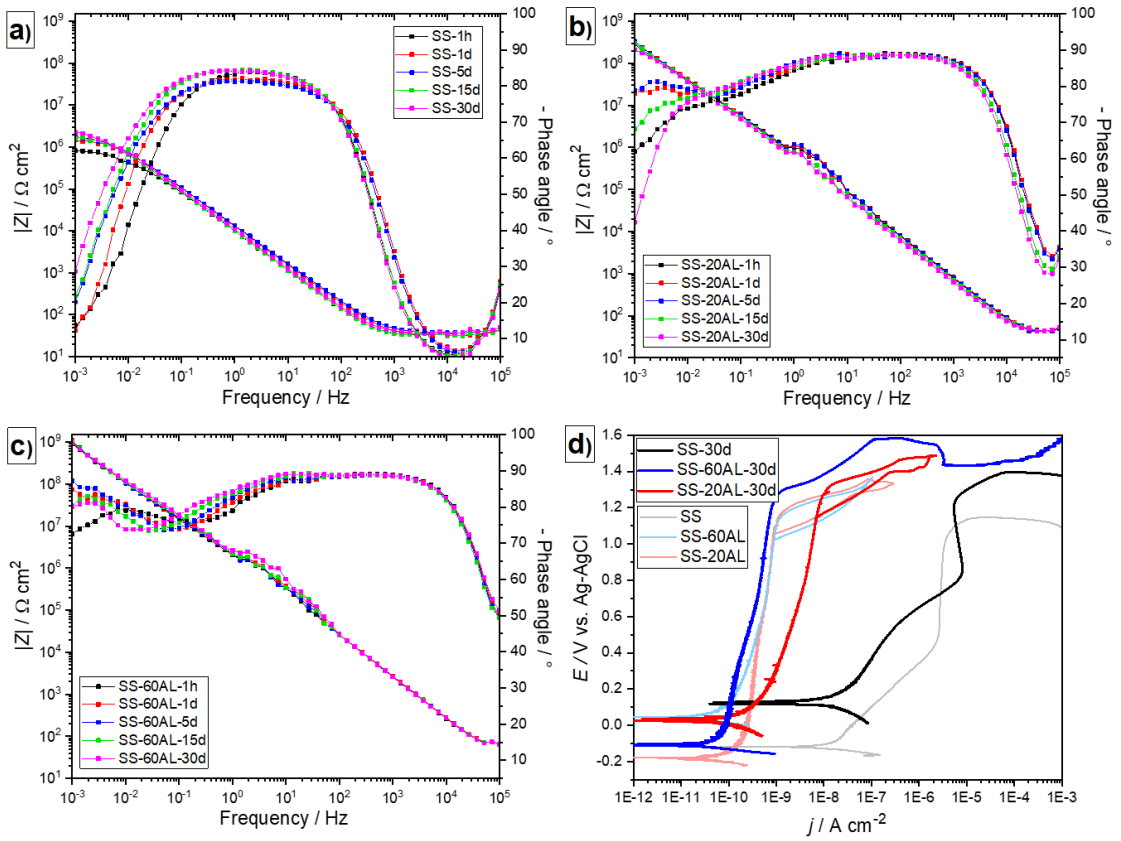

Figure 3.23: Bode plots recorded over 30 days of immersion in Hanks' solution at 37 °C for **a)** bare SS316L, **b)** SS316L coated with 20 nm of alumina and **c)** SS316L coated with 60 nm of alumina; and **d)** cyclic PDP curves recorded in Hanks' solution at 37 °C after the immersion period for 30 days of bare SS316L and of SS316L coated with 20 nm and 60 nm of alumina. The corresponding PDP curves obtained 1h after immersion (light-coloured) (**Fig. 3.19**) are shown for comparison. $\mathrm{d}E/\mathrm{d}t = 1$ mV/s.

significantly with immersion time, phase angle curves changed considerably. The values close to −85° and −60° were established at the plateau and low frequencies. The latter value first increased within the first five days and then decreased below −40° after 30 days.

The thicker film, SS-60AL, showed better protective properties as it resulted in impedance values at low frequencies to be about three orders of magnitude higher than on bare SS316L (**Figs. 3.23 c**), i.e. similar to that observed for the Ti-AL60 film (**Fig. 3.20 c**). The phase angle values at low frequencies, although being higher than for SS-20AL, still varied with the time of immersion, suggesting the occurrence of a diffusion process in the solid ALD films (**Figs. 3.23 c**). For SS-60AL, these values increased slightly in the first 5 days and then again decreased. Compared to the SS-20AL, the variations were much more minor, confirming that thicker film provides a better protective barrier.

The results of PDP measurements for SS316L, performed after 30 days of immersion, are shown in **Fig. 3.23 d**. Due to the passive film growth over more prolonged immersion, the E_{corr} and the anodic curve are shifted 0.2 V positively after 1 h of immersion. After increasing current density by about 1 order of magnitude above E_b at *ca.* 1.2 V, the corrosion process continued even after scan reversal, and the metal failed to repassivate itself. The SS-20AL-30d film showed a positive shift in E_{corr} relative to that after 1 h of immersion (**Fig. 3.23 d**). However, j_{corr} and j_{pass} were slightly higher, indicating a weaker film's protective properties. After the scan reversal, a loop was formed with an intersection at the E_p. The film has weakened to a certain extent, and electrolyte diffusion has progressed, but it still provides resistance and better protection than the naturally formed passive film on bare SS316L after 30 days. It also seems that the Ti-20AL film exhibited better properties when deposited on SS316L than on cp-Ti, as there is no noticeable dissolution on SS316L.

In the case of SS-60AL-30d film, the situation was somewhat more complex. It showed a negative shift of E_{corr}. The passive region was widened, but after scan reversal, the corrosion propagated (**Fig. 3.23 d**). To clarify why the thinner ALD alumina film on SS316L was able to re-passivate after the immersion in contrast to a thicker one, SEM/EDXS analyses were performed on a parallel set of samples (**Fig. 3.24**). The SS-20AL-30d film had numerous smaller pits, but the majority of the surface was undamaged, revealing the homogeneous coverage of the substrate by ALD film (**Fig. 3.24 a**). The EDXS analysis detected the elements originating from the film (Al, O) and underlying substrate (Fe, Cr, Ni) (**Fig. 3.24 a, Table 3.4,** spectrum 4).

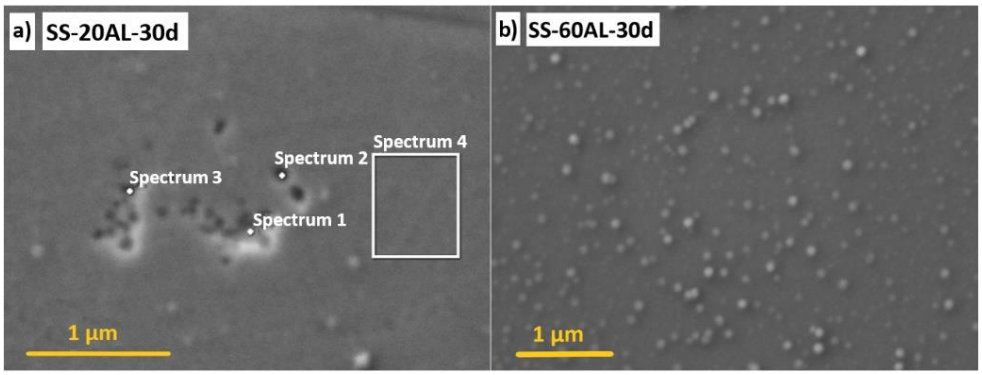

Figure 3.24: SEM images of SS316L with **a)** 20 nm of alumina and **b)** 60 nm of alumina thin film, after an immersion period of 30 days in Hanks' solution at 37 °C. Results of EDXS analyses of the film in **a)**, pits (spectra 1-3) and coating matrix (spectrum 4) are given in **Table 3.4**.

Table 3.4: Results of EDXS analysis on SS316L with 20 nm of alumina film after the immersion period of 30 days in Hanks' solution at 37 °C as shown in **Fig. 3.24 a**.

Element	Spectrum 1	Spectrum 2	Spectrum 3	Spectrum 4
C (at %)	1.3	1.8	2.1	3.5
O (at %)	1.2	4.1	3.4	7.0
Al (at %)	0.7	3.5	2.9	5.8
Cr (at %)	16.7	16.7	16.3	14.1
Fe (at %)	69.9	63.9	65.3	60.1
Ni (at %)	10.2	10.0	10.0	9.5
Total	100.0	100.0	100.0	100.0

The EDXS analyses made within the pits proved that these defects reached the SS316L substrate since the content of Al decreased significantly and those of Fe, Cr, and Ni increased (**Figs. 3.24 a, Table 3.4,** spectra 1-3) compared to the film matrix (spectrum 4). On the other hand, on SS-60AL-30d similar pits were not observed, and the film was uniform after the immersion period (**Fig. 3.24 b**). At first sight, these images and analyses contradicted the electrochemical results, where a substantial increase in current density was observed after scan reversal for SS-60AL-30d but not for SS-20AL-30d (**Fig. 3.23 d**).

However, these results can also serve as a basis for explaining such electrochemical behavior. In the case of SS-20AL-30d film, where electrolyte had access to the SS316L substrate in the pit defects during the immersion, passivation of SS316L can occur. SS316L has the ability to form the passive protective film based on Cr_2O_3. Combining very thin, 20 nm, ALD film with passivated SS316L in pits ensured the protection at high potentials and formed the small hysteresis loop between E_b and E_p (**Fig. 4.23 d**).

In contrast, in the case of SS-60AL-30d, where the film was free of such defects (**Fig. 3.24 b**), the SS316L substrate was not exposed to the electrolyte during the immersion period or PDP polarization. For this reason, when the potential reached high values (over 1.2 V), the alumina film relented, and SS316L was exposed to the electrolyte. Under such conditions, it cannot be passivated and is dissolved without the possibility of repassivation or ceasing pit growths. The supportive fact is that the j_{pass} of SS-60AL-30d is smaller than that of SS-20AL-30d (**Fig. 3.23 d**). Also, this specimen had E_b at slightly more positive values than the other two specimens since the film was defect-free and completely uniform. When the film relented, too high a potential caused progressive corrosion of the SS316L substrate. These features were not observed when deposited on cp-Ti since progressive localized corrosion did not occur on cp-Ti (**Fig. 3.20 d**).

3.2.4 Surface topography

The AFM-SKPFM technique measured the Volta potential difference (VPD) between a tip and the surface on bare specimens and those prepared with the ALD step. Additionally, measurement on the Ti-20AL flat specimen was performed, as it was a representative example of the insulative properties of alumina obtained by ALD. The SKPFM technique is relatively complex in specimens with an ALD step where the surface topography is non-homogeneous, as it may cause a faulty contrast of VPD values around the step. Therefore, for better understanding and interpretation of the obtained results, previous research work with a detailed explanation and discussion on the abilities of the SKPFM technique was used as a reference [169]. Unfortunately, in the case of specimens with ALD steps, where

the adhesive tape was used, the remaining glue made the measurement noisy, i.e. with an abundance of artefacts. However, removing artefacts in the software [135] made it possible to get more explicit images and desired information.

For metallic surfaces, there is no generally valid correlation between E_{corr}, which is measured electrochemically in an electrolyte, and VPD, which is measured in air and based on Coulombic forces between a tip and the specimen surface [169], [170]. In some cases, but not generally, the surface changes upon immersion. Nevertheless, materials with high VPD or work function energy (WFE, Φ) usually constitute a high corrosion resistance [171].

However, since ALD film is an oxide, i.e. a good insulator, and cp-Ti and SS316L alloys are good electrical conductors, it has been investigated whether the SKPFM technique can give beneficial results and whether those can still correlate with electrochemical results. It is essential to consider that the WFE of insulator oxides is undoubtedly different from that of the metals due to a different arrangement in their electronic states. Some new factors appear in the case of oxide material according to **Eq. 3.4**.

$$\Phi_{oxide} = \chi + E_g - (\mathrm{VBO} - E_g) \tag{3.4}$$

where, χ represents electron affinity, E_g is the band gap energy of the oxide film, VBO is valence band offset, and E_f represents a Fermi level energy in the oxide state [172].

Therefore, it can be expected that an enhancement in the magnitude of VPD or WFE can be anticipated in the metal oxides and ceramic oxide materials, as confirmed in the previous study [173]. Images of topography and VPD maps of chemically-mechanically polished cp-Ti and SS316L specimens are shown in **Fig. 3.25**. In the case of bare cp-Ti,

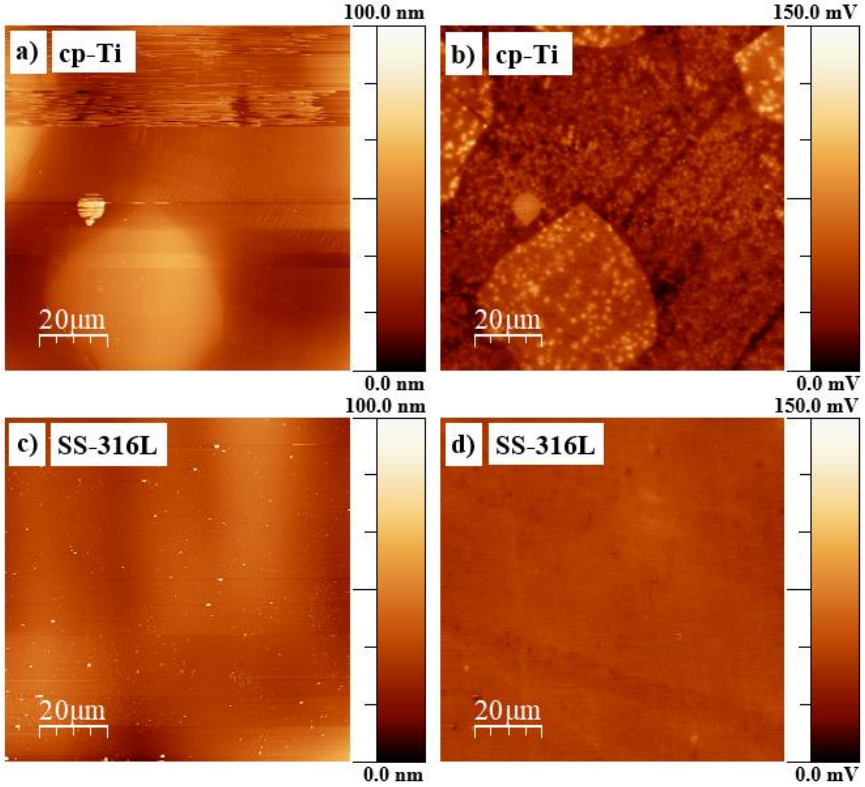

Figure 3.25: AFM-SKPFM images of bare cp-Ti and SS316L specimens; **a)** topographic image of cp-Ti, **b)** VPD on cp-Ti, **c)** topographic image of SS316L, and **d)** VPD on SS316L.

grains with different heights due to different effects of chemical-mechanical polishing can be observed (**Fig. 3.25 a**), which correlates well with SEM images (**Fig. 3.16 a**). In the corresponding VPD map, these grains can also be observed with slightly different VPD values (**Fig. 3.25 b**). Naturally formed TiO_2 passive film has very good insulating properties and a high dielectric constant [120], but its nanometric thickness is insufficient to allow uniform VPD values on the cp-Ti surface.

For SS316L, no grain boundaries can be observed in the topographic image nor differences in the VPD map (**Figs. 3.25 c,d**). Thus, although the SS316L surface was as smooth as that of cp-Ti, chemical-mechanical polishing did not have a significant chemical effect or etching on SS316L as on cp-Ti, which is also in line with an SEM investigation (**Fig. 3.16 b**). Therefore, from the AFM-SKPFM results, almost uniform topography and uniform VPD values over the SS316L surface can be deduced.

The AFM-SKPFM measurements on Ti-20AL and Ti-60AL films are shown in **Fig. 3.26**. Profile lines of these specimens (**Figs. 3.26 c,f**), which correspond to the blue lines on the topographic images (**Figs. 3.26 a,d**) confirm that the thickness of the deposited ALD films was about 20 and 60 nm, respectively. Unfortunately, these values can only be approximated due to the high proportion of noise around the ALD steps. Regarding VPD values, for Ti-20AL, the difference between ALD film and cp-Ti substrate ranged from 200 mV to 300 mV (**Fig. 3.26 b,c**). However, in the case of Ti-60AL, the value was *ca.* 100 mV (**Fig. 3.26 e,f**) is significantly less than for Ti-20AL and rather unexpected, given the larger thickness of this ALD film. Accordingly, this result does not correlate well with the E_{corr} shift from electrochemical results (**Fig. 3.18**). However, it can generally be concluded that more positive VPD values were obtained on ALD films due to their higher WFE value corresponding to the dielectric or insulating properties, which influence the electron transfer strongly and, in turn, electrochemical interactions at solid/solution interfaces.

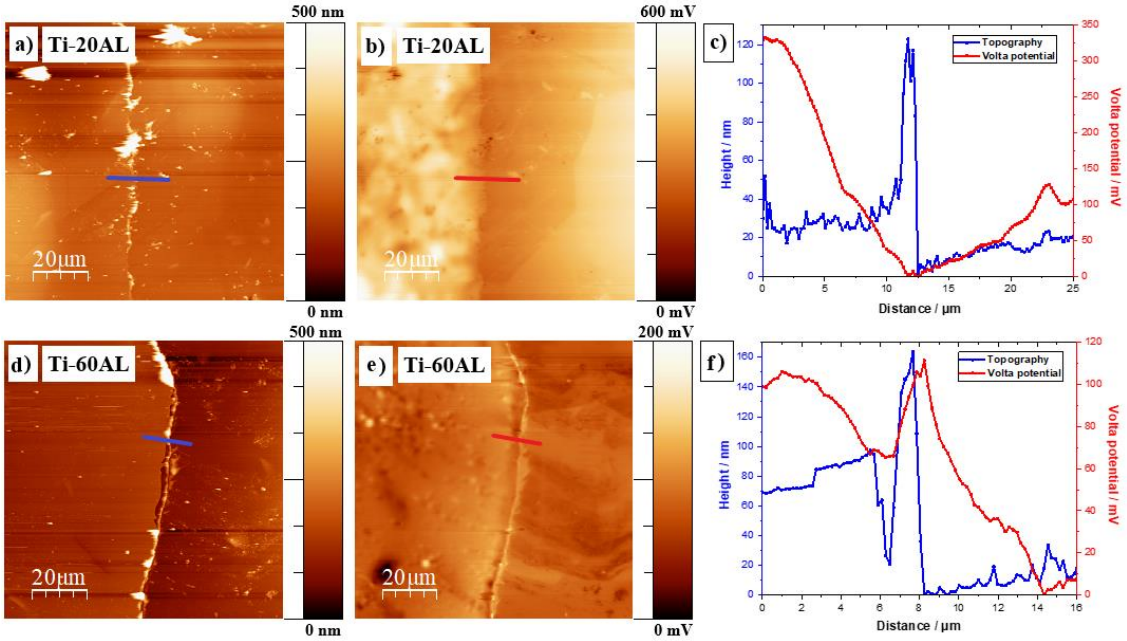

Figure 3.26: AFM-SKPFM images and line profiles on the step of alumina films on cp-Ti; **a)** topographic image of 20 nm of alumina, **b)** VPD of 20 nm of alumina and **c)** their 2D profiles marked with the blue and red lines; **d)** topographic image of 60 nm of alumina, **e)** VPD of 60 nm of alumina and **f)** their 2D profiles marked with the blue and red line.

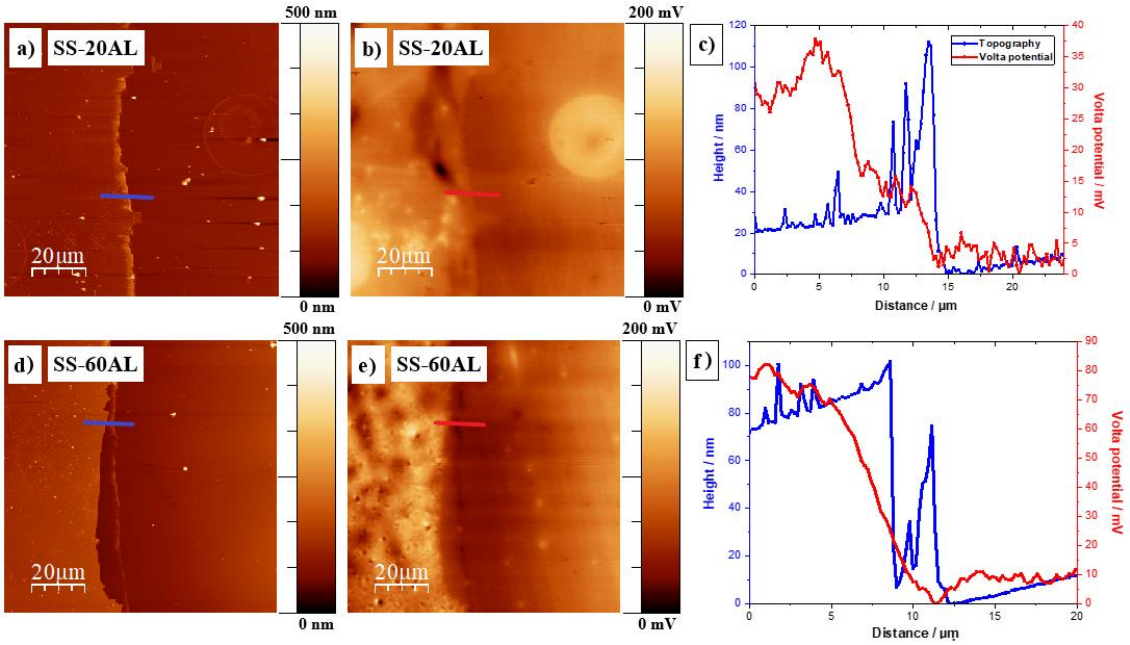

Figure 3.27: AFM-SKPFM images and line profiles on the step of alumina films on SS316L; **a)** topographic image of 20 nm of alumina, **b)** VPD of 20 nm of alumina and **c)** their 2D profiles marked with the blue and red line; **d)** topographic image of 60 nm of alumina, **e)** VPD of 60 nm of alumina and **f)** their 2D profiles marked with the blue and red line.

AFM-SKPFM measurements also provided quite complex results on SS316L specimens that require careful interpretation (**Fig. 3.27**). The determined thicknesses of SS-20AL and SS-60AL films approximate the results expected according to the ALD recipes. The SS-20AL had VPD values slightly more positive than SS316L substrate with a difference of *ca.* 30 mV on a given line profile (**Fig. 3.27 c**). For the SS-60AL, the difference was slightly larger, *ca.* 70 mV (**Fig. 3.27 f**), which may be related to the difference in thickness of these films. However, again as in the case of cp-Ti specimens, it is not possible to find a matching relationship with electrochemical measurements (**Fig. 3.19**). This discrepancy is because, with electrochemical measurements, the specimens are in solution, and a significant role is played by the processes taking place within pores in the ALD film, which could affect E_{corr} values. On the other hand, it may be challenging to use SKPFM to detect

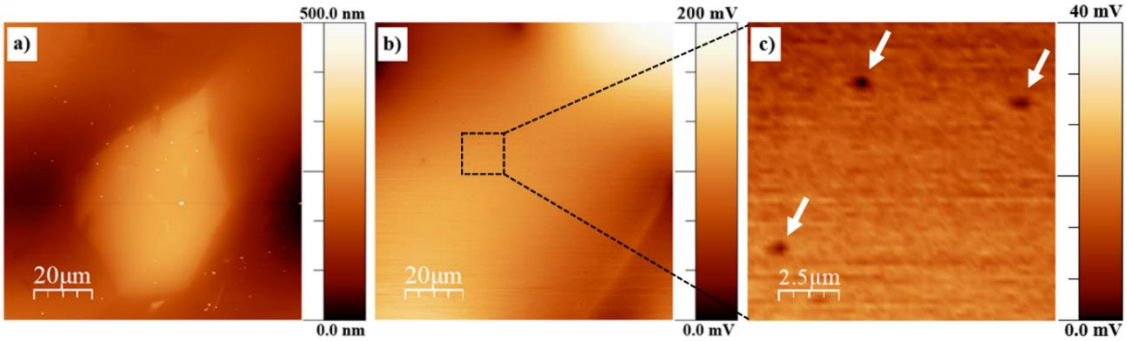

Figure 3.28: AFM-SKPFM images of flat 20 nm alumina film on cp-Ti; **a)** topographic image, **b)** VPD map, and **c)** VPD map **b)** magnified 8-fold.

very narrow pores of nanometric size, especially if they have a curving path to the substrate.

In addition to those performed on specimens with ALD steps, measurements were also carried out on the flat surface of Ti-20AL, where no noise was present. A representative example of the insulating properties of ALD alumina thin film is given in **Fig. 3.28**. The topographic image shows a crystal grain on the cp-Ti surface as a clear bump coated with 20 nm alumina film (**Fig. 3.28 a**). However, almost uniform values of VPD over the whole surface were observed without a visible crystal grain effect (**Fig. 3.28 b**). The uniformity of VDP shows that Ti-20AL film completely insulated the cp-Ti surface. SKPFM did not detect any outline of this grain that would otherwise cause different VPD values, as shown on bare cp-Ti specimens (**Fig. 3.25 b**). However, when a selected area of the VPD map was magnified, tiny dots of low VPD values can be observed, suggesting that these features may be related to black spots detected under the SEM investigation (**Fig. 3.17 b**). It is noteworthy that, based on PDP curves, it was concluded that these are rather surface dents or regions with a slight deficiency of oxygen in oxide film [174] than defects reaching the metal surface. Otherwise, a vast reduction of j_{corr} values would not be achieved for Ti-20AL compared to bare cp-Ti (**Fig. 3.18)**.

3.2.5 Summary

Similar to cp-Ti, the SS316L surface can also be efficiently polished with chemical reagents, H_2O_2 and NH_4OH. Both alumina thin films, 60 nm and 20 nm in thickness, are uniform, completely covering cp-Ti and SS316L substrate surfaces.

PDP tests did not reveal significant effect of the film thickness since both alumina thin films provided almost equal barrier protection of both substrates. However, the effect of thickness proved to be significant only after long-term EIS measurements. Thus, 20 nm thin film failed after *ca.* 10 days of immersion in the case of cp-Ti, while for SS316L specimens the film weakened over time but remained stable. Therefore, chemically different substrates provide different conditions for the formation of a stable alumina film. On the other hand, 60 nm thick films showed much better stability on both substrates over time.

PDP tests on SS316L after 30-day immersion period showed that the barrier properties of the film in combination with the ability of repassivation of the SS316L surface can provide conflicting results. For example, at high potentials, 60 nm thick film did not provide repassivation, but a thinner film that allowed passivation of the substrate surface with increasing potential, was able to repassivate. In other words, the weak property of the thinner film, i.e. its porosity, at high potentials enabled repassivation and seemingly better protective properties than the thicker film.

3.3 The Effect of ALD Multilayer Structure Al_2O_3-HfO_2-Al_2O_3 Deposited on cp-Ti and SS316L on Their Protective Properties

This section is closely related to Section 3.2, as here, the multilayer structure of ALD thin films is compared with the single alumina thin film of 60 nm (also shown in Section 3.2). Therefore, some results of pure alumina film of 60 nm are repeated in this section for comparison with multilayer films and a more straightforward discussion of the results.

3.3.1 Morphology, adhesion and thickness of ALD films

The features and characteristics of the polished substrate surfaces are described in Section 3.2.1, and their SEM micrographs are shown in **Fig 3.16**.

The black spots on the surface of Ti-60AL and SS-60AL films (**Fig. 3.29 a,c**), which are only surface features, were not observed in the case of multilayer films, i.e. Ti-60ML and SS-60ML (**Fig. 3.29 b,d**). In multilayer films, the deposit is formed through three separate deposition processes. However, these spots do not affect the protective properties of single layers because those are comparable to multilayer films by protective properties (Section 3.3.2), where there are no such surface features. Therefore, it could be assumed that these features are related to the continuous growth of alumina thin films.

The hafnia thin film causes agglomerates' appearance, which, due to the transparency of these films, can be seen as bright, round areas in the multilayer thin films (**Fig. 3.29 b,d**). The surface appearance differed on cp-Ti and SS316L, with the agglomerates being denser on SS316L, and the surface looked interspersed (**Fig. 3.29 d**). Agglomerates have

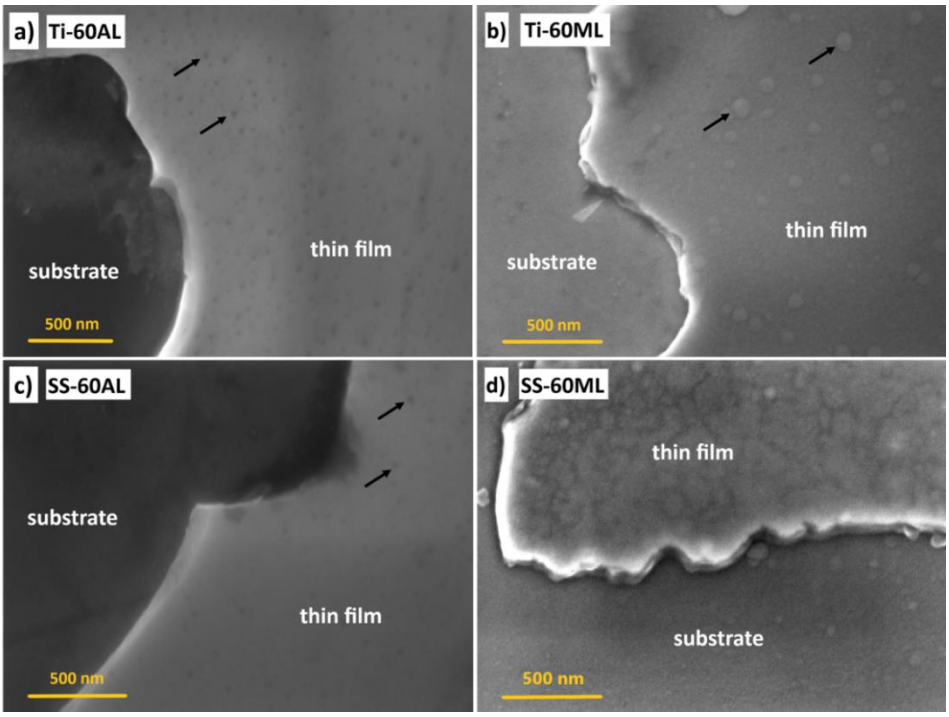

Figure 3.29: SEM images of the step site between ALD film and substrates for the **a)** 60 nm of alumina on cp-Ti, **b)** 60 nm of multilayer on cp-Ti, **c)** 60 nm of alumina on SS316L, and **d)** 60 nm of multilayer on SS316L. Arrows denote black spots and agglomerates.

also been found in alumina thin films, but to a lesser extent (see **Fig. 3.37 b**). In **Fig. 3.29 a,c,** the agglomerates are not visible due to large magnification and SEM conditions.

Another feature may reveal some mechanical properties of these thin films. Ti-60AL and SS-60AL films show smooth fracture area or step lines **(Fig. 3.29 a,c)**, while for Ti-60ML and SS-60ML, these features are irregular and look more brittle **(Fig. 3.29 b,d)**. This difference is the result of hafnia film in the multilayer structure, which has mechanical

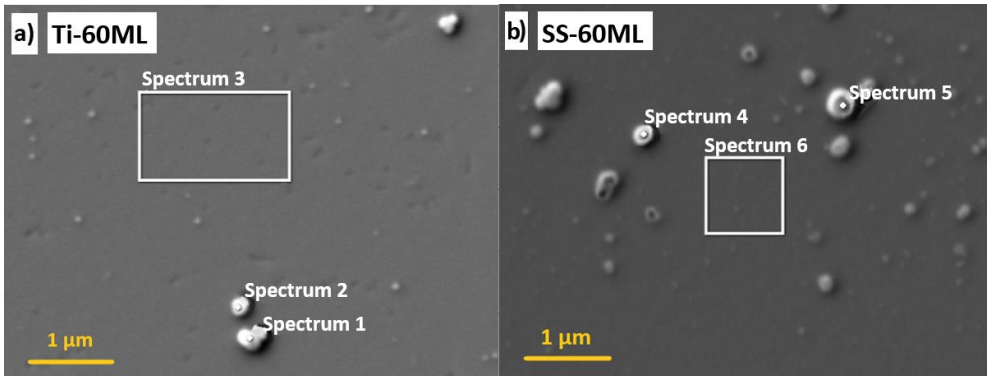

Figure 3.30: SEM images of **a)** cp-Ti with 60 nm of multilayer and **b)** SS316L with 60 nm of the multilayer. White rectangles represent the sites at which the composition of the film matrix was analysed by EDXS (spectra 3 and 6), and labelled points the sites at which composition at individual agglomerates were analysed (spectra 1, 2, 4, 5) (**Tables 3.5 and 3.6**).

Table 3.5: Results of EDXS analysis on cp-Ti with 60 nm of multilayer shown in **Fig. 3.30 a**.

Element	Spectrum 1	Spectrum 2	Spectrum 3
O (at %)	33.3	30.2	24.5
Al (at %)	13.7	13.0	9.8
Ti (at %)	21.6	27.2	41.9
Hf (at %)	31.4	29.6	23.8
Total	100.0	100.0	100.0

Table 3.6: Results of EDXS analysis on SS316L with 60 nm of multilayer shown in **Fig. 3.30 b**.

Element	Spectrum 4	Spectrum 5	Spectrum 6
O (at %)	31.3	25.9	22.7
Al (at %)	14.9	14.9	13.3
Fe (at %)	15.9	22.9	30.2
Ni (at %)	2.3	2.8	4.3
Hf (at %)	35.6	33.5	29.5
Total	100.0	100.0	100.0

properties different from alumina, affecting the mechanical properties of the entire multilayer film. Therefore, ALD hafnia thin film tends to form crystalline grains, possibly associated with agglomerates, which cause coarse step lines when the film breaks. This is proved later by TEM analysis (Section 3.4).

EDXS analysis was combined with SEM recorded at smaller magnification to characterize the surface and various surface features. SEM/EDXS analyses of Ti-60ML and SS-60ML surfaces are shown in **Fig. 3.30**. At this magnification, it became apparent that even larger agglomerates are formed on the surface of multilayer (**Figs. 3.29 b,d**). First, the matrix surface was analyzed (marked by white rectangles). For Ti-60ML, Al, Hf, O and Ti were detected (**Fig. 3.30 a, Table 3.5**, spectrum 3). Since the depth of EDXS analysis exceeds the thickness of ALD film, Ti originating from the substrate is also detected. Similarly, Hf, Al, O, Fe and Ni are detected for SS-60ML, the latter two elements originating from the substrate (**Fig. 3.30 b, Table 3.6**, spectrum 6). Analysis of agglomerates showed that they were enriched with the film constituent elements, i.e. Al, Hf and O (**Fig 3.30**, **Tables 3.5 and 3.6**, spectra 1, 2, 4, 5). Since hafnia tends to form agglomerates more than alumina, these are predominantly from hafnia but coated with a top alumina layer. The exact origin of these agglomerates remains to be elucidated. However, it can be hypothesized that to some extent, their formation may be related to polishing imperfections. Although, they may be formed spontaneously due to the local conditions during the deposition process, as stated here [129]. It is noteworthy that no cracks and no pores could be observed at the film surface, at least not using this SEM magnification.

The Vickers hardness test, with subsequent SEM investigation, was used to estimate the resistance to delamination or detaching ALD films from the substrates, as described in Section 2.4. SEM images of Vickers indentation sites on 60AL and 60ML films on both substrates, cp-Ti and SS316L, are shown in **Fig. 3.31**. There was no detachment of any

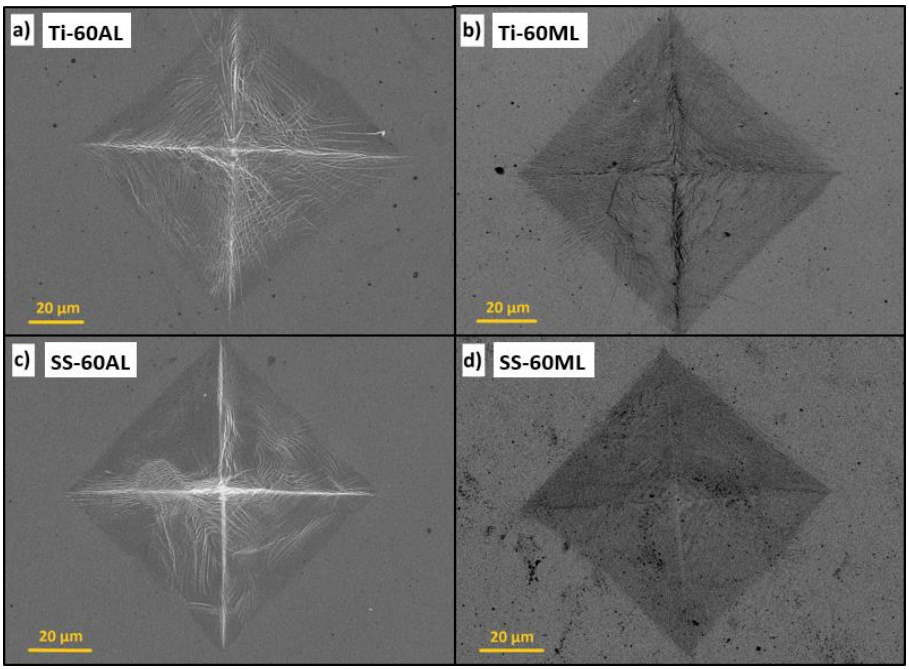

Figure 3.31: SEM images of resistance to detaching of ALD films using the Vickers indentation test with 20 N for **a)** 60 nm of alumina on cp-Ti, **b)** 60 nm of multilayer on cp-Ti, **c)** 60 nm of alumina on SS316L, and **d)** 60 nm of multilayer on SS316L as substrate.

ALD thin films. Hence, the area of delamination could not be measured. This indicates very good adhesion of these films on polished surfaces of cp-Ti and SS316L. These results are significant as they differ from an earlier study, where ALD alumina and titania films, in a single-layer and multilayer structure, were reported to be susceptible to delamination on SS316L substrate [97].

3.3.2 Short-term electrochemical measurements

The comparison of PDP curves of bare and ALD-coated cp-Ti after 1 hour of immersion at the OCP in simulated physiological Hanks' solution at 37 °C is presented in **Fig. 3.32**. The behavior of cp-Ti under these conditions, i.e. its passivation, has been described in Section 3.1.3.

For the coated cp-Ti specimens, E_{corr} and j_{corr} are almost identical for thin films Ti-60AL and Ti-60ML. For Ti-60ML, E_{corr} value is shifted positively by ca. 0.1 V, compared to cp-Ti, while for Ti-60AL, the shift is slightly higher. Further, the j_{corr} value was reduced equally by about two orders of magnitude for both thin films and cp-Ti. It indicates that the insulative properties are the same for both thin films, at least in the short period after immersion. Further, with increasing potential, both thin films provided significant resistance to an increase in current density. Thus, the curves for Ti-60AL and Ti-60ML show no significant differences indicating similar behavior of single and multilayer structures (**Fig. 3.32**). According to previous studies, different ALD multilayer configurations usually showed a greater reduction in the j_{corr} values than ALD single-layer films of the same thickness [97], [103], but this was not the case in the present study. Applying the reverse potential scan, the current density decreased for Ti-60ML, the same as Ti-60AL. This is due to the combination of very insulative passive film of cp-Ti and ALD film and oxygen consumption from the electrolyte, as described in Section 3.1.3.

In the case of the SS316L specimens (**Fig. 3.33**), cyclic PDP curves are different compared to cp-Ti due to the susceptibility of SS316L to pitting corrosion as described in the previous chapter. The electrochemical behavior of bare SS316L did not show repassivation (as described in Section 3.2.2.). The coated specimens show a repassivation loop. Similarly to coated cp-Ti, the j_{corr} values for SS-60ML and SS-60AL were reduced by

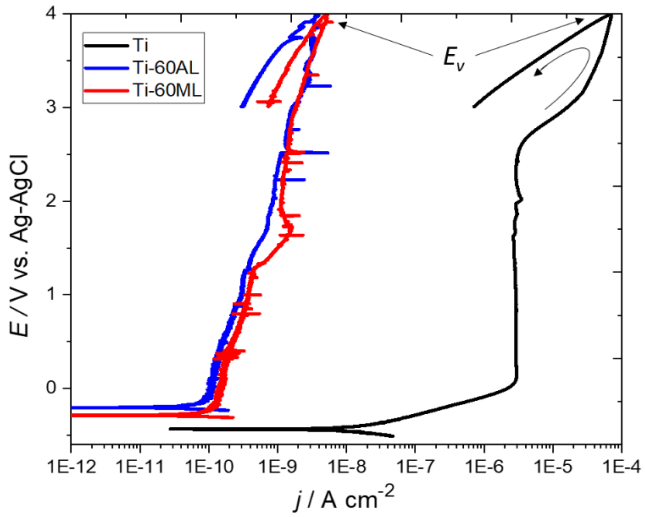

Figure 3.32: Cyclic PDP curves recorded in Hanks' solution at 37 °C of bare cp-Ti, cp-Ti coated with 20 nm of alumina and 60 nm of multilayer thin films. $dE/dt = 1$ mV/s.

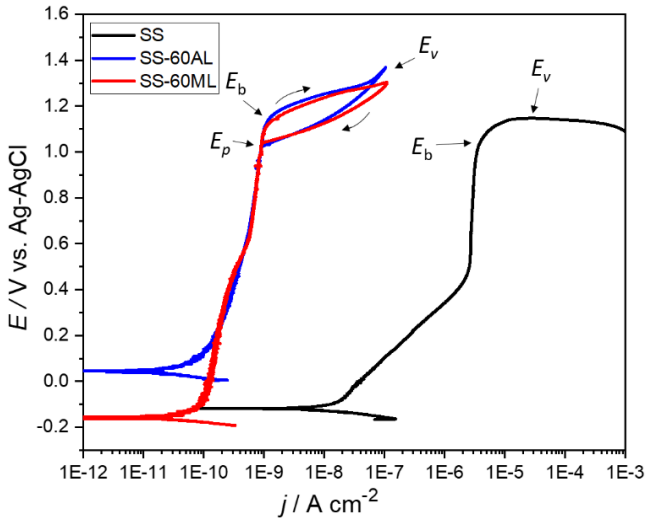

Figure 3.33: Cyclic PDP curves recorded in Hanks' solution at 37 °C of bare SS316L, SS316L coated with 20 nm of alumina and 60 nm of multilayer thin films. $dE/dt = 1$ mV/s.

about two orders of magnitude compared to bare SS316L. However, the E_{corr} values were slightly different. For SS-60AL, the E_{corr} is shifted positively by about 0.15 V while, for SS-60ML, it shifted slightly negative compared to bare SS316L

SS-60ML breaks down at the same potential as SS-60AL, around 1.2 V, i.e. slightly more positive than the passive film on bare SS316L. Above E_b the current density increased rapidly. After scan reversal, the loop was formed for both thin films (**Fig. 3.33**). The intersection point of the reverse and forward curves is at 1 V, giving the pitting protection potential (E_p). Therefore, both SS-60AL and SS-60ML thin films can stop the propagation of localized or pitting corrosion on SS316L substrate and allow SS316L to repassivate through pores in the film.

3.3.3 Long-term electrochemical measurements

3.3.3.1 Commercially pure titanium

Results of EIS and PDP tests of bare and coated cp-Ti specimens during immersion for 30 days in Hanks' solution at 37 °C are shown in **Fig. 3.34.** The bare cp-Ti specimen has a stable response due to passive film formation during immersion (**Fig 3.34 a**), as described in Section 3.1.3.

Multilayer thin film, Ti-60ML, showed a stable EIS response over 30 days of the immersion period, with almost constant values of impedance and phase angle, similar to the Ti-60AL (**Figs. 3.34 b,c**). Impedance values increased at low frequencies by two orders of magnitude compared to that of bare cp-Ti, and, in the mid-frequency range, the plateau of the phase angle values was close to −90° (**Fig. 3.34 b**). With decreasing frequency, the phase angle of Ti-60AL decreased slightly and rose again, indicating a diffusion process in the solid phase at the ALD film/electrolyte interface. For Ti-60ML, the phase angle curve plateau was noticeably wider than for Ti-60AL, probably due to the hafnia thin film in the multilayer structure, which may provide better resistance to diffusion, i.e. better insulating properties than alumina. Interestingly, it has been shown by XPS depth profile analysis (**Fig. 3.35**) that the outer alumina layer was dissolved after 30 days of immersion, but the hafnia layer remained stable and provided protection.

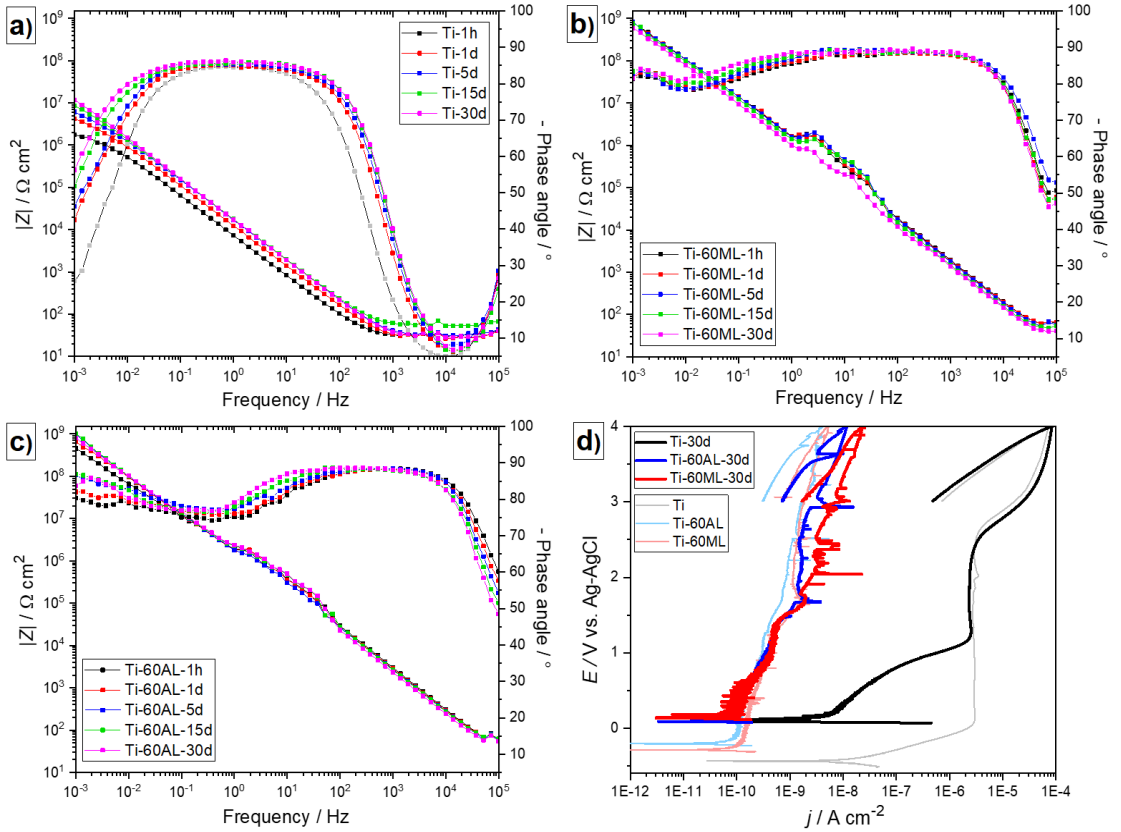

Figure 3.34: Bode plots recorded over 30 days of immersion in Hanks' solution at 37 °C for **a)** bare cp-Ti, **b)** cp-Ti coated with 60 nm of multilayer and **c)** cp-Ti coated with 60 nm of alumina, and **d)** cyclic PDP curves recorded in Hanks' solution at 37 °C after the immersion period for 30 days of bare cp-Ti and of cp-Ti coated with 60 nm of multilayer and 60 nm of alumina. The corresponding PDP curves obtained 1h after immersion (light-coloured) (**Fig. 3.32**) are shown for comparison $\mathrm{d}E/\mathrm{d}t = 1$ mV/s.

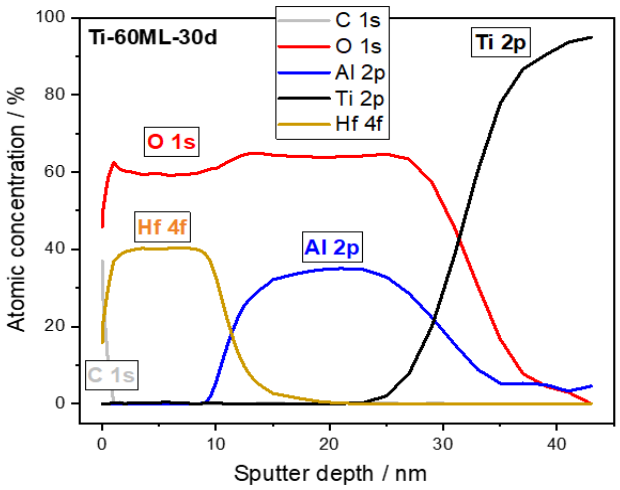

Figure 3.35: XPS depth profile of the 60 nm of multilayer film deposited on cp-Ti after 30-day immersion period in Hanks' solution at 37 °C.

Therefore, very thin ALD alumina film, of ca. 20 nm, is prone to dissolution and is unstable, and as such, cannot provide barrier protection, as also shown in Section 3.2 (**Fig. 3.21 and 3.22**).

PDP tests were performed on these specimens after 30 days of immersion (**Fig. 3.34**). The behavior of the bare cp-Ti specimen is described in Section 3.1.3. For the Ti-60ML and Ti-60AL thin films, the E_{corr} reached the same value as bare cp-Ti, i.e. shifted more positive for 300–400 mV than shortly after immersion. Therefore, both films seem porous and allow surface passivation by the Ti-oxide layer formed through its pores. The same Ti-oxide passive layer was formed as on the uncoated cp-Ti specimens, as they reached the same E_{corr} value. Further, the j_{corr} value remained the same for Ti-60AL and Ti-60ML, as, after a short immersion period (*ca.* 10^{-10} A cm^{-2}), i.e. their protective properties on cp-Ti were not diminished.

3.3.3.2 Stainless steel 316L

The long-term EIS tests and accompanying PDP tests for bare and coated SS316L specimens are shown in **Fig. 3.36**. Like bare cp-Ti, bare SS316L shows a stable response due to passive film formation during immersion (**Fig 3.36 a**), as described in Section 3.2.3.

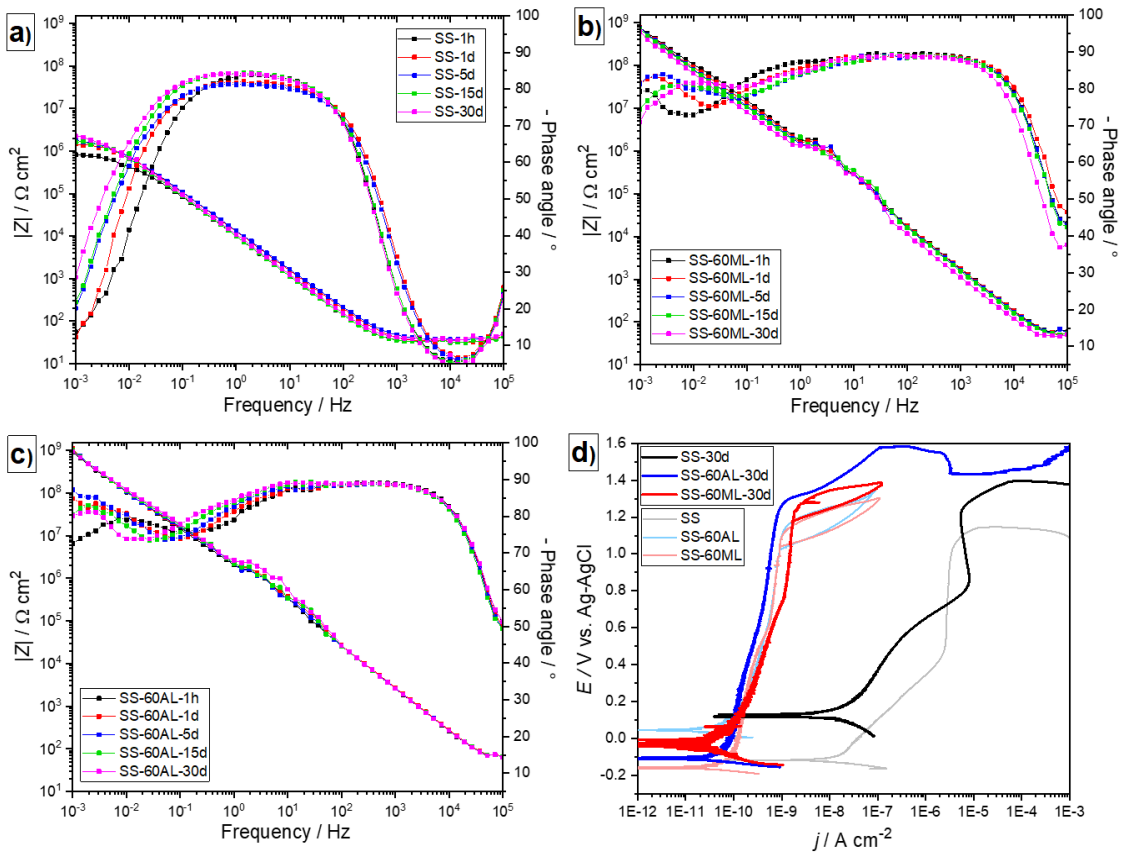

Figure 3.36: Bode plots recorded over 30 days of immersion in Hanks' solution at 37 °C for **a)** bare SS316L, **b)** SS316L coated with 60 nm of multilayer and **c)** cp-Ti coated with 60 nm of alumina, and **d)** cyclic PDP curves recorded in Hanks' solution at 37 °C after the immersion period for 30 days of bare SS316 L and of SS316L coated with 60 nm of multilayer and 60 nm of alumina. The corresponding PDP curves obtained 1h after immersion (light-coloured) (**Fig. 3.33**) are shown for comparison $dE/dt = 1$ mV/s.

The ALD-coated SS316L specimens, SS-60AL and SS-60ML, showed significant protective properties as they provided impedance values at low frequencies to be about three orders of magnitude higher than on bare SS316L (**Figs. 3.36 b,c**). This is analogous to the behavior of the thin films on cp-Ti as a substrate (**Figs. 3.34 b,c**). However, the values of the phase angle at low frequencies varied with the time of immersion, suggesting the non-stability and probably occurrence of a diffusion process in the solid ALD films. Comparing the SS-60AL and SS-60ML thin films, it can be observed that there is a slightly wider plateau of phase angle values (close to −90°) in the case of the SS-60ML. Similar behavior was observed for cp-Ti specimens (**Figs. 3.34 b,c**), but the difference with SS316L is somewhat less pronounced (**Fig. 3.36 b,c**). Therefore, using EIS measurements, it was found that the difference between single and multilayer combinations lies in only a slightly more extended plateau of high phase angle values in a multilayer configuration. The reason is associated with its more substantial insulating properties. However, significant drawbacks for multilayer films were also revealed (*vide infra*).

The PDP tests for SS316L specimens performed after 30 days of immersion are shown in **Fig. 3.36 d**. The bare SS316L specimen, due to the formation of its passive film, retained relatively good corrosion properties, as explained in Section 3.2.3. The PDP curve of the multilayer film on the SS316L after 30 days of immersion, SS-60ML-30d, was almost the same as after 1 hour. This behavior indicates good stability of multilayer thin film and the ability of the SS316L substrate to repassivate itself at relatively high potentials when a reverse scan is applied. However, reference should be made here to the SS-60AL-30d thin film, its defect-free surface (**Fig. 3.24 b**) without the possibility of repassivation because the substrate is not exposed and thus not able to form a passive film, as explained in Section 3.2.3. Thus, analogously to the SS-20AL-30d, it can be inferred that this film, SS-60ML-30d, has defects that expose the SS316L substrate to the electrolyte, allowing it to repassivate itself. This has been investigated further by SEM/EDXS analysis.

The surface of the SS-60ML-30d is shown in **Fig. 3.37 a**. Although the SS-60ML-30d surface was free of pits, as observed for SS-20Al-30d (**Fig. 3.24 a**), some larger defects surrounded by agglomerates have been observed. At the matrix of the multilayer film and at agglomerates (**Table 3.7,** spectra 3 and 2, respectively), the

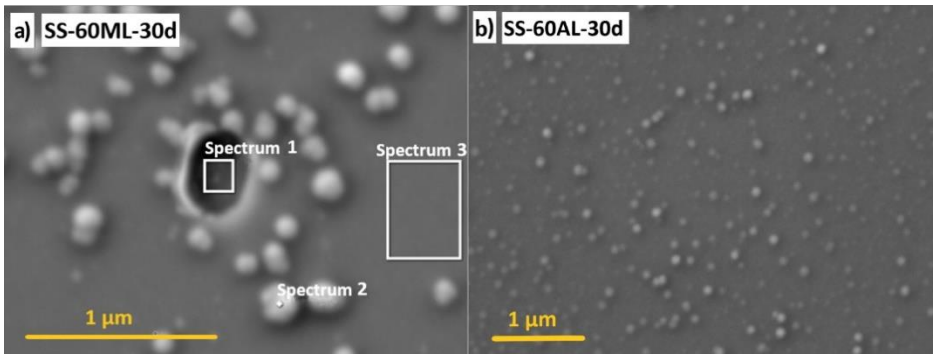

Figure 3.37: SEM images of SS316L with **a)** 60 nm of multilayer thin film and **b)** 60 nm of alumina thin film, both after an immersion period of 30 days in Hanks' solution at 37 °C. Corresponding EDXS analyses for **a)** are given in **Table 3.7** (defects (spectrum 1), agglomerates (spectrum 2) and coating matrix (spectrum 3)).

Table 3.7: Results of EDXS analysis on SS316L with 60 nm of multilayer film after an immersion period of 30 days in Hanks' solution at 37 °C as shown in **Fig. 3.37**.

Element	Spectrum 1	Spectrum 2	Spectrum 3
C (at %)	2.7	2.1	2.2
O (at %)	4.7	22.7	27.4
Al (at %)	1.6	12.5	14.7
Cr (at %)	16.2	0.0	0.0
Fe (at %)	64.6	25.4	15.3
Ni (at %)	9.5	3.4	2.1
Hf (at %)	0.7	33.9	38.3
Total	100.0	100.0	100.0

concentrations of Al and and Hf are similar as before the immersion (**Fig. 3.30 b**, **Table 3.6**, spectra 6 and 5, respectively). The concentrations of elements coming from the substrate are strongly reduced, e.g. Cr is not even detected. At the defect site (**Fig. 3.37 a**, **Table 3.7,** spectrum 1), however, Al content is reduced, and that of substrate elements increases. Such sites, where many agglomerates are concentrated in the multilayer, can cause poor mechanical properties of the film, i.e. detaching, cracking, formation of defects, etc.

On the surface of the SS-60AL-30d, the presence of such agglomerates can also be seen, but without defects (**Fig. 3.37 b**). This means that the formation of the hafnia interlayer may harm the stability of the multilayer film under the stated conditions. These results, including electrochemical behavior, contradict some earlier studies on ALD multilayer thin films, though not combined with alumina and hafnia. They have presented the multilayer structure of ALD films as advantageous regarding their protective and mechanical properties compared to single-layer films [97], [103]. It can be hypothesized that such agglomerates may induce some internal stress or mismatch at specific sites in the multilayer structure, leading to the mechanical detachment and dissolution of the ALD film. However, during the immersion and subsequent polarization, the SS316L surface is still well protected as the formation of a hysteresis loop is observed, again due to repassivation of the underlying surface (**Fig. 3.36 d**).

3.3.4 Summary

Unlike single-layer alumina thin films, which show high uniformity, multilayer films due to the presence of hafnia are interspersed with agglomerates. After a long-term immersion, this will later prove as a drawback due to possible delamination or peeling of the film around the agglomerate sites.

Long-term EIS measurements have shown that multilayer thin films retain good barrier properties as well as single-layer alumina thin films. However, PDP tests after immersion period have shown that there are significant differences in the protective properties of these two thin films. Namely, multilayer thin films, due to presence of the agglomerates and the tendency to leak electrolyte with increasing potential, allow repassivation of the SS316L substrate. However, with single-layer alumina thin film, due to excellent barrier properties, passivation of the SS316L substrate does not occur with increasing potential, and finally when local corrosion starts, there is no possibility of repassivation.

3.4 Biocompatibility and Antibacterial Properties of Al_2O_3 and HfO_2 ALD Thin Films Deposited on cp-Ti and SS316L

The properties of ALD alumina and hafnia thin films deposited at different temperatures, 180 °C and 260 °C (Section 2.2), were investigated to study their biocompatibility and antibacterial properties. This study is based on findings that ALD films formed at different temperatures tend to have a different roughness [129], [175], [176]. Further, hafnia exhibits a change in crystallinity depending on the temperature [129], which could affect the interaction with living cells and bacteria [71], [177]. Therefore, SEM investigation on the surface and GI-XRD (Section 2.4) were used as supportive techniques to determine the surface morphology and crystallinity of thin films.

ALD procedures for 60 nm thick alumina and hafnia thin films were used for deposition, as in studies 3.2 and 3.3, but given a significantly higher temperature, i.e. 260 °C, thicknesses can vary by several nanometers. However, the thicknesses of the thin films here are not a significant parameter as the investigation is focused exclusively on the surface.

3.4.1 Surface morphology and crystallinity

The surface morphologies of cp-Ti and SS316L specimens coated with ALD alumina thin films deposited at different temperatures, 180 °C and 260 °C, are shown in **Fig. 3.38**. The presence of agglomerates, order of magnitude of 1 µm, randomly distributed over the surface can be observed in all four cases. For the SS316L substrate, these agglomerates appear to form preferentially in some areas, i.e. they are not uniformly distributed (**Fig. 3.38 c,d**). On cp-Ti samples, the agglomerates have an equally random distribution on the surface (**Fig. 3.38 a,b**). In the case of alumina thin films, the deposition temperature

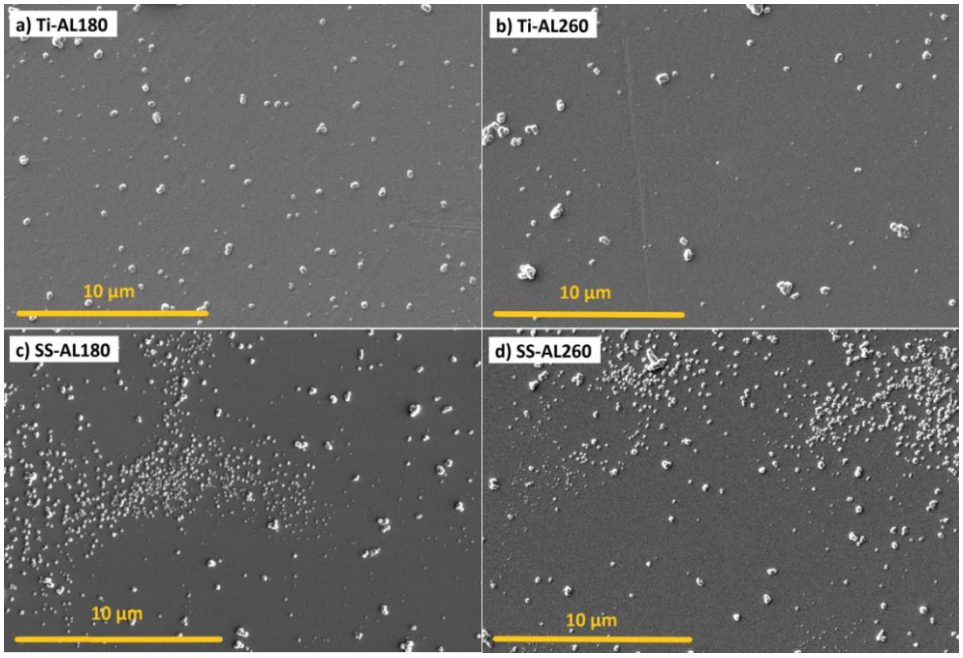

Figure 3.38: SEM images of ALD alumina-coated cp-Ti and SS316L specimens for **a)** cp-Ti coated at 180 °C, **b)** cp-Ti coated at 260 °C, **c)** SS316L coated at 180 °C and **d)** SS316L coated at 260°C.

does not affect the change in the formation of agglomerates, i.e. at both temperatures, the morphology and, therefore, micro-roughness are equal. EDXS analyses found that these agglomerates, especially the bigger ones, may be associated with the presence of Si on the surface of specimens left after polishing. Although, it was also found that these agglomerates may be formed without Si under the film, i.e. probably on surface imperfections, as stated in Section 3.3. An example of EDXS analysis on such agglomerate is shown for Ti-AL180 thin film in **Fig 3.39** and **Table 3.8**, where Si is detected in low proportion.

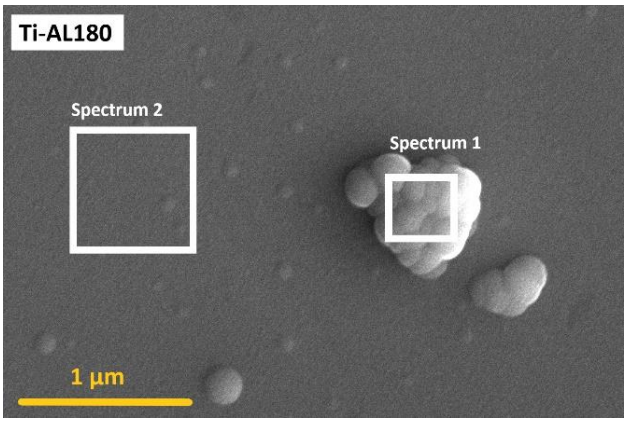

Figure 3.39: SEM image of alumina thin film deposited on cp-Ti specimen at 180 °C with EDXS analysis at agglomerate.

Table 3.8: Results of EDXS analysis on agglomerate on alumina film deposited on cp-Ti specimen at 180 °C (**Fig. 3.39**).

Element	Spectrum 1	Spectrum 2
O (at %)	57.6	43.8
Ti (at %)	26.6	48.0
Al (at %)	13.9	8.2
Si (at %)	1.9	-
Total	100.0	100.0

ALD hafnia thin films exhibit different surface morphology than alumina films. Namely, the presence of agglomerates depends strongly on the deposition temperature (**Fig. 3.40**). When deposited at 180 °C, the surface of the hafnia thin films appears uniform on a given scale (**Fig. 3.40 a,c**), while when deposited at 260 °C, many agglomerates, order of magnitude of 1 µm, are present (**Fig. 3.40 b,d**). These agglomerates result from the Si presence, as in the case of alumina, though it seems that hafnia is prone to form agglomerates itself more than alumina, as has also been found in Sections 3.1 and 3.2. Further, the rough morphology on the nano-scale is the characteristic feature of the ALD hafnia thin films (insets in **Fig. 3.40**), as has also been shown in study 3.1. These tiny agglomerates, less than 100 nm in size, are intrinsic properties of the ALD hafnia thin films, i.e., the nature of the deposit growth depends on the temperature. At higher temperatures, a higher density of these agglomerates can be observed (insets in **Fig. 3.40 b,d**) compared to the morphology at lower temperatures (insets in **Fig. 3.40 a,c**).

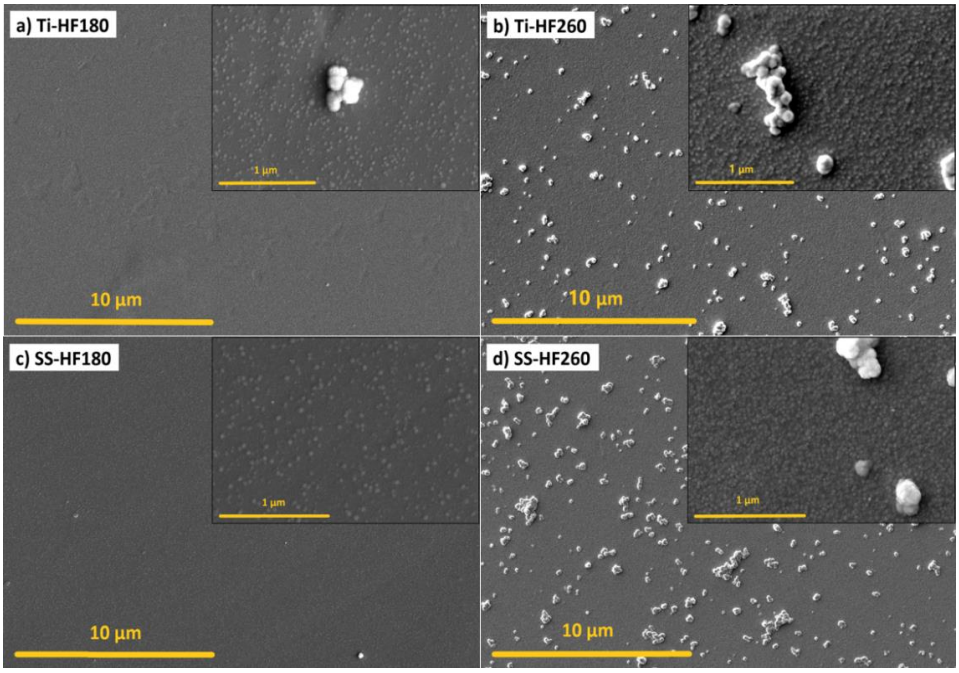

Figure 3.40: SEM images of ALD hafnia-coated cp-Ti and SS316L specimens for **a)** cp-Ti coated at 180 °C, **b)** cp-Ti coated at 260 °C, **c)** SS316L coated at 180 °C, and **d)** SS316L coated at 260°C.

Regarding the crystallinity in alumina thin films, GI-XRD measurements showed that alumina is entirely amorphous, and there is no difference in crystallinity regardless the deposition temperatures (**Fig. 3.41 a**). Here, only peaks for Ti can be detected because, despite very low angles, i.e. grazing incidence mode (Section 2.4), these films are too thin to avoid the signal from the substrate.

On the other hand, hafnia thin films showed more interesting characteristics in terms of crystallinity. At a deposition temperature of 180 °C, the XRD spectrum shows a broad feature in the range of 25° to 40° of 2Θ values where peaks for crystalline hafnia are expected (**Fig. 3.41 b**), indicating an amorphous structure [130], [178]. However, after the TEM analysis, it was found that crystallites were present in the film (**Fig. 3.42 a**), i.e.

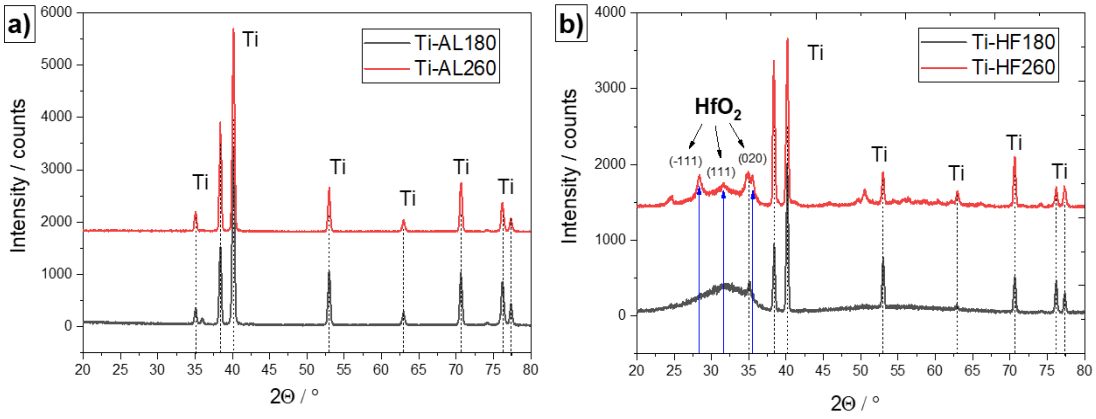

Figure 3.41: GI-XRD spectra of **a)** alumina thin films deposited at 180 °C and 260 °C, on cp-Ti substrate and **b)** hafnia thin films deposited at 180 °C and 260 °C, on cp-Ti substrate.

that the film was not completely amorphous. The picture clearly shows the crystal structure of the marked crystallite, which has a conical shape on the film's surface. But since GIXRD did not detect the presence of the crystalline phase in the film, it can be assumed that the proportion of crystalline phase is very low for the hafnia deposited at 180 °C. However, after the deposition at 260 °C, hafnia shows a significantly higher proportion of crystallinity, as it is shown in **Fig. 3.41 b**. Reflections for (-111), (111) and (020) crystal planes are observed, similarly as reported here [178]. By integrating the XRD spectrum surface and the crystal phase-related peaks in the film, it is possible to estimate the proportion of the crystal phase in the hafnia thin film. It was estimated that the crystallinity content is ca. 10%, and the estimation procedure is described in Appendix C. After TEM analysis of this film, it was found that almost all large agglomerates are due to the formation of the crystalline phase during deposition, and the example shown in **Fig. 3.42 b**. Also, it should be noted that both crystallites shown in **Fig. 3.42** are formed accidentally (due to local conditions during deposition), i.e. not on surface irregularities, as it can be seen that the interface is non-defective.

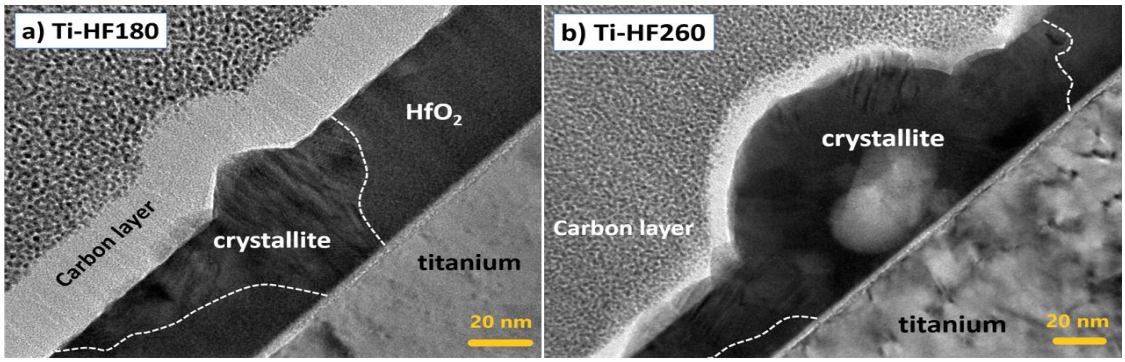

Figure 3.42: TEM analyses showing crystallites of **a)** hafnia deposited on cp-Ti at 180 °C and **b)** hafnia deposited on cp-Ti at 260 °C.

3.4.2 Biocompatibility properties

The first method to evaluate biocompatibility was by incubating specimens in a medium and obtaining their extracts, as described in Section 2.5.1. By using extracts to cultivate human mesenchymal stem cells (hMSCs), it is possible to infer the possible toxicity of the tested ALD thin films for cell development. More precisely, to obtain data on whether the tested ALD thin films release toxic species that would interfere with the metabolic activity of cells and their development. If the specimens do not show a harmful effect, they can be considered materials of potentially good biocompatibility.

The results of epifluorescence microscopy, where cell development can be seen after 3 days of culturing in the extracts of the tested specimens and the control media, are shown in **Fig. 3.43**. Blue spots and flecks represent cell nuclei, while grey fibre-like forms represent cytoskeletal filamentous actin (F-actin) that indicates cellular development. First of all, in the control medium (**Fig. 3.43 a**) containing only fresh culture medium without specimens extracts, certain cell development is observed, which serves as a reference. In the case of positive control (**Fig. 3.43 b**), a culture medium with added Triton X-100, cell development is completely stopped, and only inactive cell nuclei can be observed. However, a comparison of cell development for the tested specimens (**Fig. 3.43 c-l**) and control medium (**Fig. 3.43 a**) did not show a significant difference in the development of F-actin. Thus, none of the tested specimens show the release of harmful species during incubation

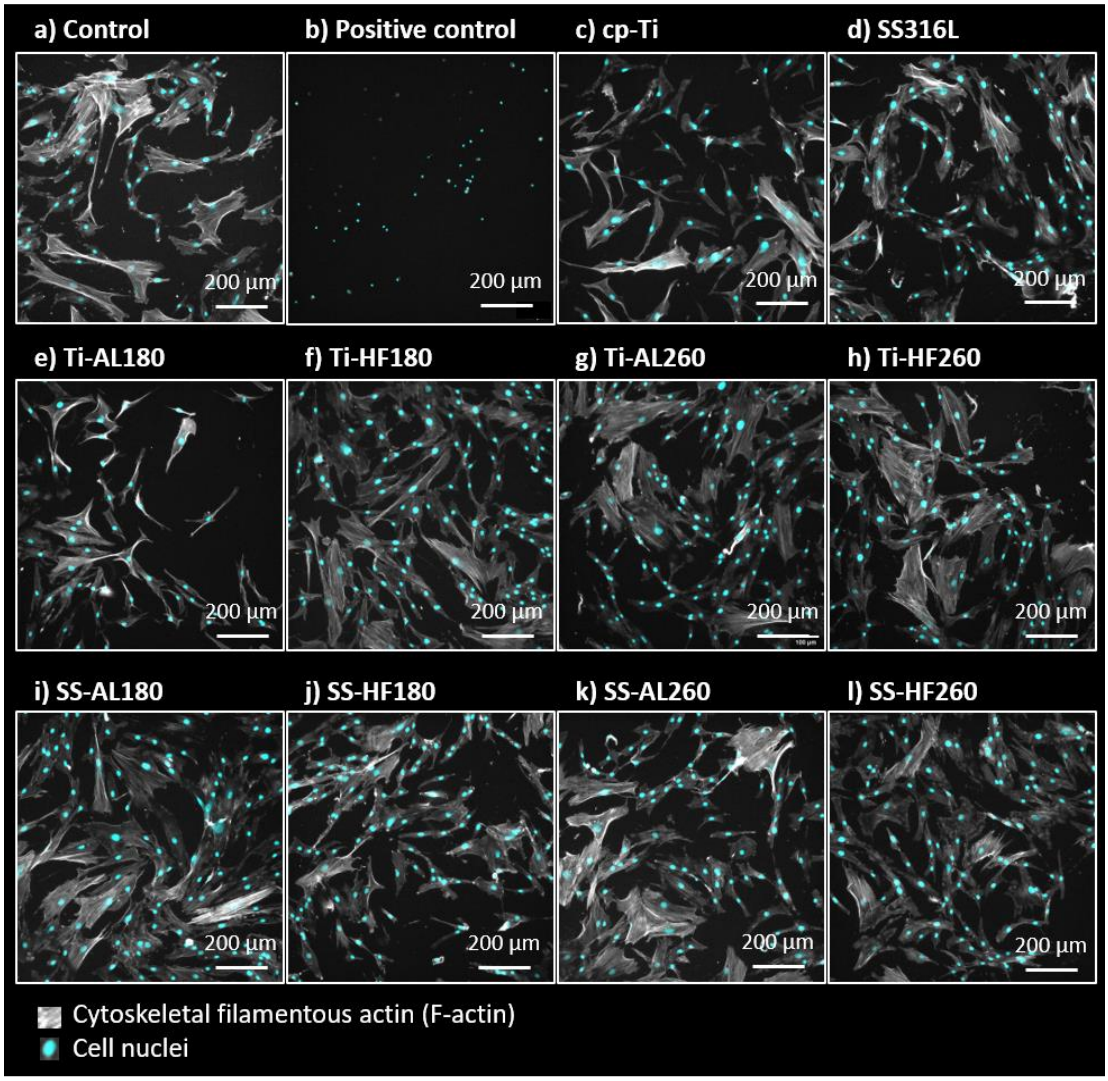

Figure 3.43: Fluorescent labelling of F-actin (grey) and nuclei (blue) of hMSCs cultured for 3 days in extracts of tested specimens and in control media; **a)** control containing fresh culture medium, **b)** positive control or culture medium with added Triton X-100, **c)** cp-Ti extract, **d)** SS316L extract, **e)** Ti-AL180 extract, **f)** Ti-HF180 extract, **g)** Ti-AL260 extract, **h)** Ti-HF260 extract, **i)** SS-AL180 extract, **j)** SS-HF180 extract, **k)** SS-AL260 extract and **l)** SS-HF260 extract.

that would interfere with cell development, i.e. they all have potentially good biocompatibility.

The second, more quantitative method for testing the metabolic activity of cells cultured in the extracts of specimens is performed using Resazurin assay and fluorescence spectroscopy (Section 2.5.1). The metabolic activity of cells after culturing in extracts of specimens and control media after 24 h, 48 h and 72 h are shown in **Fig. 3.44**. Here, as in the previous case, the metabolic activity of the cells in the control medium is similar or the same as for the tested specimens. The Resazurin assay confirmed the inertness of the tested specimens, in terms of non-release of harmful species into the incubation medium. However, the somewhat higher metabolic activity of the cells was observed for SS316L and SS-AL180 extracts after 72 h, but there is no reasonable explanation for this as it is even higher than the metabolic activity in the control medium.

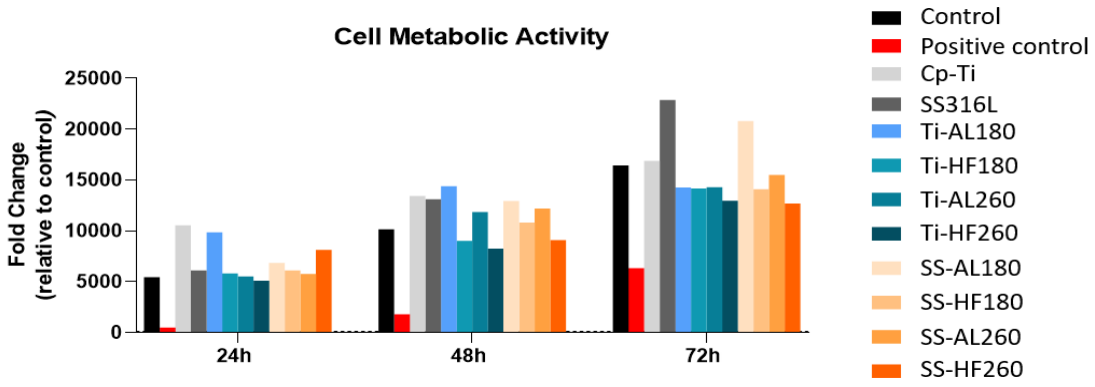

Figure 3.44: Results of Resazurin assays showing hMSCs viability after culturing in specimen extracts and control media for 24 h, 48 h and 72 h.

Another way to perform biocompatibility assays was by direct contact or seeding of cells on the surfaces of the tested specimens and by performing the same methods of epifluorescence microscopy and Resazurin assays. The results of cell development after 7 days of culturing directly on the surfaces of the tested specimens using epifluorescence microscopy are shown in **Fig. 3.45**. There was no significant difference in the cell appearance between the specimens. The main result is that in the case of Ti-HF180 and SS-HF180, the presence of cells was not observed, so they are not shown here. There is an interesting correlation with the morphological characteristics of the surfaces. Namely, ALD hafnia thin films deposited at 180 °C do not show roughness or agglomerates on the micrometer scale (**Fig. 3.40 a,c**) as hafnia deposited at 260 °C (**Fig. 3.40 b,d**). Thus, the absence of cells on the surface is not caused by the toxic action of the species from the surface; otherwise, it would be detected in assays performed from extracts as well. Instead, the reason lies in the unfavorable morphology of agglomerate-free surfaces.

The Resazurin assays were performed after 1 and 7 days of culturing of cells on the specimen surfaces (Section 2.5.1), and the results are shown in **Fig. 3.46**. Again, the metabolic activity of cells in the case of Ti-HF180 and SS-HF180 is severely impaired, confirming that uniform morphology of these ALD thin films (**Fig. 3.40**) is unfavorable for cell development. The remaining specimens, which show a significant presence of agglomerates on the surface, all have favorable properties for cell development. The comparison of the metabolic activity of cells on uncoated specimens, cp-Ti and SS316L, and on ALD thin films shows that it is somewhat increased after 7 days of culturing for ALD thin films deposited at 260 °C, regardless of the used substrate. This is related to the appearance of agglomerates on the surface of ALD thin films, which was shown to occur mainly at higher deposition temperatures (**Figs. 3.38 and 3.40**). Further, when comparing the uncoated specimens, i.e. cp-Ti and SS316L, it is interesting to note that the metabolic activity for SS316L increases significantly over time, while for cp-Ti, this increase is slower. Namely, after 1 day of culturing (**Fig. 3.46 a**), the metabolic activity of cells is significantly higher for cp-Ti, and after 7 days (**Fig. 3.46 b**), both specimens show almost the same level of that, i.e. it is fast increased for SS316L.

Based on the presented results, it can be concluded that alumina and hafnia ALD thin films and uncoated cp-Ti and SS316L specimens do not have a detrimental or toxic effect on cell development. However, surface morphology, i.e. agglomerate distribution and their size, may have a decisive effect on cell adhesion or attachment, and consequently cellular development over the surface.

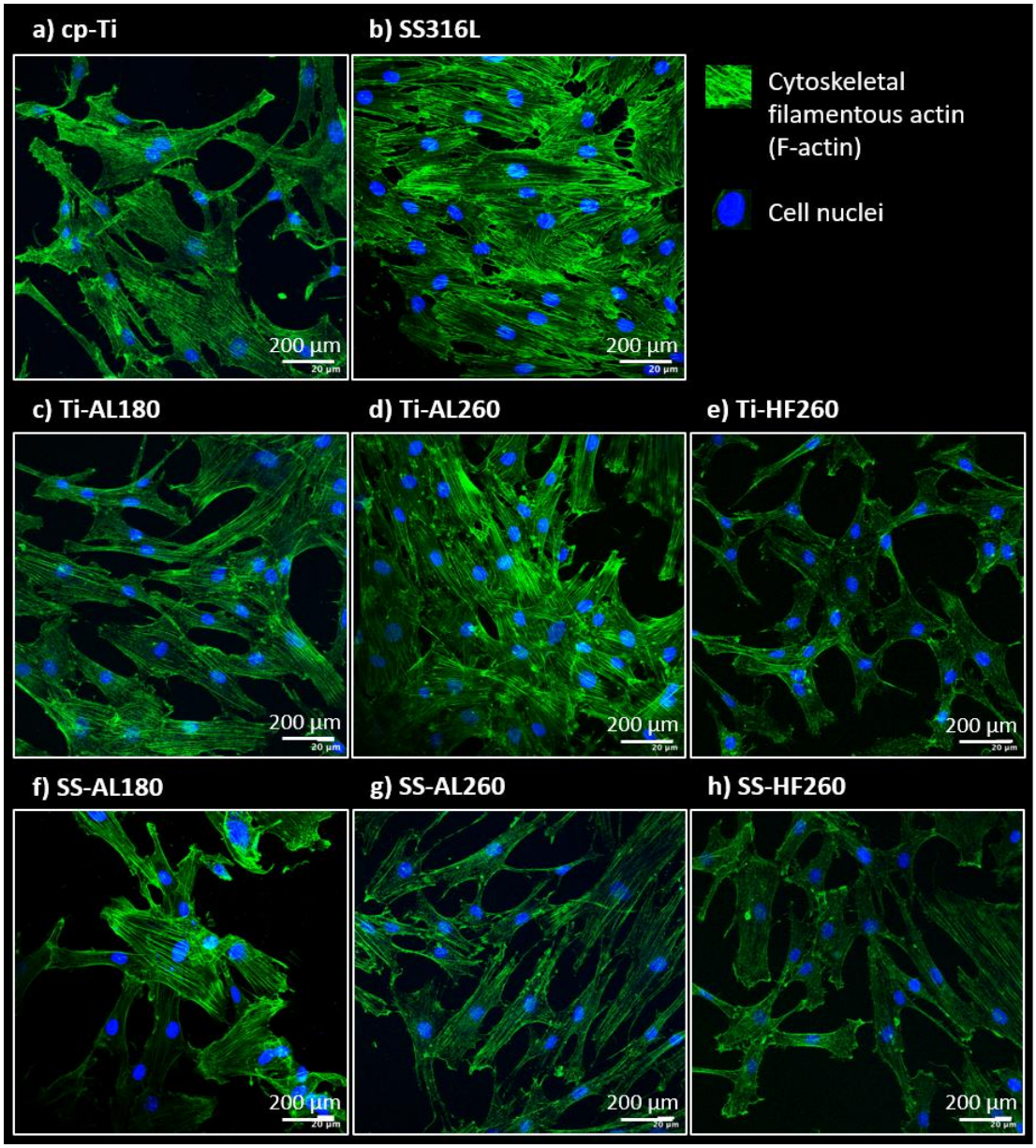

Figure 3.45: Fluorescent labelling of F-actin (green) and nuclei (blue) of hMSCs cells cultured for 7 days direct on tested specimens; **a)** cp-Ti specimen, **b)** SS316L specimen, **c)** Ti-AL180 specimen, **d)** Ti-AL260 specimen, **e)** Ti-HF260 specimen, **f)** SS-AL180 specimen, **g)** SS-AL260 specimen, and **h)** SS-HF260 specimen.

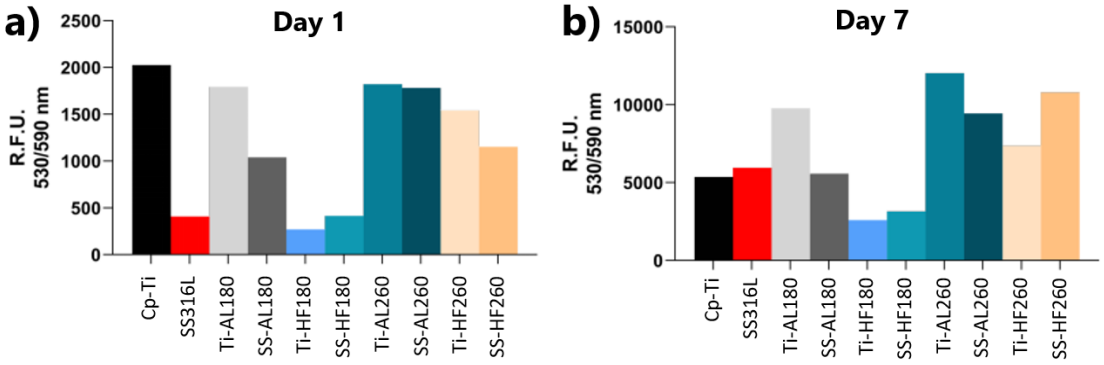

Figure 3.46: Results of Resazurin assays showing hMSCs viability after culturing directly on the specimen surfaces after **a)** 1 day and **b)** 7 days.

3.4.3 Antibacterial properties

Antibacterial properties were determined by direct contact of *Staphylococcus aureus* bacteria and the specimen surfaces (Section 2.5.1.). A colony-forming unit (CFU) was counted in the supernatant incubation medium and of adhered bacteria on the specimen surfaces. In addition to cp-Ti and SS316L specimens, pure Cu was used as a bactericide, i.e. as a positive control. Additionally, SEM surface observations were performed for visual insight into adhered bacteria.

The antibacterial activity of bare cp-Ti and coated cp-Ti specimens compared to the Cu specimen in supernatant media and of adhered bacteria on the specimen surfaces are shown in **Fig. 3.47**. On the Cu specimen, no live bacteria were present either in the supernatant media or as adhered to the surface. On bare cp-Ti, significantly more bacteria remained on the specimen surface, i.e. adhered (**Fig. 3.47 b**), than in the supernatant medium (**Fig. 3.47 a**). Among ALD-coated specimens, Ti-AL260 shows an anti-adhesive effect, as demonstrated by the statistically significant differences observed for supernatants and adherent bacteria. The Ti-AL180 specimen does not show a similar effect, although both alumina-coated cp-Ti specimens have a similar morphology, i.e. the presence of

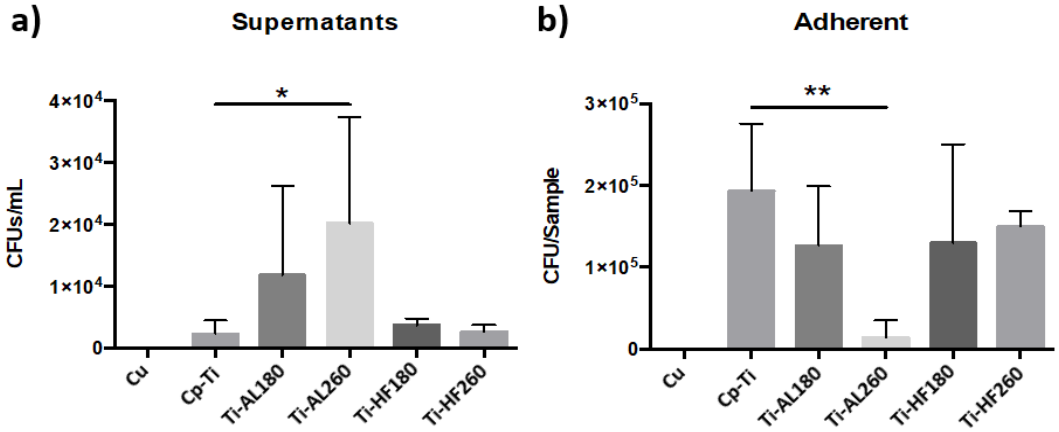

Figure 3.47: Antibacterial activity of cp-Ti and cp-Ti-coated surfaces against *S. aureus* after incubation for 2h. Statistically significant differences are indicated as *p< 0.05; **p<0.01.

agglomerates (**Fig. 3.38 a,b**). Both hafnia-coated cp-Ti specimens, Ti-HF180 and Ti-HF260, show similar features as bare cp-Ti in contact with bacteria, i.e. the presence of adhered bacteria on the surface and significantly less supernatant's bacteria. Since Ti-HF180 and Ti-HF260 have pretty different surface morphology (**Fig. 3.40 a,b**), it turns out that surface morphology and presence of agglomerates do not affect the attachment of these bacteria on hafnia thin films.

The antibacterial activity of the SS316L specimens proved to be quite similar to that of cp-Ti (**Fig. 3.48**), except for SS-AL260. Namely, it would be expected that the SS-AL260 has similar anti-adhesive properties as the Ti-AL260 (**Fig. 3.47 b**), but this is not the case. SS-AL260 film does not provide a better anti-adhesive surface than bare SS316L (**Fig. 3.48 b**). This may correlate with the different surface morphology of the alumina film deposited at 260 °C on cp-Ti and on SS316L specimens (**Fig. 3.38 b,d**) or possibly with the different surface energy (not measured in this work). Bare SS316L showed similar interactions with bacteria as cp-Ti, i.e. more bacteria remained adhered to the surface than in the supernatant media. In the case of hafnia-coated SS316L specimens, both SS-HF180 and SS-HF260 show the same properties as in the case of cp-Ti specimens and as bare SS316L, i.e. preferred adhesion of bacteria to their surfaces.

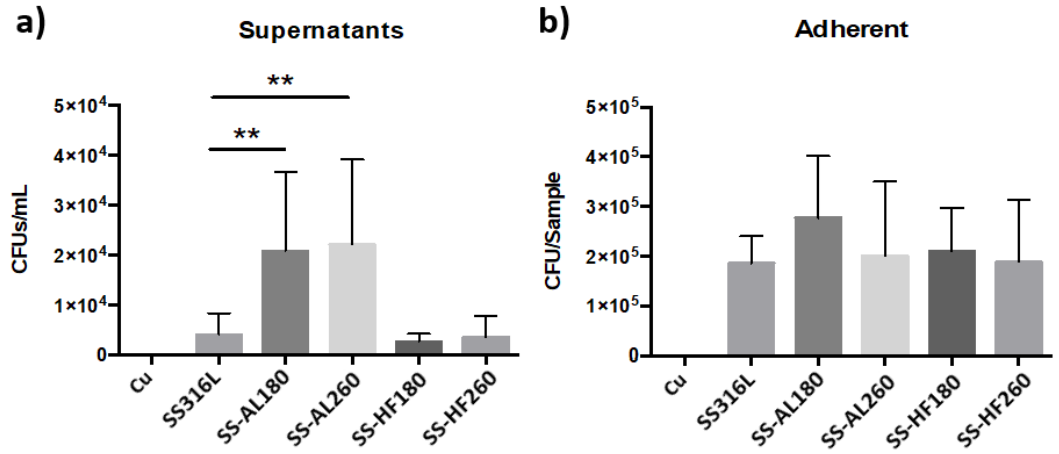

Figure 3.48: Antibacterial activity of SS316L and SS316L-coated surfaces against *S. aureus* after incubation for 2h. Statistically significant differences are indicated as **p<0.01.

For the visual illustration of the adhesion of bacterial colonies on the specimen surfaces, cp-Ti specimens coated with ALD thin films and exposed to bacteria are shown in **Fig. 3.49**. *S. aureus* is a round-shaped bacteria that usually forms in clumps as bright white clusters in different amounts for all four cases here, and an example is shown in the inset in **Fig 3.48 d**. Regardless of the similar morphology of Ti-AL180 and Ti-AL260 specimens regarding agglomerates (**Fig. 3.38 a,b**), visually fewer bacteria can be observed on the surface of Ti-AL260 (**Fig. 3.49 a,b**). The same was also concluded by CFU counting **(Fig. 3.47**), i.e. that Ti-AL260 surface provides anti-adhesive effect for these bacteria.

On the other hand, Ti-HF180 and Ti-HF260, despite a significant difference in morphology (**Fig. 3.40 a,b**), i.e. the absence of agglomerates in Ti-HF180, the presence of bacteria was observed in both cases equally (**Fig. 3.49 c,d**). However, it should be noted that SEM results are only complementary results for visual information and should not be taken as quantitative. In the quantitative measurements by CFU counting, the bacteria are live, while in the case of the SEM observation, due to the specimen preparation process (Section 2.5.2), all bacteria are dead.

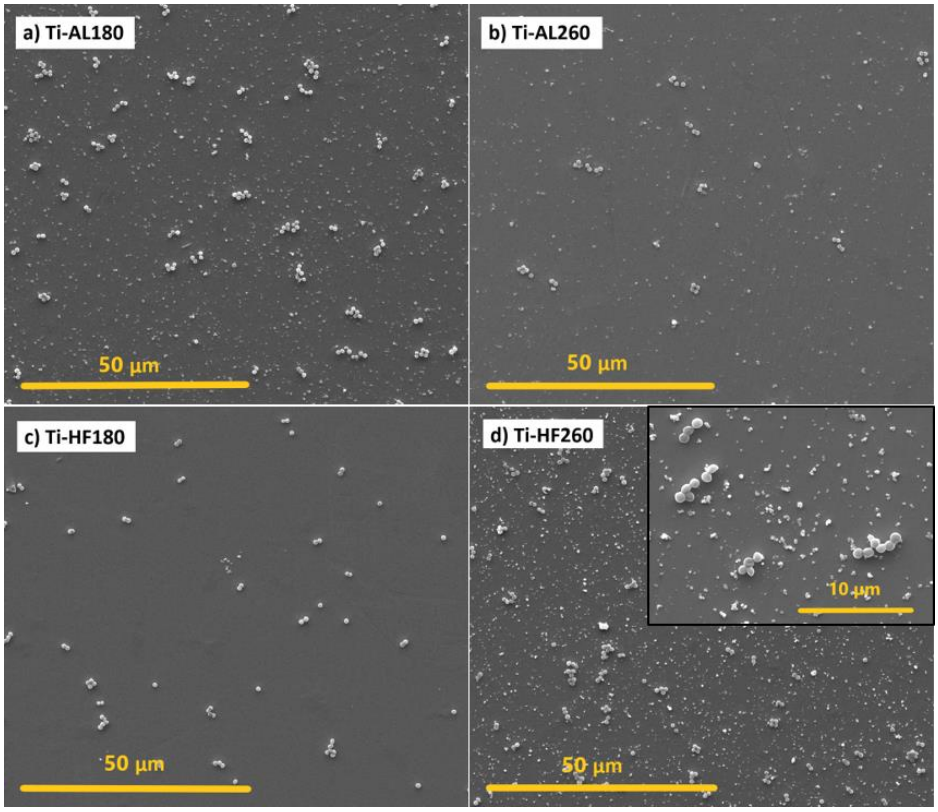

Figure 3.49: SEM images of ALD alumina- and hafnia-coated cp-Ti specimens after incubation for 2 h with the *S. aureus* for **a)** alumina deposited at 180 °C, **b)** alumina deposited at 260 °C, **c)** hafnia deposited at 180 °C and **d)** hafnia deposited on 260°C. White bright clusters are adhered bacteria.

3.4.4 Summary

The deposition temperature does not affect the surface morphology of alumina thin films, i.e. the size and distribution of agglomerates. However, the effect of temperature is significant for hafnia thin films, i.e. at 180 °C, the surface looks very uniform, while at 260 °C, there are many agglomerates sized approximately 1 µm. Further, the deposition temperature does not affect the crystallinity of the alumina thin film, which was completely amorphous. Hafnia the thin film deposited at 260 °C showed a crystalline content of about 10%, and that at 180 °C did not show the presence of a crystalline phase.

Both thin films, alumina and hafnia, regardless of the deposition temperature, showed no toxic effect on mesenchymal stem cells nor a bactericidal effect on *S. aureus*, and the same has been shown for uncoated cp-Ti and SS316L specimens. However, the presence and distribution of agglomerates proved to be a decisive factor for good adhesion and retention of cells on the surface, while it did not show the same effect on bacteria.

Yet the antibacterial properties were shown exclusively for alumina thin film deposited on cp-Ti at 260 °C, and it was concluded that due to the specific surface chemistry, probably increased surface energy, it has only an adhesive effect on bacteria.

3.5 Conclusions

3.5.1 Study 3.1 – The effect of cp-Ti surface preparation on the protective properties of ALD Al_2O_3 and HfO_2 films

Considering the first hypothesis of the thesis, i.e. the smooth surface of cp-Ti substrate allows the formation of higher quality alumina and hafnia ALD thin films (in terms of surface protection and barrier properties) than the rough surface, it is proved correct.

Both types of surfaces, rough and smooth, allow uniform deposition and complete coverage with both types of films, alumina and hafnia. According to PDP tests, both ALD thin films vastly reduce the corrosion current density of both ground and polished specimens. This would not be possible in the case of non-uniform ALD films. Yet alumina and hafnia showed slightly different properties. At the beginning of testing, alumina provides similar corrosion protection on rough and smooth surfaces, while hafnia showed differences in the degree of protection depending on the surface roughness. Therefore, the protective properties of hafnia are more affected by the surface roughness.

Long-term EIS measurements during 40 days of immersion in Hanks' solution at 37 °C provided further detail on the stability of films over a long period in simulated human body conditions. Both thin films exhibit a high capacitive character, with a broad region of linear increase in the impedance magnitude and large phase angle values. Alumina film on a smooth surface showed excellent stability throughout the whole immersion time, while on a rough surface, it showed a slight weakening in protective properties after 15 days. However, hafnia showed a significant difference in properties on a smooth and rough surface. On a smooth surface, it shows exceptional insulating properties continuously throughout the 40 days, while on a rough surface, it shows significant porosity resulting in passivation of cp-Ti through the pores of the film. It can be assumed that crystallites are easily formed on a rough surface due to the abundance of defects, and at their grain boundaries, the penetration of electrolytes to the substrate can easily occur.

3.5.2 Study 3.2 – The effect of thickness of Al_2O_3 ALD films deposited on cp-Ti and SS316L on their protective properties

In the second hypothesis, it was postulated that the thickness of ALD thin film is critical for providing barrier corrosion protection. Long-term electrochemical response confirmed that this hypothesis was correct.

Electrochemical measurements on thinner alumina films, of *ca.* 60 nm and 20 nm, on cp-Ti and SS316L as substrates have shown that both ALD alumina thin films provide significant barrier protection reflected in significantly reduced current densities. However, after a few days of immersion, 20 nm thick alumina film failed, and it was unstable and susceptible to dissolution in Hanks' solution at 37 °C, probably due to its insufficient thickness. The instability of thin films has been observed mainly for cp-Ti and less for the SS316L substrate indicating a difference in the protective properties of very thin alumina film when deposited on different substrates.

On the other hand, 60 nm thick film has retained good barrier properties over the immersion period on both substrate types. Nevertheless, it was found that the repassivation of metal substrates plays an important role in assuring the protective properties of ALD thin films. Namely, the possibility of surface repassivation at high potentials indicates the presence of pores or defects in the film during anodizing of specimens. This behavior is especially evident for SS316L substrate due to its susceptibility to localized corrosion in chloride-containing solutions.

3.5.3 Study 3.3 – The effect of ALD multilayer structure Al_2O_3-HfO_2-Al_2O_3 deposited on cp-Ti and SS316L on their protective properties

The third hypothesis of the thesis was that the protective properties of multilayer ALD thin films, obtained by combining alumina and hafnia, are improved compared to a single layer of pure alumina ALD thin film of the same thickness, on both substrates, SS316L and cp-Ti. This hypothesis was refuted.

Multilayer thin films morphologically showed similar properties as single-layer alumina thin films, i.e. uniformity and no defects or cracks after deposition. However, the presence of hafnia as an interlayer seems to affect the structure of the thin film as more agglomerates that originate from hafnia have been observed than for single-layer alumina thin films.

Electrochemical measurements reveal that multilayer structure does not significantly improve protective properties compared to single-layer alumina film of the same thickness, as would be expected considering better dielectric properties of hafnia. After 1 hour of immersion in simulated physiological solution, multilayer thin films provide significant barrier protection of the underlying substrates equally as single-layer alumina film on both substrates.

After the long-term measurements of 30 days of immersion, multilayer thin film, equally as single-layer alumina thin film, retains good barrier properties as there is no increase in the current density values. A similar conclusion can be drawn from EIS tests. However, based on the reverse cycles of PDP curves tests at high potentials and SEM observations, it was concluded that there are significant differences in the protective properties of these films. Defects were detected in the multilayer thin film due to the hafnia middle layer and its tendency to form agglomerates during deposition. These defects enabled surface passivation and repassivation after the initiation of localized corrosion. However, in the case of the single-layer film, which is defect-free, sudden exposure of the substrate to high potentials resulted in progressed corrosion and relention of the film. This was observed only for SS316L specimens, similar to study 3.2, because cp-Ti is not susceptible to local corrosion under given conditions.

3.5.4 Study 3.4 – Biocompatibility and antibacterial properties of Al_2O_3 and HfO_2 ALD thin films deposited on cp-Ti and SS316L

The following hypothesis was postulated: alumina and hafnia ALD thin films have better biocompatibility and antibacterial properties than metal substrates SS316L and cp-Ti. Essentially, both hypotheses were refuted, with exception of only one thin film type where it has been proved correct.

Biocompatibility of the surfaces of ALD specimens seems to correlate significantly with the morphology of their surfaces on a micro scale, primarily with the presence of agglomerates, while antibacterial properties show no correlation with surface morphology. Otherwise, the favorable surface morphology of implant materials, i.e. roughness on micro and sub-micro scale, has previously been shown to be an essential property for good interaction between implanted material and tissue [177].

Regardless of the deposition temperature, ALD alumina and hafnia do not show a toxic effect on human mesenchymal stem cells nor a bactericidal effect on *S. aureus*. The same results were obtained for uncoated cp-Ti and SS316L specimens. Uniform ALD hafnia thin films deposited at 180 °C without agglomerates on the micro scale were shown to adversely affect cell adhesion and their development.

Bare cp-Ti and SS316L, and ALD thin films do not show antibacterial properties. However, they can show anti-adhesive properties to bacteria. The anti-adhesive effect may be due to increased surface energy conditioned by the presence of different chemical groups on the surface. This was the case for alumina thin film deposited on cp-Ti at 260 °C, as a significantly lower amount of adhered bacteria was shown compared to other surfaces. However, in the case of alumina thin film on SS316L at 260 °C, this was not the case. Therefore, the different nature of the substrate affects the growth and properties of ALD alumina thin films.

3.5.5 Towards ALD films application in biomedicine

Several points should be pointed out regarding the justification of applying ALD thin films on biomaterials for implantation. ALD thin films could offer an efficient solution for protecting cp-Ti and SS316L in some specific cases of high susceptibility of implanted biomaterials to corrosion. For instance, cp-Ti may be corroded when hydrogen peroxide is released around the implant site (see Section 1.3.2). ALD thin films could then offer a high level of protection by insulating the implant's surface from a dynamic biological environment. In addition, theoretically, it could be possible to use ALD thin films in implanted devices containing more metallic materials in contact, where there is a risk of galvanic corrosion (see Section 1.3).

On the other hand, SS316L, due to its sensitivity to localized corrosion, is an even better candidate for applying ALD films. From the corrosion point of view, the Cl ions are the most detrimental species for stainless steel since they can disrupt the passive film of SS316L and cause pitting corrosion [44]. Therefore, it seems that ALD films from various metal oxides could serve as adequate protection for some metallic materials or devices implanted into the human body. However, additional *in vitro* and *in vivo* studies need to be carried out, emphasizing long-term investigations to confirm or refute the safety and efficiency of different ALD films in the human body.

In addition, it is important to note that there are some limitations when considering the main characteristics of ALD thin films and their application in medicine. Namely, ALD thin films made of investigated ceramic materials, alumina and hafnia, may meet the requirements of chemical stability and biocompatibility, but their mechanical properties cause limited application. Since ALD thin films are mainly deposited as thin layers, up to several hundred nanometers, their mechanical stability in interaction with other parts of the implant or body is questionable. Therefore, research on ALD thin films for biomedical purposes should be mainly related to applications that do not involve a mechanical load that could damage the thin film, e.g. for bioassays, biosensors, nano-porous and nanostructured biomaterials for the specific application, bio-templating, etc. [91], [96].

Appendix A

Electrochemical Techniques in Corrosion

A.1 Introduction

Since the corrosion reactions in practice are primarily electrochemical, the corrosion behavior of metals can be evaluated with electrochemical techniques. The three techniques commonly used for assessing the corrosion properties of metallic materials are monitoring corrosion potential, potentiodynamic polarization test, and electrochemical impedance spectroscopy [34]. These techniques use a potentiostatic circuit that includes an electrochemical cell equipped with three electrodes, as schematically shown in **Fig. A.1** [179]. The working electrode (WE) is the metal specimen, i.e. material under evaluation. The counter electrode (CE), or auxiliary electrode, is ideally a material that supports oxidation or reduction processes with reactants in the electrolyte but does not itself undergo corrosion, e.g. platinum or graphite. The reference electrode (RE) has a stable and constant potential relative to which the potential of the WE is measured, e.g. saturated calomel electrode (SCE) or standard silver-silver chloride (Ag-AgCl) electrode [34], [179].

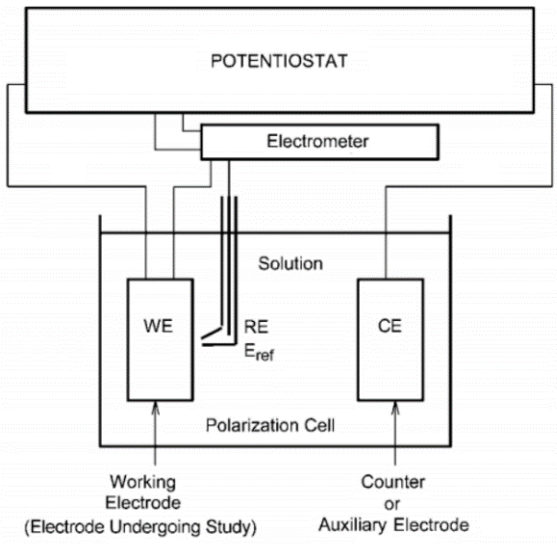

Figure A.1: Schematic illustration of potentiostatic circuit of a three-electrode electrochemical cell [179].

A.2 Potentiodynamic polarization test

In the potentiodynamic polarization (PDP) or linear sweep voltammetry (LSV) test, both cathodic and anodic reactions of the tested specimen are accelerated by applying overpotential from an external source. Usually, the initial potential is set in the cathodic range from the OCP, e.g., 200 mV, and then is increased over the OCP into the anodic region to a predetermined potential value or until the specimen corrodes. The applied overpotential on the specimen is changed at a constant rate, usually very slow, e.g. 1 mV/s, to keep the system in the steady state. During the application of the overpotential in both directions, the current of cathodic and anodic reactions is measured, which provides relevant information on the corrosion behavior of the specimen (**Fig. A.2**) [179].

It is also common to implement cyclic PDP to evaluate metal susceptibility to pitting corrosion. In this case, at high potentials, when an increase in current occurs due to pitting corrosion, the potential scan is reversed, whereby the metal surface may be re passivated or not. An example of a cyclic PDP curve is shown in **Fig. A.2** [3], [179]. The figure shows an example of a metal passivated in an electrolyte due to surface oxidation. Its OCP value is about −400 mV vs SHE (standard hydrogen electrode) [179]. As the potential in the anode direction increases, the current increases due to metal oxidation. The primary passivation potential (E_{pp}), the point of critical corrosion current (j_{cc}), is reached at the maximum current.

The passive film takes on a protective role so that there is a sudden decrease in current due to its insulating properties. Then, the current reaches the plateau, i.e. a constant value called the passivation current (j_{pas}). In the presence of aggressive ions, e.g. Cl^- and $[SO_4]^{2-}$, pitting or crevice corrosion or both are initiated and propagated at breakdown potential (E_b), along with oxygen evolution and electrochemical dissolution of the passive film. Since the current rises again due to corrosion (dashed curve), the reverse potential scan is applied in the vertex potential point (E_v). When the re passivation of the metal inside pits is

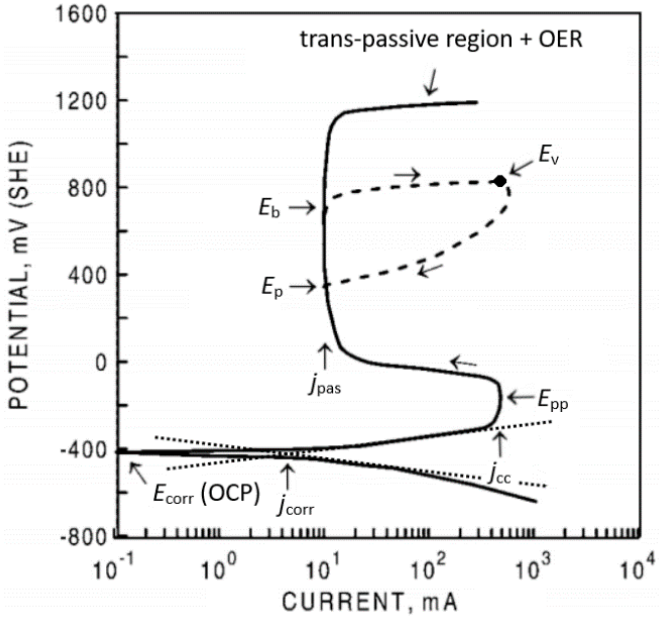

Figure A.2: Schematic illustration of potentiostatic circuit of a three-electrode electrochemical cell [179].

reached, the current drops again so that the dashed curve intersects the full line of the forward scan. This intersection point is named the pitting protection potential (E_p), which is considered the criterion for evaluating the material's susceptibility to pitting corrosion. If the potential never rises above this value, pitting is not expected to occur, i.e. the lower the resulting hysteresis loop, the lower the susceptibility of metal to pitting corrosion [3], [179].

In the case of some typical passivated metals, e.g. Fe, Cr, Ni, and in the absence of aggressive ions, metals can go into a trans-passive state where oxidation of a metal oxide to a higher oxidation state occurs. This process and OER are the reason for the increase in current in this area (**Fig. A.2**) [179]. However, for valve metals, e.g. Al, Ti, Zr, Hf, Ta, W, etc., the passive film can grow to a thickness of even several tens of micrometers, making OER difficult to occur [3].

The corrosion current density (j_{corr}), polarization resistance (R_p) and the corrosion rate are the values that are crucial for understanding corrosion of a particular metal. The corrosion rate is determined from the PDP curve using Tafel analysis (dot lines in **Fig. A.2**) in a narrow potential range around the OCP value [179], where the current linearly depends on the potential (50 to 100 mV from the OCP).

A.3 Electrochemical impedance spectroscopy

Electrochemical impedance spectroscopy (EIS) is a powerful tool in studying metals corrosion phenomena. Unlike the PDP technique, which uses only direct current (DC) and is destructive, EIS uses alternating current (AC) and can be considered non-destructive. This feature allows consecutive long-term tests of a metal specimen immersed in an electrolyte for the desired period.

The technique involves the application of time-varying and small potential perturbation in the cathodic and anodic direction around the OCP of the specimen. The alternating potential perturbation takes place at different rates or frequencies. In most cases, it is applied over the frequency range from 10^4 to 10^{-3} Hz, i.e. from fast to slow perturbations, while the amplitude of each potential perturbation is constant and commonly less than 10 mV. In this way, the corrosion system is not disturbed, i.e. a continuous in-situ measurement of the impedance behavior is enabled. The alternating potential perturbation is applied as a sinusoidal function, and as a result, the alternating current is measured (**Fig. A.3**) [179]. Both functions, dependence of potential and current on time, can be expressed according to **Eqs. A.1 and A.2**, respectively.

$$E(t) = E_0 \cdot \sin(\omega t) \tag{A.1}$$

$$i(t) = i_0 \cdot \sin(\omega t - \Phi) \tag{A.2}$$

where E_0 and i_0 are amplitudes in potential and current, respectively; ω is the radial frequency (rad/s) and is equal to 2πf (where f is the frequency in Hz), and Φ is phase angle or phase shift in arc degrees (°).

Fig. A.3 shows that the current is shifted by the value of Φ, i.e. the phase angle, which is obtained by analysis of the applied and the resulting sinusoidal signals. In addition to impedance, this quantity is used to describe the corrosion behavior of a tested metal. The impedance (Z) may be considered the resistance to alternating current, i.e. analogously to Ohm's law, $R = U / I$, it can be expressed as $Z = E / i$. However, since the division operation between sinusoidal functions is applied, imaginary numbers are included, and the

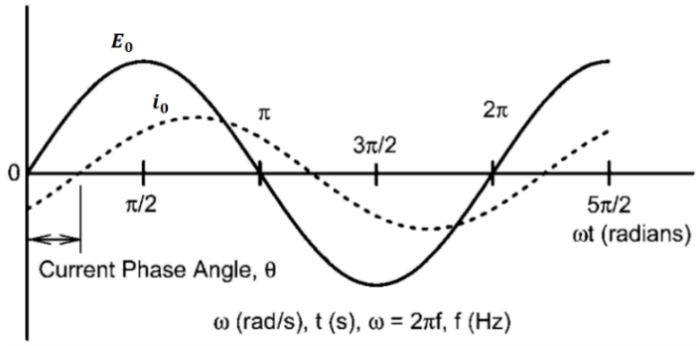

Figure A.3: The EIS technique uses the sinusoidal change of potential (full line) and the resulting change in alternating current (dash line).

total impedance is divided into a real component and an imaginary one. Therefore, the general mathematical equations for impedance are shown in **Eqs. A.3-A.6**.

$$Z = |Z| \cdot (\cos \Phi + j \sin \Phi) \tag{A.3}$$

$$Z_{Re} = |Z| \cos \Phi \tag{A.4}$$

$$Z_{Im} = |Z| \sin \Phi \tag{A.5}$$

$$Z = Z_{Re} + j\ Z_{Im} \tag{A.6}$$

where $|Z|$ is the so-called impedance magnitude and is equal to the ratio of E_0 and i_0, Z_{Re} is the real component, and Z_{Im} is the imaginary component of impedance.

The electrochemical cell is modelled by an equivalent electrical circuit (EEC), with each element corresponding to an electrochemical, chemical, or physical process taking place in the cell. The simplest EEC for metals immersed in an electrolyte is shown in **Fig. A.4**. R_p is the polarization resistance, and R_s is the solution resistance between the tested specimen and the reference electrode. The capacitance (C_dl) is associated with the specimen/electrolyte interface, i.e. it represents the double-layer capacitance formed upon

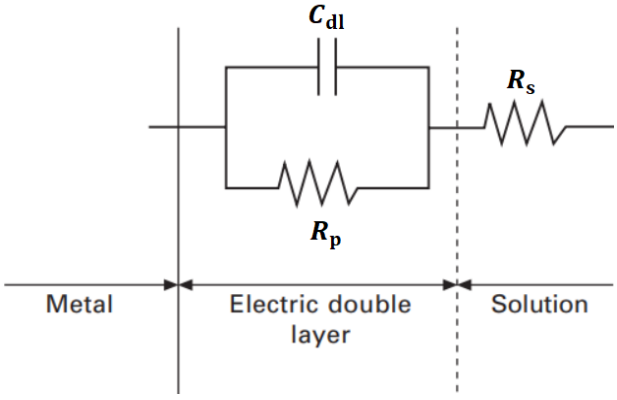

Figure A.4: Equivalent electric circuit of a metal/electrolyte interface.

immersion of metal in an electrolyte. The process of progressive corrosion is described specimen/electrolyte interface, i.e. it represents the double-layer capacitance formed upon immersion of metal in an electrolyte. The process of progressive corrosion is described with an inductive element, but this does not occur commonly in the case of medical materials and is not shown here.

As the frequency of applied potential varies, the final result may be presented as the dependence of impedance magnitude logarithm ($\log|Z|$) and phase angle on frequency logarithm in Hz (so-called Bode diagram in **Fig. A.5 a**) [179]. EIS data may also be plotted in the complex plane as Z_{Im} versus Z_{Re}, i.e. imaginary versus a real component (so-called Nyquist plot in **Fig. A.5 b**). Herein, it is possible to obtain a relationship between resistive, which is attributed to the real component, and capacitive behavior of the tested specimen, which is attributed to the imaginary component [179].

Bode plots have advantages in that the impedance magnitude and phase angle are shown as explicit functions of the frequency, which is the independent experimental variable. The Nyquist plot allows three relevant parameters to be determined directly, the resistance of solution (R_s), the polarization resistance (R_p), and capacity (C), which is calculated using the frequency at the apex of the semicircle as it is shown in **Fig. A.5 b** [179].

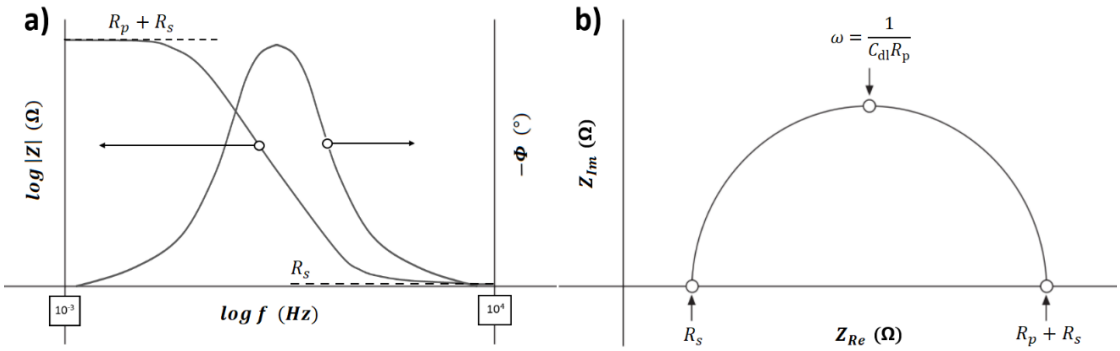

Figure A.5: Different EIS data presentations; **a)** Bode plot and **b)** Nyquist plot.

Appendix B

Morphology of the Hafnia Film

B.1 Source of Agglomerate in Hafnia Thin Film

Regarding the significant presence of agglomerates in hafnia film with a thickness of about 150 nm on cp-Ti (**Fig. 3.4 b**), the question arose whether agglomerates are exclusively the result of irregularities on the surface of the substrate.

Investigating the morphology of the hafnia film formed on the perfectly smooth surface of the Si-wafer, it is concluded that the formation of these agglomerates and crystallites can also be the property of the hafnia itself, as it has also been reported [129]. **Fig. B.1** presents the cross-section of the hafnia film of *ca.* 100 nm in thickness deposited on the Si-wafer, which is factory-coated with a layer of SiO_2 of *ca.* 500 nm in thickness. Since the surface of the SiO_2 substrate is perfectly smooth, there are no sites on the surface that could serve as a trigger for the formation of these agglomerates as in the case of the Ti-OPS surface. However, on the surface of the hafnia film, these agglomerates can be observed as bright areas to approximately the same extent as on the hafnia film formed on the cp-Ti substrate (**Fig. 3.4 b**).

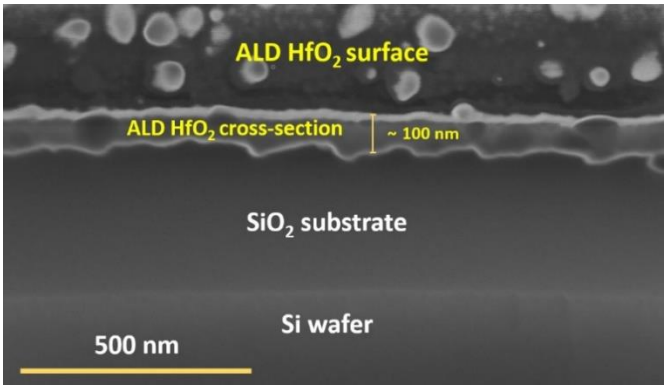

Figure B.1: SEM image of the hafnia ALD thin film deposited on the Si-wafer substrate on the cross-section site. Si-wafer is factory-coated with a SiO_2 layer of *ca.* 500 nm in thickness. Magnification was 100,000×, beam energy 5 kV and electrical current 50 pA.

It should be noted that the cross-section on the Si-wafer was not obtained by the FIB method but by a mechanically brittle fracture, and therefore the bright line representing the SiO_2/HfO_2 interface looks very curved. It is a perfectly smooth surface or interface on Si-wafer specimen, but because it was broken mechanically, it gives a false impression that the interface is rough.

B.2 Crystallinity in the HF260 Thin Film

Determination of the proportion of crystalline phase in the hafnia thin film deposited on cp-Ti at 260°C (Ti-HF260) was performed by integrating the XRD spectrum surface (**Fig. B.2 a**) and the HfO_2 crystal phase-related peaks in the film (**Fig. B.2 b**). From the obtained surface values, the content of the crystalline phase was estimated at about 10% (**Eq. B.1**).

$$x_c = \frac{A_c}{A} = \frac{832.8}{8384.9} = 0.1 \tag{B.1}$$

where, x_c is the portion of the crystal phase, A_c is the area formed by the three crystal phase-related peaks, and A is the area under the entire XRD spectrum.

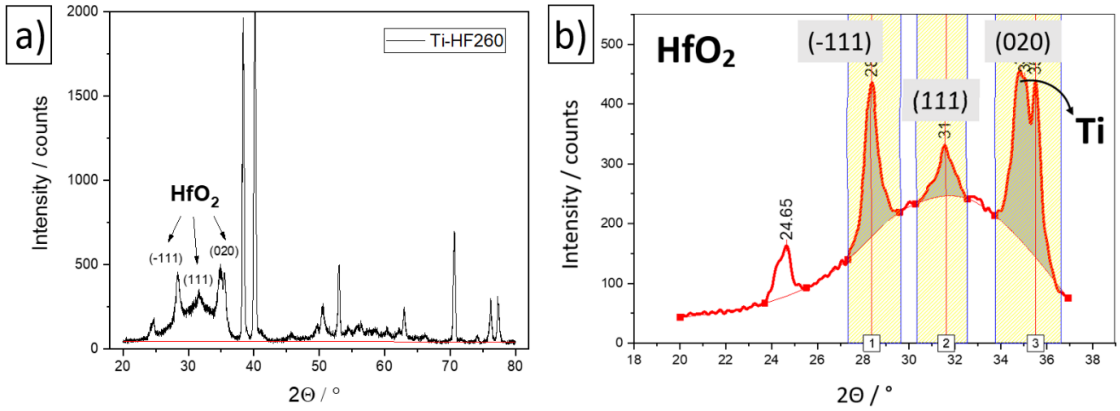

Figure B.2: SEM image of the hafnia ALD thin film deposited on the Si-wafer substrate on the cross-section site. Si-wafer is factory-coated with a SiO_2 layer of *ca.* 500 nm in thickness. Magnification was 100,000×, beam energy 5 kV and electrical current 50 pA.

However, it should be noted that the determination of the hafnia crystal phase content in this simple way can only serve as a rough estimate because, as shown in **Fig. B.2 b,** the peak for (020) crystal plane partially coincides with the peak for Ti at 2Θ on 35°. Thus, the obtained crystallinity estimate should be reduced, and it can be roughly assumed that the crystallinity content is between 5 and 10%.

References

[1] C. M. Agrawal, "Reconstructing the human body using biomaterials," *J. Miner.*, vol. 50, no. 1, pp. 31–35, 1998, doi: 10.1007/s11837-998-0064-5.

[2] D. F. Williams, *Definitions in biomaterials. Proceedings of a consensus conference of the european society for biomaterials*, vol. 4., 1987.

[3] N. Eliaz, "Corrosion of metallic biomaterials: A review," *Materials (Basel).*, vol. 12, no. 3, p. 1, 2019, doi: 10.3390/ma12030407.

[4] D. F. Williams, "On the nature of biomaterials," *Biomaterials*, vol. 30, no. 30, pp. 5897–5909, 2009, doi: 10.1016/j.biomaterials.2009.07.027.

[5] R. L. Reis, "2nd Consensus conference on definitions on biomaterials science," *J. Tissue Eng. Regen. Med.*, vol. 14, no. 4, pp. 561–562, 2020, doi: 10.1002/term.3016.

[6] I. Milošev, "Metallic materials for biomedical applications: Laboratory and clinical studies," *Pure Appl. Chem.*, vol. 83, no. 2, p. 309, 2011, doi: 10.1351/PAC-CON-10-07-09.

[7] R. I. M. Asri *et al.*, "Corrosion and surface modification on biocompatible metals: A review," *Mater. Sci. Eng. C*, vol. 77, p. 1261, 2017, doi: 10.1016/j.msec.2017.04.102.

[8] A. Guenbour, J. Faucheu, and A. Ben Bachir, "on the Mechanism for Improved Passivation By Addition of Molybdenum To Austenitic Stainless Steels in O-Phosphoric Acid.," *Corrosion*, vol. 44, no. 4, pp. 214–221, 1988, doi: 10.5006/1.3583928.

[9] C. S. Tedmon Jr., D. A. Vermilyea, and J. H. Rosolowski, "Intergranular corrosion of austenitic stainless steel," *J. Electrochem. Soc.*, vol. 118, p. 192, 1971, doi: 10.4028/www.scientific.net/AMM.229-231.14.

[10] J. Brnic *et al.*, "Mechanical properties, short time creep, and fatigue of an austenitic steel," *Materials (Basel).*, vol. 9, no. 4, pp. 1–19, 2016, doi: 10.3390/ma9040298.

[11] T. Hryniewicz and K. Rokosz, "Analysis of XPS results of AISI 316L SS electropolished and magnetoelectropolished at varying conditions," *Surf. Coatings Technol.*, vol. 204, no. 16–17, pp. 2583–2592, 2010, doi: 10.1016/j.surfcoat.2010.02.005.

[12] C. Pallotta, N. De Cristofano, R. C. Salvarezza, and A. J. Arvia, "The influence of temperature and the role of chromium in the passive layer in relation to pitting corrosion of 316 stainless steel in NaCl solution," *Electrochim. Acta*, vol. 31, no. 10, pp. 1265–1270, 1986, doi: 10.1016/0013-4686(86)80146-3.

[13] T. Hanawa, S. Hiromoto, A. Yamamoto, D. Kuroda, and K. Asami, "XPS characterization of the surface oxide film of 316L stainless steel samples that were located in quasi-biological environments," *Mater. Trans.*, vol. 43, no. 12, pp. 3088–3092, 2002, doi: 10.2320/matertrans.43.3088.

[14] M. Strangwood, "Fundamentals of ferrite formation in steels," *Phase Transform. Steels*, vol. 1, pp. 187–224, 2012, doi: 10.1533/9780857096104.2.187.

[15] H. Y. Ha, T. H. Lee, J. H. Bae, and D. W. Chun, "Molybdenum effects on pitting corrosion resistance of FeCrMnMoNC austenitic stainless steels," *Metals (Basel).*, vol. 8, no. 8, pp. 1–13, 2018, doi: 10.3390/met8080653.

[16] N. Suutala, "Effect of Manganese and Nitrogen on the Solidification Mode in Austenitic Stainless Steel Welds.," *Metall. Trans. A, Phys. Metall. Mater. Sci.*, vol. 13 A, no. 12, pp. 2121–2130, 1982, doi: 10.1007/BF02648382.

[17] T. Masumura and T. Tsuchiyama, "Effect of carbon and nitrogen on work-hardening behavior in metastable austenitic stainless steel," *ISIJ Int.*, vol. 61, no. 2, pp. 617–624, 2021, doi: 10.2355/isijinternational.ISIJINT-2020-535.

[18] J. W. Simmons, "Overview: High-nitrogen alloying of stainless steels," *Mater. Sci. Eng. A*, vol. 207, no. 2, pp. 159–169, 1996, doi: 10.1016/0921-5093(95)09991-3.

[19] D. M. Brunette, P. Tengvall, M. Textor, and P. Thomsen, "Titanium in Medicine," pp. 703–746, 2001, doi: 10.1007/978-3-642-56486-4_21.

[20] R. Boyer, G. Welsch, and E. W. Collings, *Materials properties handbook : titanium alloys.*, 1st ed., ASM Interantional, 1994, pp. 3–165.

[21] Y. M. Ahmed, K. Salleh, M. Sahari, M. Ishak, and B. A. Khidhir, "Titanium and its Alloy," *Int. J. Sci. Res.*, vol. 10, no. 3, pp. 1351–1361, 2014.

[22] N. Mitsuo, "Mechanical properties of biomedical titanium alloys," *Mater. Sci. Eng. A*, vol. 243, no. 1–2, pp. 231–236, 1998, doi: 10.1016/S0921-5093(97)00806-X.

[23] M. Niinomi, M. Nakai, and J. Hieda, "Development of new metallic alloys for biomedical applications," *Acta Biomater.*, vol. 8, no. 11, pp. 3888–3903, 2012, doi: 10.1016/j.actbio.2012.06.037.

[24] M. Topolovec, A. Cör, and I. Milošev, "Metal-on-metal vs. metal-on-polyethylene total hip arthroplasty tribological evaluation of retrieved components and periprosthetic tissue," *J. Mech. Behav. Biomed. Mater.*, vol. 34, pp. 243–252, 2014, doi: 10.1016/j.jmbbm.2014.02.018.

[25] M. Geetha, A. K. Singh, R. Asokamani, and A. K. Gogia, "Ti based biomaterials, the ultimate choice for orthopaedic implants - A review," *Prog. Mater. Sci.*, vol. 54, no. 3, pp. 397–425, 2009, doi: 10.1016/j.pmatsci.2008.06.004.

[26] J. L. Katz, "Anisotropy of Young's modulus of bone", *Nature*, vol. 288, pp. 106–107, 1980, doi: 10.1038/283106a0.

[27] M. A. Hussein, A. S. Mohammed, and N. Al-Aqeeli, "Wear characteristics of metallic biomaterials: A review," *Materials (Basel).*, vol. 8, no. 5, pp. 2749–2768, 2015, doi: 10.3390/ma8052749.

[28] K. Prasad *et al.*, "Metallic biomaterials: Current challenges and opportunities," *Materials (Basel).*, vol. 10, no. 8, pp. 1–33, 2017, doi: 10.3390/ma10080884.

[29] G. D. Rushing, M. J. Goretsky, T. Gustin, M. Morales, R. E. Kelly, and D. Nuss, "When it is not an infection: metal allergy after the Nuss procedure for repair of pectus excavatum," *J. Pediatr. Surg.*, vol. 42, no. 1, pp. 93–97, 2007, doi: 10.1016/j.jpedsurg.2006.09.056.

[30] V. Levašič, I. Milošev, and V. Zadnik, "Risk of cancer after primary total hip replacement: The influence of bearings, cementation and the material of the stem: A retrospective cohort study of 8,343 patients with 9 years average follow-up from Valdoltra Orthopaedic Hospital, Slovenia," *Acta Orthop.*, vol. 89, no. 2, pp. 234–239, 2018, doi: 10.1080/17453674.2018.1431854.

[31] I. Gurappa, "Characterization of different materials for corrosion resistance under simulated body fluid conditions," *Mater. Charact.*, vol. 49, no. 1, pp. 73–79, 2002, doi: 10.1016/S1044-5803(02)00320-0.

[32] J. Pan, D. Thierry, and C. Leygraf, "Hydrogen peroxide toward enhanced oxide growth on titanium in PBS solution: Blue coloration and clinical relevance," *J. Biomed. Mater. Res.*, vol. 30, no. 3, pp. 393–402, 1996, doi: 10.1002/(SICI)1097-4636(199603)30:3<393::AID-JBM14>3.0.CO;2-L.

[33] E. McCafferty, "Introduction of corroion science," 1st ed., Springer, 2010, pp. 1–518.

[34] S. Hiromoto, "Corrosion of metallic biomaterials," in Metals for Biomedical Devices, 1st ed., vol. 1. M. Niinomi, Woodhead Publishing, 2010, ch. 4, pp. 99–121, doi: 10.1533/9781845699246.2.99.

[35] G. Manivasagam, D. Dhinasekaran, and A. Rajamanickam, "Biomedical Implants: Corrosion and its Prevention - A Review," *Recent Patents Corros. Sci.*, vol. 2, no. 1, pp. 40–54, 2010, doi: 10.2174/1877610801002010040.

[36] B. Zhang *et al.*, "Unmasking chloride attack on the passive film of metals," *Nat. Commun.*, vol. 9, no. 1, pp. 1–9, 2018, doi: 10.1038/s41467-018-04942-x.

[37] S. Hiromoto and T. Hanawa, "Corrosion of Implant Metals in the Presence of Cells," *Corros. Rev.*, vol. 24, no. 5, pp. 323–351, 2011, doi: 10.1515/corrrev.2006.24.5-6.323.

[38] U. Kamachi Mudali, T. M. Sridhar, and R. A. J. Baldev, "Corrosion of bio implants," *Sadhana - Acad. Proc. Eng. Sci.*, vol. 28, no. 3–4, pp. 601–637, 2003, doi: 10.1007/BF02706450.

[39] S. Karimi and A. M. Alfantazi, "Ion release and surface oxide composition of AISI 316L, Co-28Cr-6Mo, and Ti-6Al-4V alloys immersed in human serum albumin solutions," *Mater. Sci. Eng. C*, vol. 40, p. 435–444, 2014, doi: 10.1016/j.msec.2014.04.007.

[40] E. Rahimi, R. Offoiach, K. Baert, H. Terryn, M. Lekka, and L. Fedrizzi, "Role of phosphate, calcium species and hydrogen peroxide on albumin protein adsorption on surface oxide of Ti6Al4V alloy," *Materialia*, vol. 15, p. 100988, 2021, doi: 10.1016/j.mtla.2020.100988.

[41] S. H. Chang and Y. C. Hsiao, "Surface and protein adsorption properties of 316L stainless steel modified with polycaprolactone film," *Polymers (Basel).*, vol. 9, no. 10, 2017, doi: 10.3390/polym9100545.

[42] T. Hanawa, "Reconstruction and Regeneration of Surface Oxide Film on Metallic Materials in Biological Environments," *Corros. Rev.*, vol. 21, no. 2–3, pp. 161–182, 2003, doi: 10.1515/CORRREV.2003.21.2-3.161.

[43] Y. Mu, T. Kobayashi, M. Sumita, A. Yamamoto, and T. Hanawa, "Metal ion release from titanium with active oxygen species generated by rat macrophages in vitro," *J. Biomed. Mater. Res.*, vol. 49, no. 2, pp. 238–243, 2000, doi: 10.1002/(SICI)1097-4636(200002)49:2<238::AID-JBM12>3.0.CO;2-J.

[44] Y. Koumya *et al.*, "Pitting corrosion behavior of SS-316L in simulated body fluid and electrochemically assisted deposition of hydroxyapatite coating," *Chem. Pap.*, vol. 75, no. 6, pp. 2667–2682, 2021, doi: 10.1007/s11696-021-01517-x.

[45] M. Sivakumar, K. S. Kumar Dhanadurai, S. Rajeswari, and V. Thulasiraman, "Failures in stainless steel orthopaedic implant devices: A survey," *J. Mater. Sci. Lett.*, vol. 14, no. 5, pp. 351–354, 1995, doi: 10.1007/BF00592147.

[46] H. Amel-Farzad, M. T. Peivandi, and S. M. R. Yusof-Sani, "In-body corrosion fatigue failure of a stainless steel orthopaedic implant with a rare collection of different damage mechanisms," *Eng. Fail. Anal.*, vol. 14, no. 7, pp. 1205–1217, 2007, doi: 10.1016/j.engfailanal.2006.11.037.

[47] H. Grafen, E.-M. Horn, H. Schlecker, and H. Schindler, "Corrosion," in *Ullmann's Encyclopedia of Industrial Chemistry*, Wiley-VCH Verlag GmbH & Co. KGaA, 2005, pp. 1–17.

[48] V. Maurice and P. Marcus, "Current developments of nanoscale insight into corrosion protection by passive oxide films," *Curr. Opin. Solid State Mater. Sci.*, vol. 22, no. 4, pp. 156–167, 2018, doi: 10.1016/j.cossms.2018.05.004.

[49] D. W. Shoesmith, J. J. Noël, and V. E. Annamalai, "Corrosion of Titanium and Its Alloys," in Reference Module in Materials Science and Materials Engineering, Elsevier, 2016, pp. 1–11, doi: 10.1016/b978-0-12-803581-8.09219-5.

[50] M. Nakagawa, S. Matsuya, K. U. Section, B. Engineering, O. Faculty, and D. Science, "Effect of Fluoride Concentration and pH on Corrosion Behavior of Titanium for Dental Use," *Dent. Mater. J.*, vol. 20, no. 4, pp. 305–314, 2001, doi: 10.1177/00220345990780091201.

[51] J. Pan, D. Thierry, and C. Leygraf, "Electrochemical and XPS studies of titanium for biomaterial applications with respect to the effect of hydrogen peroxide," *J. Biomed. Mater. Res.*, vol. 28, no. 1, pp. 113–122, 1994, doi: 10.1002/jbm.820280115.

[52] D. J. Blackwood, L. M. Peter, and D. E. Williams, "Stability and open circuit breakdown of the passive oxide film on titanium," *Electrochim. Acta*, vol. 33, no. 8, pp. 1143–1149, 1988, doi: 10.1016/0013-4686(88)80206-8.

[53] C. K. Dyer and J. S. L. Leach, "Reversible reactions within anodic oxide films on titanium electrodes," *Electrochim. Acta*, vol. 23, no. 12, pp. 1387–1394, 1978, doi: 10.1016/0013-4686(78)80022-X.

[54] S. Y. Yu, C. W. Brodrick, M. P. Ryan, and J. R. Scully, "Effects of Nb and Zr Alloying Additions on the Activation Behavior of Ti in Hydrochloric Acid," *J. Electrochem. Soc.*, vol. 146, no. 12, pp. 4429–4438, 1999, doi: 10.1149/1.1392655.

[55] D. Prando *et al.*, "Corrosion of titanium: Part 1: Aggressive environments and main forms of degradation," *J. Appl. Biomater. Funct. Mater.*, vol. 15, no. 4, pp. e291–e302, 2017, doi: 10.5301/jabfm.5000387.

[56] X. He, J. J. Noël, and D. W. Shoesmith, "Temperature Dependence of Crevice Corrosion Initiation on Titanium Grade-2," *J. Electrochem. Soc.*, vol. 149, no. 9, p. B440–B449, 2002, doi: 10.1149/1.1499501.

[57] R. L. Saldanha *et al.*, "Inhibition of the oxygen evolution reaction during titanium passivation in aqueous phosphoric acid solution," *J. Solid State Electrochem.*, vol. 24, no. 8, pp. 1991–1998, 2020, doi: 10.1007/s10008-020-04497-2.

[58] T. Hanawa, K. Asami, and K. Asaoka, "Repassivation of titanium and surface oxide film regenerated in simulated bioliquid," *J. Biomed. Mater. Res.*, vol. 40, no. 4, pp. 530–538, 1998, doi: 10.1002/(SICI)1097-4636(19980615)40:4<530::AID-JBM3>3.0.CO;2-G.

[59] T. Hanawa and M. Ota, "Calcium phosphate naturally formed on titanium in electrolyte solution," *Biomaterials*, vol. 12, no. 8, pp. 767–774, 1991, doi: 10.1016/0142-9612(91)90028-9.

[60] K. T. Kim, M. Y. Eo, T. T. H. Nguyen, and S. M. Kim, "General review of titanium toxicity," *Int. J. Implant Dent.*, vol. 5, no. 1, 2019, doi: 10.1186/s40729-019-0162-x.

[61] H. Zitter and H. Plenk, "The electrochemical behavior of metallic implant materials as an indicator of their biocompatibility," *J. Biomed. Mater. Res.*, vol. 21, no. 7, pp. 881–896, 1987, doi: 10.1002/jbm.820210705.

[62] A. G. Gristina, "Biomaterial-Centered Infections: Microbial Adhesion versus Tissue Integration," *Science*, vol. 237, no. 4822, pp. 1588–1595, 1987, doi: 10.1007/978-1-4471-3454-1_25.

[63] H. Breme, V. Biehl, N. Reger and E. Gawalt, "Metallic Biomaterials: Introduction," in Handbok of Biomaterial Properties, 2nd ed., Springer, 2016, ch. 1a, pp. 151–187.

[64] D. F. Williams, "On the mechanisms of biocompatibility," *Biomaterials*, vol. 29, no. 20, pp. 2941–2953, 2008, doi: 10.1016/j.biomaterials.2008.04.023.

[65] S. Lavenus, P. Pilet, J. Guicheux, P. Weiss, G. Louarn, and P. Layrolle, "Behaviour of mesenchymal stem cells, fibroblasts and osteoblasts on smooth surfaces," *Acta Biomater.*, vol. 7, no. 4, pp. 1525–1534, 2011, doi: 10.1016/j.actbio.2010.12.033.

[66] J. Hasan, R. J. Crawford, and E. P. Ivanova, "Antibacterial surfaces: The quest for a new generation of biomaterials," *Trends Biotechnol.*, vol. 31, no. 5, pp. 295–304, 2013, doi: 10.1016/j.tibtech.2013.01.017.

[67] I. Milošev, "Surface Treatments of Titanium with Antibacterial Agents for Implant Applications," in Biomedical and Pharmaceutical Applications of Electrochemistry, S. Djokic, Ed. Springer, 2016, pp. 1–72.

[68] B. Gottenbos, D. W. Grijpma, H. C. Van Der Mei, J. Feijen, and H. J. Busscher, "Antimicrobial effects of positively charged surfaces on adhering Gram-positive and Gram-negative bacteria," *J. Antimicrob. Chemother.*, vol. 48, no. 1, pp. 7–13, 2001, doi: 10.1093/jac/48.1.7.

[69] B. A. Jucker, H. Harms, and A. J. B. Zehnder, "Adhesion of the positively charged bacterium Stenotrophomonas (Xanthomonas) maltophilia 70401 to glass and teflon,"

J. Bacteriol., vol. 178, no. 18, pp. 5472–5479, 1996, doi: 10.1128/jb.178.18.5472-5479.1996.

[70] K. Anselme, P. Davidson, A. M. Popa, M. Giazzon, M. Liley, and L. Ploux, "The interaction of cells and bacteria with surfaces structured at the nanometre scale," *Acta Biomater.*, vol. 6, no. 10, pp. 3824–3846, 2010, doi: 10.1016/j.actbio.2010.04.001.

[71] Y. Wu, J. P. Zitelli, K. S. TenHuisen, X. Yu, and M. R. Libera, "Differential response of Staphylococci and osteoblasts to varying titanium surface roughness," *Biomaterials*, vol. 32, no. 4, pp. 951–960, 2011, doi: 10.1016/j.biomaterials.2010.10.001.

[72] B. D. Hatton, "Antimicrobial coatings for metallic biomaterials," in Surface Coating and Modification of Metallic Biomaterials, Woodhead Pblishing, 2015, pp. 379–391.

[73] T. R. Rautray, R. Narayanan, and K. H. Kim, "Ion implantation of titanium based biomaterials," *Prog. Mater. Sci.*, vol. 56, no. 8, p. 1137, 2011, doi: 10.1016/j.pmatsci.2011.03.002.

[74] P. Budzynski, "Long-range effect in nitrogen ion-implanted AISI 316L stainless steel," *Nucl. Instruments Methods Phys. Res. Sect. B Beam Interact. with Mater. Atoms*, vol. 342, pp. 1–6, 2015, doi: 10.1016/j.nimb.2014.09.004.

[75] J. Z. Shi, C. Z. Chen, H. J. Yu, and S. J. Zhang, "Application of magnetron sputtering for producing bioactive ceramic coatings on implant materials," *Bull. Mater. Sci.*, vol. 31, no. 6, pp. 877–884, 2008, doi: 10.1007/s12034-008-0140-z.

[76] A. M. Ektessabi, "Surface modification of biomedical implants using ion-beam-assisted sputter deposition," *Nucl. Instruments Methods Phys. Res. Sect. B Beam Interact. with Mater. Atoms*, vol. 127–128, pp. 1008–1014, 1997, doi: 10.1016/S0168-583X(97)00049-9.

[77] G. Giavaresi *et al.*, "Histomorphometric, ultrastructural and microhardness evaluation of the osseointegration of a nanostructured titanium oxide coating by metal-organic chemical vapour deposition: An in vivo study," *Biomaterials*, vol. 25, no. 25, pp. 5583–5591, 2004, doi: 10.1016/j.biomaterials.2004.01.017.

[78] L. Duta and A. C. Popescu, "Current status on pulsed laser deposition of coatings from animal-origin calcium phosphate sources," *Coatings*, vol. 9, no. 5, pp. 1–42, 2019, doi: 10.3390/coatings9050335.

[79] A. Jaafar, C. Hecker, P. Árki, and Y. Joseph, "Sol-gel derived hydroxyapatite coatings for titanium implants: A review," *Bioengineering*, vol. 7, no. 4, pp. 1–23, 2020, doi: 10.3390/bioengineering7040127.

[80] Y. Parcharoen, P. Kajitvichyanukul, S. Sirivisoot, and P. Termsuksawad, "Hydroxyapatite electrodeposition on anodized titanium nanotubes for orthopedic applications," *Appl. Surf. Sci.*, vol. 311, pp. 54–61, 2014, doi: 10.1016/j.apsusc.2014.04.207.

[81] B. Moore, E. Asadi, and G. Lewis, "Deposition methods for Microstructured and Nanostructured coatings on metallic bone implants: A review," *Adv. Mater. Sci. Eng.*, vol. 2017, pp. 1–9 2017, doi: 10.1155/2017/5812907.

[82] C. Toccafondi, S. Dante, A. P. Reverberi, and M. Salerno, "Biomedical Applications of Anodic Porous Alumina," *Curr. Nanosci.*, vol. 11, no. 5, pp. 572–580, 2015, doi: 10.2174/1573413711666150415225541.

[83] B. J. McEntire, B. S. Bal, M. N. Rahaman, J. Chevalier, and G. Pezzotti, "Ceramics and ceramic coatings in orthopaedics," *J. Eur. Ceram. Soc.*, vol. 35, no. 16, pp. 4327–4369, 2015, doi: 10.1016/j.jeurceramsoc.2015.07.034.

[84] A. Sáenz, E. Rivera, W. Brostow, and V. Castaño, "Ceramic biomaterials: an introductory overview," *J. Mater. Educ.*, vol. 21, no. 5/6, pp. 267–276, 1999.

[85] P. Li, C. Ohtsuki, T. Kokubo, K. Nakanishi, N. Soga, and K. de Groot, "The role of hydrated silica, titania, and alumina in inducing apatite on implants," *J. Biomed. Mater. Res.*, vol. 28, no. 1, pp. 7–15, 1994, doi: 10.1002/jbm.820280103.

[86] M. Leskelä, J. Niinistö, and M. Ritala, "Atomic Layer Deposition," *Compr. Mater. Process.*, vol. 4, pp. 101–123, 2014, doi: 10.1016/B978-0-08-096532-1.00401-5.

[87] M. Leskelä, J. Niinistö, and M. Ritala, "Atomic Layer Deposition," in *Comprehensive Materials Processing*, 1st ed., vol. 4, S. Hashmi, Ed. Oxford: Elsevier Ltd., 2014, p. 101.

[88] T. Kääriäinen, D. Cameron, M.-L. Kääriäinen, and A. Sherman, *Atomic layer deposition - Principles, Characteristics, and Nanotechnology Applications*, 2nd ed., Scrivener Publishing LLC., 2013, p. 272.

[89] V. Cremers, R. L. Puurunen, and J. Dendooven, "Conformality in atomic layer deposition: Current status overview of analysis and modelling," *Appl. Phys. Rev.*, vol. 6, no. 2, p. 021302, 2019, doi: 10.1063/1.5060967.

[90] M. Ritala, M. Leskelä, J. P. Dekker, C. Mutsaers, P. J. Soininen, and J. Skarp, "Perfectly conformal TiN and Al_2O_3 films deposited by atomic layer deposition," *Chem. Vap. Depos.*, vol. 5, no. 1, pp. 7–9, 1999, doi: 10.1002/(SICI)1521-3862(199901)5:1<7::AID-CVDE7>3.0.CO;2-J.

[91] S. A. Skoog, J. W. Elam, and R. J. Narayan, "Atomic layer deposition: Medical and biological applications," *Int. Mater. Rev.*, vol. 58, no. 2, p. 113, 2013, doi: 10.1179/1743280412Y.0000000009.

[92] R. Matero, M. Ritala, M. Leskelä, T. Salo, J. Aromaa, and O. Forsén, "Atomic layer deposited thin films for corrosion protection," *J. Phys. IV*, vol. 9, no. 8, p. 493, 1999, doi: 10.1051/jp4:1999862.

[93] H. C. M. Knoops, S. E. Potts, A. A. Bol, and W. M. M. Kessels, "Atomic Layer Deposition," in Handbook of Crystal Growth, *2nd Ed.*, Elsevier, 2015, ch. 27, pp. 1101–1134, doi: 10.1016/B978-0-444-63304-0.00027-5.

[94] R. L. Puurunen, "Surface chemistry of atomic layer deposition: A case study for the trimethylaluminum/water process," *J. Appl. Phys.*, vol. 97, no. 12, 2005, p. 121301 doi: 10.1063/1.1940727.

[95] J. A. Carlisle, M. J. Pellin, J. W. Elam, and J. Wang, "Hermetic Bio-Inert Coatings for bio-Implants Fabricated Using Atomic Layer Deposition," US2006/0251875A1, 2006.

[96] A. K. Bishal *et al.*, "Atomic Layer Deposition in Bio-Nanotechnology: A Brief Overview," *Crit. Rev. Biomed. Eng.*, vol. 43, no. 4, pp. 255–276, 2015, doi: 10.1615/CritRevBiomedEng.2016016456.

[97] E. Marin, L. Guzman, A. Lanzutti, W. Ensinger, and L. Fedrizzi, "Multilayer Al_2O_3/TiO_2 atomic layer deposition coatings for the corrosion protection of stainless steel," *Thin Solid Films*, vol. 522, p. 283, 2012, doi: 10.1016/j.tsf.2012.08.023.

[98] A. I. Abdulagatov *et al.*, "Al_2O_3 and TiO_2 Atomic Layer Deposition on Copper for Water Corrosion Resistance," *ACS Appl. Mater. Interfaces*, vol. 3, no. 12, p. 4593, 2011, doi: 10.1021/am2009579.

[99] J. S. Daubert *et al.*, "Corrosion protection of copper using Al_2O_3, TiO_2, ZnO, HfO_2, and ZrO_2 Atomic layer deposition," *ACS Appl. Mater. Interfaces*, vol. 9, no. 4, p. 4192, 2017, doi: 10.1021/acsami.6b13571.

[100] S. E. Potts *et al.*, "Ultra-Thin Aluminium Oxide Films Deposited by Plasma-Enhanced Atomic Layer Deposition for Corrosion Protection," *J. Electrochem. Soc.*, vol. 158, no. 5, p. C132, 2011, doi: 10.1149/1.3560197.

[101] A. K. Singh, K. Adstedt, B. Brown, P. M. Singh, and S. Graham, "Development of ALD Coatings for Harsh Environment Applications," *ACS Appl. Mater. Interfaces*, vol. 11, no. 7, pp. 7498–7509, 2019, doi: 10.1021/acsami.8b11557.

[102] G. C. Correa, B. Bao, and N. C. Strandwitz, "Chemical stability of titania and alumina thin films formed by atomic layer deposition," *ACS Appl. Mater. Interfaces*, vol. 7, no. 27, pp. 14816–14821, 2015, doi: 10.1021/acsami.5b03278.

[103] M. K. Abbass, S. A. Ajeel, and H. M. Wadullah, "Biocompatibility, Bioactivity and Corrosion Resistance of Stainless Steel 316L Nanocoated with TiO_2 and Al_2O_3 by Atomic Layer Deposition Method," *J. Phys. Conf. Ser.*, vol. 1032, no. 1, p. 012017, 2018, doi: 10.1088/1742-6596/1032/1/012017.

[104] D. S. Finch, T. Oreskovic, K. Ramadurai, C. F. Herrmann, S. M. George, and R. L. Mahajan, "Biocompatibility of atomic layer-deposited alumina thin films," *J. Biomed. Mater. Res. - Part A*, vol. 87, no. 1, p. 100, 2008, doi: 10.1002/jbm.a.31732.

[105] F. Wang, Y. Zhang, X. Chen, B. Leng, X. Guo, and T. Zhang, "ALD mediated heparin grafting on nitinol for self-expanded carotid stents," *Colloids Surfaces B Biointerfaces*, vol. 143, pp. 390–398, 2016, doi: 10.1016/j.colsurfb.2016.03.063.

[106] D. Vokoun *et al.*, "Al_2O_3 and Pt atomic layer deposition for surface modification of NiTi shape memory films," *Coatings*, vol. 10, no. 8, pp. 1–14, 2020, doi: 10.3390/COATINGS10080746.

[107] Q. Yang *et al.*, "Atomic layer deposited ZrO_2 nanofilm on Mg-Sr alloy for enhanced corrosion resistance and biocompatibility," *Acta Biomater.*, vol. 58, p. 515, 2017, doi: 10.1016/j.actbio.2017.06.015.

[108] M. Peron, A. Bin Afif, A. L. Dadlani, F. Berto, and J. Torgersen, "Improving stress corrosion cracking behavior of AZ31 alloy with conformal thin titania and zirconia coatings for biomedical applications," *J. Mech. Behav. Biomed. Mater.*, vol. 111, p. 104005, 2020, doi: 10.1016/j.jmbbm.2020.104005.

[109] A. Ziębowicz *et al.*, "Evaluation of bacterial adhesion to the ZrO_2 atomic layer deposited on the surface of cobalt-chromium dental alloy produced by DMLS method," *Materials (Basel).*, vol. 14, no. 5, pp. 1–15, 2021, doi: 10.3390/ma14051079.

[110] I. P. Grigal, A. M. Markeev, S. A. Gudkova, A. G. Chernikova, A. S. Mityaev, and A. P. Alekhin, "Correlation between bioactivity and structural properties of titanium dioxide coatings grown by atomic layer deposition," *Appl. Surf. Sci.*, vol. 258, no. 8, p. 3415, 2012, doi: 10.1016/j.apsusc.2011.11.082.

[111] M. Shahmohammadi, B. Yang, and C. G. Takoudis, "Applications of Titania Atomic Layer Deposition in the Biomedical Field and Recent Updates," *Am. J. Biomed. Sci. Res.*, vol. 8, no. 6, pp. 465–468, 2020, doi: 10.34297/ajbsr.2020.08.001321.

[112] M. Putkonen *et al.*, "Atomic layer deposition and characterization of biocompatible hydroxyapatite thin films," *Thin Solid Films*, vol. 517, no. 20, p. 5819, 2009, doi: 10.1016/j.tsf.2009.03.013.

[113] I. Levin and D. Brandon, "Metastable alumina polymorphs: Crystal structures and transition sequences," *J. Am. Ceram. Soc.*, vol. 81, no. 8, pp. 1995–2012, 1998, doi: 10.1111/j.1151-2916.1998.tb02581.x.

[114] H. H. Al-Moameri, Z. Majid Nahi, D. Raheem Rzaij, and N. T. Al-Sharify, "a Review on the Biomedical Applications of Alumina," *J. Eng. Sustain. Dev.*, vol. 24, no. 05, pp. 28–36, 2020, doi: 10.31272/jeasd.24.5.5.

[115] E. Denes, G. Barrière, E. Poli, and G. Lévêque, "Alumina biocompatibility," *J. Long. Term. Eff. Med. Implants*, vol. 28, no. 1, pp. 9–13, 2018, doi: 10.1615/JLongTermEffMedImplants.2018025635.

[116] M. Rahmati and M. Mozafari, "Biocompatibility of alumina-based biomaterials–A review," *J. Cell. Physiol.*, vol. 234, no. 4, p. 3321, 2019, doi: 10.1002/jcp.27292.

[117] A. Engelhardt, M. Salzer, A. Zeibig, and H. Locke, "Experiences with Al_2O_3 implantations in humans to bridge resection defects," *J. Biomed. Mater. Res.*, vol. 9, no. 4, pp. 227–232, 1975, doi: 10.1002/jbm.820090425.

[118] V. Miikkulainen, M. Leskelä, M. Ritala, and R. L. Puurunen, "Crystallinity of inorganic films grown by atomic layer deposition: Overview and general trends," *J. Appl. Phys.*, vol. 113, no. 2, 2013, doi: 10.1063/1.4757907.

[119] E. Ghiraldelli, C. Pelosi, E. Gombia, G. Chiavarotti, and L. Vanzetti, "ALD growth, thermal treatments and characterisation of Al2O3 layers," *Thin Solid Films*, vol. 517, no. 1, pp. 434–436, 2008, doi: 10.1016/j.tsf.2008.08.052.

[120] J. Robertson, "High dielectric constant oxides J.," *Eur. Phys. J. Appl. Phys.*, vol. 28, no. 3, p. 265, 2004, doi: DOI: 10.1051/epjap:2004206.

[121] M. J. Biercuk, D. J. Monsma, C. M. Marcus, J. S. Backer, and R. G. Gordon, "Low-temperature atomic-layer-deposition lift-off method for microelectronic and nanoelectronic applications," *Appl. Phys. Lett.*, vol. 83, no. 12, p. 2405, 2003, doi: 10.1063/1.1612904.

[122] K. Kukli *et al.*, "Effect of selected atomic layer deposition parameters on the structure and dielectric properties of hafnium oxide films," *J. Appl. Phys.*, vol. 96, no. 9, pp. 5298–5307, 2004, doi: 10.1063/1.1796513.

[123] F. Zhang, G. Liu, A. Liu, B. Shin, and F. Shan, "Solution-processed hafnium oxide dielectric thin films for thin-film transistors applications," *Ceram. Int.*, vol. 41, no. 10, pp. 13218–13223, 2015, doi: 10.1016/j.ceramint.2015.07.099.

[124] D. A. Golosov, S. M. Zavadski, S. N. Melnikov, and N. Villa, "Dielectric Characteristics of Hafnia Thin Films," *Nanotechnologies Russ.*, vol. 12, no. 9–10, pp. 529–533, 2017, doi: 10.1134/S1995078017050020.

[125] L. Wachnicki, S. Gieraltowska, B. S. Witkowski, M. Godlewski, M. M. Godlewski, and A. Slonska-Zielonka, "Antimicrobial coatings grown by the atomic layer deposition technique," in *IEEE International Conference on Nanotechnology*, 2015, p. 846, doi: 10.1109/NANO.2015.7388745.

[126] Z. Fohlerova and A. Mozalev, "Anodic formation and biomedical properties of hafnium-oxide nanofilms," *J. Mater. Chem. B*, vol. 7, no. 14, p. 2300, 2019, doi: 10.1039/c8tb03180k.

[127] S. Mohammadi, M. Esposito, M. Cucu, L. E. Ericson, and P. Thomsen, "Tissue response to hafnium," *J. Mater. Sci. Mater. Med.*, vol. 12, no. 7, pp. 603–611, 2001, doi: 10.1023/A:1011237610299.

[128] H. Matsuno, A. Yokoyama, F. Watari, M. Uo, and T. Kawasaki, "Biocompatibility and osteogenesis of refractory metal implants, titanium, hafnium, niobium, tantalum and rhenium," *Biomaterials*, vol. 22, no. 11, pp. 1253–1262, 2001, doi: 10.1016/S0142-9612(00)00275-1.

[129] D. M. Hausmann and R. G. Gordon, "Surface morphology and crystallinity control in the atomic layer deposition (ALD) of hafnium and zirconium oxide thin films," *J. Cryst. Growth*, vol. 249, no. 1–2, pp. 251–261, 2003, doi: 10.1016/S0022-0248(02)02133-4.

[130] D. Blaschke *et al.*, "A correlation study of layer growth rate, thickness uniformity, stoichiometry, and hydrogen impurity level in HfO_2 thin films grown by ALD between 100°C and 350°C," *Appl. Surf. Sci.*, vol. 506, p. 144188, 2020, doi: 10.1016/j.apsusc.2019.144188.

[131] I. Spajić, P. Rodič, G. Šekularac, M. Lekka, L. Fedrizzi, and I. Milošev, "The effect of surface preparation on the protective properties of Al_2O_3 and HfO_2 thin films deposited on cp-titanium by atomic layer deposition," *Electrochim. Acta*, vol. 366, p. 137431, 2021, doi: 10.1016/j.electacta.2020.137431.

[132] I. Spajić, E. Rahimi, M. Lekka, R. Offoiach, L. Fedrizzi, and I. Milošev, " Al_2O_3 and HfO_2 Atomic Layers Deposited in Single and Multilayer Configurations on Titanium and on Stainless Steel for Biomedical Applications ," *J. Electrochem. Soc.*, vol. 168, no. 7, p. 071510, 2021, doi: 10.1149/1945-7111/ac131b.

[133] E. S. Gadelmawla, M. M. Koura, T. M. A. Maksoud, I. M. Elewa, and H. H. Soliman, "Roughness parameters," *J. Mater. Process. Technol.*, vol. 123, no. 1, pp. 133–145, 2002, doi: 10.1016/S0924-0136(02)00060-2.

[134] I. Horcas, R. Fernández, J. M. Gómez-Rodríguez, J. Colchero, J. Gómez-Herrero, and A. M. Baro, "WSXM: A software for scanning probe microscopy and a tool for nanotechnology," *Rev. Sci. Instrum.*, vol. 78, no. 1, p. 013705, 2007, doi: 10.1063/1.2432410.

[135] C. Monteiro, F. Costa, A. M. Pirttilä, M. V. Tejesvi, and M. C. L. Martins, "Prevention of urinary catheter-associated infections by coating antimicrobial peptides from crowberry endophytes," *Sci. Rep.*, vol. 9, no. 1, pp. 1–14, 2019, doi: 10.1038/s41598-019-47108-5.

[136] R. M. Pinto *et al.*, "N-Acetyl-l-cysteine-Loaded Nanosystems as a Promising Therapeutic Approach Toward the Eradication of Pseudomonas aeruginosa Biofilms," *ACS Appl. Mater. Interfaces*, vol. 13, no. 36, pp. 42329-42343, 2021, doi: 10.1021/acsami.1c05124.

[137] M. Ritala, H. Saloniemi, M. Leskelä, T. Prohaska, G. Friedbacher, and M. Grasserbauer, "Studies on the morphology of Al_2O_3 thin films grown by atomic layer epitaxy," *Thin Solid Films*, vol. 286, no. 1–2, pp. 54–58, 1996, doi: 10.1016/S0040-6090(95)08524-6.

[138] J. W. Elam, Z. A. Sechrist, and S. M. George, "ZnO/Al_2O_3 nanolaminates fabricated by atomic layer deposition: Growth and surface roughness measurements," *Thin Solid Films*, vol. 414, no. 1, pp. 43–55, 2002, doi: 10.1016/S0040-6090(02)00427-3.

[139] W. S. Lau, J. Zhang, X. Wan, J. K. Luo, Y. Xu, and H. Wong, "Surface smoothing effect of an amorphous thin film deposited by atomic layer deposition on a surface with nano-sized roughness," *AIP Adv.*, vol. 4, no. 2, pp. 1–5, 2014, doi: 10.1063/1.4866988.

[140] D. V. Nazarov, E. G. Zemtsova, A. Yu. Solokhin, R. Z. Valiev, and V. M. Smirnov, "Modification of the surface topography and composition of ultrafine and coarse grained titanium by chemical etching," *Nanomaterials*, vol. 7, no. 1, pp. 1–15, 2017, doi: 10.3390/nano7010015.

[141] S. Okawa and K. Watanabe, "Chemical mechanical polishing of titanium with colloidal silica containing hydrogen peroxide - Mirror polishing and surface properties," *Dent. Mater. J.*, vol. 28, no. 1, pp. 68–74, 2009, doi: 10.4012/dmj.28.68.

[142] C. Ohtsuki, H. Iida, S. Hayakawa, and A. Osaka, "Bioactivity of titanium treated with hydrogen peroxide solutions containing metal chlorides," *J. Biomed. Mater. Res.*, vol. 35, no. 1, pp. 39–47, 1997, doi: 10.1002/(SICI)1097-4636(199704)35:1<39::AID-JBM5>3.0.CO;2-N.

[143] B. Wälivaara, B. O. Aronsson, M. Rodahl, J. Lausmaa, and P. Tengvall, "Titanium with different oxides: in vitro studies of protein adsorption and contact activation," *Biomaterials*, vol. 15, no. 10, pp. 827–834, 1994, doi: 10.1016/0142-9612(94)90038-8.

[144] N. P. Kobayashi, C. L. Donley, S. Y. Wang, and R. S. Williams, "Atomic layer deposition of aluminum oxide on hydrophobic and hydrophilic surfaces," *J. Cryst. Growth*, vol. 299, no. 1, pp. 218–222, 2007, doi: 10.1016/j.jcrysgro.2006.11.224.

[145] X. Liu, P. K. Chu, and C. Ding, "Surface modification of titanium, titanium alloys, and related materials for biomedical applications," *Mater. Sci. Eng. R Reports*, vol. 47, no. 3–4, pp. 49–121, 2004, doi: 10.1016/j.mser.2004.11.001.

[146] P. Tengvall, I. Lundström, L. Sjöqvist, H. Elwing, and L. M. Bjursten, "Titanium-hydrogen peroxide interaction: model studies of the influence of the inflammatory response on titanium implants," *Biomaterials*, vol. 10, no. 3, pp. 166–175, 1989, doi: 10.1016/0142-9612(89)90019-7.

[147] O. Miyakawa, K. Watanabe, S. Okawa, M. Kanatani, S. Nakano, and M. Kobayashi, "Surface Contamination of Titanium by Abrading Treatment," *Dent. Mater. J.*, vol. 15, no. 1, pp. 11–21, 1996, doi: 10.4012/dmj.15.11.

[148] J. C. Vickerman, " Molecular Surface Mass Spectrometry by SIMS," in Surface Analysis - The Principal Techniques, 2nd ed., J. C. Vickerman and I. S. Gilmore, Wiley, 2009, ch. 4, pp. 113–203.

[149] C. K. Dyer, "Breakdown and Efficiency of Anodic Oxide Growth on Titanium," *J. Electrochem. Soc.*, vol. 125, no. 7, pp. 1032–1038, 1978, doi: 10.1149/1.2131616.

[150] P. J. Boddy, "Oxygen evolution on semiconducting TiO_2," *J. Electrochem. Soc.*, vol. 115, no. 2, pp. 199–203, 1968, doi: 10.1016/0013-4686(77)85049-4.

[151] I. Milošev, G. Žerjav, J. M. Calderon Moreno, and M. Popa, "Electrochemical properties, chemical composition and thickness of passive film formed on novel Ti-20Nb-10Zr-5Ta alloy," *Electrochim. Acta*, vol. 99, p. 176, 2013, doi: 10.1016/j.electacta.2013.03.086.

[152] J. Yahalom and J. Zahavi, "Electrolytic breakdown crystallization of anodic oxide films on A1, Ta and Ti," *Electrochim. Acta*, vol. 15, no. 9, pp. 1429–1435, 1970, doi: 10.1016/0013-4686(70)80064-0.

[153] C. Aparicio, F. Javier Gil, C. Fonseca, M. Barbosa, and J. A. Planell, "Corrosion behaviour of commercially pure titanium shot blasted with different materials and sizes of shot particles for dental implant applications," *Biomaterials*, vol. 24, no. 2, pp. 263–273, 2003, doi: 10.1016/S0142-9612(02)00314-9.

[154] S. H. Ahn, J. H. Lee, H. G. Kim, and J. G. Kim, "A study on the quantitative determination of through-coating porosity in PVD-grown coatings," *Appl. Surf. Sci.*, vol. 233, p. 105, 2004, doi: 10.1016/j.apsusc.2004.03.213.

[155] W. Tato and D. Landolt, "Electrochemical Determination of the Porosity of Single and Duplex PVD Coatings of Titanium and Titanium Nitride on Brass," *J. Electrochem. Soc.*, vol. 145, no. 12, pp. 4173–4181, 1998, doi: 10.1149/1.1838932.

[156] C. Liu, Q. Bi, A. Leyland, and A. Matthews, "An electrochemical impedance spectroscopy study of the corrosion behavior of PVD coated steels in 0.5 N NaCl aqueous solution: Part II. EIS interpretation of corrossion behaviour," *Corros. Sci.*, vol. 45, no. 6, pp. 1257–1273, 2003, doi: 10.1016/S0010-938X(02)00214-7.

[157] Z. Chai, J. Li, X. Lu, and D. He, "Use of electrochemical measurements to investigate the porosity of ultra-thin Al_2O_3 films prepared by atomic layer deposition," *RSC Adv.*, vol. 4, no. 74, pp. 39365–39371, 2014, doi: 10.1039/C4RA04565C.

[158] B. Díaz *et al.*, "Corrosion properties of steel protected by nanometre-thick oxide coatings," *Corros. Sci.*, vol. 82, pp. 208–217, 2014, doi: 10.1016/j.corsci.2014.01.024.

[159] J. Pan, D. Thierry, and C. Leygraf, "Electrochemical impedance spectroscopy study of the passive oxide film on titanium for implant application," *Electrochim. Acta*, vol. 41, no. 7–8, p. 1143, 1996, doi: 10.1016/0013-4686(95)00465-3.

[160] I. Milošev, M. Metikoš-Huković, and H. H. Strehblow, "Passive film on orthopaedic TiAlV alloy formed in physiological solution investigated by X-ray photoelectron spectroscopy," *Biomaterials*, vol. 21, no. 20, pp. 2103–2113, 2000, doi: 10.1016/S0142-9612(00)00145-9.

[161] Y. Tanaka, E. Kobayashi, S. Hiromoto, K. Asami, H. Imai, and T. Hanawa, "Calcium phosphate formation on titanium by low-voltage electrolytic treatments," *J. Mater. Sci. Mater. Med.*, vol. 18, no. 5, p. 797, 2007.

[162] I. Milošev, J. Hmeljak, G. Žerjav, A. Cör, J. M. Calderon Moreno, and M. Popa, "Quaternary Ti-20Nb-10Zr-5Ta alloy during immersion in simulated physiological solutions: Formation of layers, dissolution and biocompatibility," *J. Mater. Sci. Mater. Med.*, vol. 25, no. 4, pp. 1099–1114, 2014, doi: 10.1007/s10856-014-5144-1.

[163] I. Milošev and H. H. Strehblow, "The behavior of stainless steels in physiological solution containing complexing agent studied by x-ray photoelectron spectroscopy," *J. Biomed. Mater. Res.*, vol. 52, no. 2, p. 404, 2000, doi: 10.1002/1097-4636(200011)52:2<404::AID-JBM22>3.0.CO;2-Z.

[164] S. Tamilselvi, R. Murugaraj, and N. Rajendran, "Electrochemical impedance spectroscopic studies of titanium and its alloys in saline medium," *Mater. Corros.*, vol. 58, no. 2, p. 113, 2007, doi: 10.1002/maco.200603979.

[165] J. J. M. Damen, J. M. Ten Cate, and J. E. Ellingsen, "Induction of Calcium Phosphate Precipitation by Titanium Dioxide," *J. Dent. Res.*, vol. 70, no. 10, p. 1346, 1991, doi: 10.1177/00220345910700100601.

[166] H. B. Wen, J. G. C. Wolke, J. R. De Wijn, W. Q. Liu, F. Z. Cui, and K. De Groot, "Fast precipitation of calcium phosphate layers on titanium induced by simple chemical treatments," *Biomaterials*, vol. 18, no. 22, p. 1471, 1997, doi: 10.1016/S0142-9612(97)82297-1.

[167] J. E. Sundgren, P. Bodö, and I. Lundström, "Auger electron spectroscopic studies of the interface between human tissue and implants of titanium and stainless steel," *J. Colloid Interface Sci.*, vol. 110, no. 1, p. 9, 1986, doi: 10.1016/0021-9797(86)90348-6.

[168] I. Iatsunskyi, M. Kempiński, M. Jancelewicz, K. Załęski, S. Jurga, and V. Smyntyna, "Structural and XPS characterization of ALD Al_2O_3 coated porous silicon," *Vacuum*, vol. 113, p. 52, 2015, doi: 10.1016/j.vacuum.2014.12.015.

[169] M. Rohwerder and F. Turcu, "High-resolution Kelvin probe microscopy in corrosion science: Scanning Kelvin probe force microscopy (SKPFM) versus classical scanning Kelvin probe (SKP)," *Electrochim. Acta*, vol. 53, no. 2, p. 290, 2007, doi: 10.1016/j.electacta.2007.03.016.

[170] C. Örnek, C. Leygraf, and J. Pan, "On the Volta potential measured by SKPFM–fundamental and practical aspects with relevance to corrosion science," *Corros. Eng. Sci. Technol.*, vol. 54, no. 3, p. 185, 2019, doi: 10.1080/1478422X.2019.1583436.

[171] E. Rahimi, A. Rafsanjani-Abbasi, A. Imani, and A. Davoodi, "TiO_2/Cu_2O coupled oxide films in Cl− ion containing solution: Volta potential and electronic properties characterization by scanning probe microscopy," *Mater. Chem. Phys.*, vol. 212, p. 403, 2018, doi: 10.1016/j.matchemphys.2018.03.066.

[172] H. Zhu and R. Ramprasad, "Effective work function of metals interfaced with dielectrics: A first-principles study of the Pt-HfO_2 interface," *Phys. Rev. B - Condens. Matter Mater. Phys.*, vol. 83, no. 8, p. 081416, 2011, doi: 10.1103/PhysRevB.83.081416.

[173] M. T. Greiner and Z. H. Lu, “Thin-film metal oxides in organic semiconductor devices: Their electronic structures, work functions and interfaces,” *NPG Asia Mater.*, vol. 5, no. 7, p. e55, 2013, doi: 10.1038/am.2013.29.

[174] R. Hausbrand, M. Stratmann, and M. Rohwerder, “The Physical Meaning of Electrode Potentials at Metal Surfaces and Polymer/Metal Interfaces: Consequences for Delamination,” *J. Electrochem. Soc.*, vol. 155, no. 7, p. C369, 2008, doi: 10.1149/1.2926589.

[175] R. L. Puurunen *et al.*, “Controlling the crystallinity and roughness of atomic layer deposited titanium dioxide films,” *J. Nanosci. Nanotechnol.*, vol. 11, no. 9, pp. 8101–8107, 2011, doi: 10.1166/jnn.2011.5060.

[176] J. Aarik, A. Aidla, T. Uustare, and V. Sammelselg, “Morphology and structure of TiO_2 thin films grown by atomic layer deposition,” *J. Cryst. Growth*, vol. 148, no. 3, pp. 268–275, 1995, doi: 10.1016/0022-0248(94)00874-4.

[177] R. A. Gittens *et al.*, “The effects of combined micron-/submicron-scale surface roughness and nanoscale features on cell proliferation and differentiation,” *Biomaterials*, vol. 32, no. 13, pp. 3395–3403, 2011, doi: 10.1016/j.biomaterials.2011.01.029.

[178] P. Kondaiah, H. Shaik, and G. Mohan Rao, “Studies on RF magnetron sputtered HfO_2 thin films for microelectronic applications,” *Electron. Mater. Lett.*, vol. 11, no. 4, pp. 592–600, 2015, doi: 10.1007/s13391-015-4490-6.

[179] E. E. Stansbury and R. A. Buchanan, "Electrochemical Corrosion-Rate Measurements," in Fundamentals of Electrochemical Corrosion, 1st ed., ASM International, 2000, ch. 6, pp. 233–268.

Bibliography

Publications Related to the Thesis

Journal Articles

I. Spajić, P. Rodič, G. Šekularac, M. Lekka, L. Fedrizzi, I. Milošev, The effect of surface preparation on the protective properties of Al_2O_3 and HfO_2 thin films deposited on cp-titanium by atomic layer deposition, Electrochim. Acta, 366, 137431 (2021), doi: 10.1016/j.electacta.2020.13743.

I. Spajić, E. Rahimi, M. Lekka, R. Offoiach, L. Fedrizzi, Ingrid Milošev, Al_2O_3 and HfO_2 Atomic Layers Deposited in Single and Multilayer Configurations on Titanium and on Stainless Steel for Biomedical Applications, J. Electrochem. Soc., 168, 071510 (2021), doi: 10.1149/1945-7111/ac131b.

Other Publications

Journal Articles

D. Sačer, I. Spajić, M. Kraljić Roković, Z. Mandić, New insights into chemical and electrochemical functionalization of graphene oxide electrodes by o-phenylenediamine and their potential applications, J. Mater. Sci., 53, 15285 (2018), doi: 10.1007/s10853-018-2693.

Biography

Ivan Spajić was born on February 6th, 1993 in Žepče, Bosnia and Herzegovina. He studied Chemistry and Engineering of Materials at the Faculty of Chemical Engineering and Technology (University of Zagreb) from 2011 to 2017. In July 2017, he defended his master's thesis entitled "Modification of graphene oxide with aromatic amines" at the Department of Electrochemistry and received the degree of Master in Material Science and Engineering (M.Sc.Eng). Since April 2018, he has been employed at the Jožef Stefan Institute in Ljubljana as a MSCA-ITN ESR fellow within the framework of the mCBEEs project. In September 2018, he enrolled in the Jožef Stefan International Postgraduate School, Nanosciences and Nanotechnologies programme, under the supervision of Prof. Dr. Ingrid Milošev. He is the co-author of three scientific articles, two of which are related to his PhD thesis. In both of these articles, he is the first co-author.

Addendum

Alumina (Al_2O_3), as an amorphous passive film spontaneously formed on metallic aluminum is thermodynamically stable in the pH range from 3.9 to 8.6 and in a wide range of potentials in aqueous solutions, as presented in E vs. pH Pourbaix diagram for aluminum [1]. Therefore, aluminum is protected against corrosion in these conditions. However, during long-term immersion in the simulated physiological solution, we observed instability and dissolution of alumina when deposited as thin film of 20 nm (see sections 3.2.3.1 and 3.3.3.1). To further explain this unexpected result, we herein relate it to similar observations in the literature.

Abdulagatov et al. investigated the possibility of using ultra-thin ALD alumina and titania films to protect copper against corrosion in water at the temperature of 90 °C [2]. They reported on the solubility of ALD alumina of 200 Å under the tested conditions resulting in insufficient protection of copper. Correa et al. investigated the chemical stability of alumina and titania in water and different aqueous solutions at room temperature, as-deposited and after thermal treatment at different temperatures [3]. They also reported on the instability of alumina when deposited as a 50 nm thick film in pure water, as-deposited and after annealing at 450 °C, while at higher annealing temperatures, alumina was stable. Since they were focused on the change in roughness due to the degradation of ALD alumina thin films, they used AFM measurements. They proposed that ALD alumina thin films in pure water undergoes hydration with a dynamic dissolution/precipitation process, which causes an increase in surface roughness. In addition, they state that hydration of amorphous alumina can result in crystallization into bayerite and gibbsite, polymorphs of aluminum hydroxide, increasing the volume of deposit, as investigated here [4].

Therefore, when we consider the properties and stability of alumina obtained by the ALD method, we cannot equalize it with spontaneously formed passive aluminum-(hydr)oxide on metallic aluminum [5], nor with crystalline alumina, which is a very chemically stable material [6]. Further, as reported, ALD alumina thin films may contain relatively high residual C and H atoms from the precursor, primarily if TMA is used [7]. This fact certainly affects the chemical stability of alumina when it is deposited by the ALD method. Moreover, residual atoms, primarily H, are more pronounced the thinner the deposited film. This is a consequence of the incomplete reaction with water and the retention of −OH groups in the alumina structure. However, residual −OH groups, with a longer deposition time when growing thicker films, are available for further oxidation, i.e., a complete reaction between TMA and water, as reported here [8]. Therefore, thinner alumina films tend to retain more residual −OH groups, while thicker films are more like pure alumina due to the longer ALD process. This also explains why the 20 nm alumina thin film showed apparent instability after a few days of immersion in Hanks' solution at 37 °C, while the thicker film of 60 nm remained stable throughout the 30-day immersion period.

References:

[1] E. McCafferty, "Introduction to Corrosion Science," 1st ed., Springer, 2010, pp. 1–518.
[2] A. I. Abdulagatov et al., "Al_2O_3 and TiO_2 Atomic Layer Deposition on Copper for Water Corrosion Resistance," *ACS Appl. Mater. Interfaces*, vol. 3, no. 12, p. 4593, 2011.
[3] G. C. Correa, B. Bao, and N. C. Strandwitz, "Chemical stability of titania and alumina thin films formed by atomic layer deposition," *ACS Appl. Mater. Interfaces*, vol. 7, no. 27, pp. 14816–14821, 2015.
[4] G. Lefevre, M. Duc, P. Lepeut, R. Caplain, M. Fedoroff, Hydration of γ-Alumina in Water and Its Effects on Surface Reactivity, *Langmuir*, vol. 18, no. 20, pp. 7530−7537, 2002.
[5] M. Elboujdaini, E. Ghali, R. G. Barradas and M. Girgis, Potentiostatic study of the passivation of aluminium alloys in aqueous electrolyte media, *J. Appl. Electrochem.*, vol. 25, pp. 412−417, 1995.
[6] I. Levin and D. Brandon, "Metastable alumina polymorphs: Crystal structures and transition sequences," *J. Am. Ceram. Soc.*, vol. 81, no. 8, pp. 1995–2012, 1998.
[7] S.J. Yun, K.-H. Lee, J. Skarp, H.-R. Kim, K.-S. Nam, Dependence of atomic layer-deposited Al_2O_3 films characteristics on growth temperature and Al precursors of $Al(CH_3)_3$ and $AlCl_3$, *J. Vacuum Sci. Technol. A: Vacuum Surf. Films*, vol. 15, pp. 2993-2997, 1997.
[8] S. Mirhashemihaghighi, J. Światowska, V. Maurice, A. Seyeux, L.H. Klein, E. Härkönen, M. Ritala and P. Marcus, *J. Electrochem. Soc.*, vol. 162, no. 8, pp. C377–C384, 2015.